INVESTIGATION OF THE CRUST AND UPPERMOST MANTLE IN THE CAROLINA TERRANE AND BLUE RIDGE, SOUTHERN APPALACHIANS, USING RECEIVER FUNCTION ANALYSIS OF BROADBAND EARTHQUAKE DATA

by

M. SCOTT BAKER

(Under the Direction of Robert B. Hawman)

ABSTRACT

This study provides new estimates of crustal thickness and average crustal composition in the area surrounding two broadband seismic stations located in Murphy, NC in the Blue Ridge mountains and Godfrey, GA in the Carolina Terrane. Lateral variations around each station are investigated by grouping teleseismic wave arrivals into separate azimuthal ranges and finding the corresponding estimates of thickness and average V_P/V_S using receiver function analysis.

The thickness of the crust beneath station MYNC is approximately 48–52 km with a decrease in thickness from the NW to SE, and approximately 39–42 km beneath station GOGA with a similar decrease in thickness from the NW to the SE. V_P/V_S ratios for MYNC vary between 1.742 and 1.852 and suggest the presence of rocks of granitic to intermediate average composition. For GOGA, V_P/V_S was slightly lower (1.720 to 1.777, suggesting a slightly more granitic average crustal composition. The crustal thickness differences between the two stations are consistent with results from previous reflection and refraction profiles which suggest westward crustal thickening beneath the Blue Ridge Mountains and portions of the Valley and Ridge.

INDEX WORDS: Moho, receiver function analysis, crustal, structure, composition, V_P/V_S

INVESTIGATION OF THE CRUST AND UPPERMOST MANTLE IN THE CAROLINA TERRANE AND BLUE RIDGE, SOUTHERN APPALACHIANS, USING RECEIVER FUNCTION ANALYSIS OF BROADBAND EARTHQUAKE DATA

by

M. SCOTT BAKER

B.S., University of Georgia, 2003

A Thesis Submitted to the Graduate Faculty of The University of Georgia in Partial Fulfillment of the Requirements for the Degree

MASTERS OF SCIENCE

ATHENS, GEORGIA

2006

INVESTIGATION OF THE CRUST AND UPPERMOST MANTLE IN THE CAROLINA TERRANE AND BLUE RIDGE, SOUTHERN APPALACHIANS, USING RECEIVER FUNCTION ANALYSIS OF BROADBAND EARTHQUAKE DATA

by

M. SCOTT BAKER

Major Professor:	Robert B. Hawman
Committee:	Douglas E. Crowe Michael F. Roden

Electronic Version Approved:

Maureen Grasso
Dean of the Graduate School
The University of Georgia
May 2006

ACKNOWLEDGEMENTS

I would like to acknowledge the Joseph W. Berg Scholarship in Geophysics which provided funds to purchase the necessary equipment for processing and analysis, allowing for a more efficient and streamlined environment in which to conduct this research.

Support from the NSF (grant #0124249) in the form of hourly work helped lay the groundwork for the receiver function analysis of the Murphy and Godfrey seismic data.

I would like to thank Rob Hawman for his guidance, thoughtful input, and encouragement. I would also like to acknowledge Rob Hawman for the software he developed for moveout corrections, stacking, and the Zhu-Kanamori analysis. I would like to thank my loving wife Caryl for her patience and tolerance with me throughout the entire process. My parents, of course, who always believed I would succeed and gave me the opportunity to do so.

TABLE OF CONTENTS

Page

LIST OF TABLES

Page

LIST OF FIGURES

Page

Chapter 1

Introduction

This study was conducted to investigate the crustal structure of the Blue Ridge Mountains of North Carolina and the Carolina Terrane in Georgia. The main goal of the research was to test the hypothesis that the Blue Ridge Mountains are supported by a crustal root, by estimating the thickness and average composition of the crust as inferred from seismic waves.

Previous geophysical studies in the region include seismic reflection profiles (Hatcher *et al.*, 1987; Nelson *et al.*, 1987) and refraction/wide-angle reflection profiles (Dorman, 1972; Kean and Long, 1980; Prodehl *et al.*, 1984; Hawman, 1996, 2004). The reflection profiles have recovered fairly detailed images of the upper 5–10 km but show much weaker, less continuous reflections below 10 km, because differential travel times are too small to resolve velocities at those depths. Beneath most of the profiles, events interpreted as possible Moho reflections are particularly weak. The refraction profiles show clearer reflections from the lower crust and Moho and have provided important constraints on P–wave and S–wave velocity structure at all depths within the crust, but the velocity estimates represent lateral averages along the relatively long (20–200 km) raypaths sampled.

The present study, which uses teleseismic P–waves converted to S–waves at the Moho, was carried out to fill some of the gaps in coverage left by earlier experiments. In contrast with conventional vertical–incidence reflection profiles (*e.g.* COCORP), the differential travel times observed for teleseismic recordings are large enough to yield velocity information for the whole crust. Moreover, receiver functions (Langston, 1979) sample the crust in a fairly narrow cone

beneath a broadband station and therefore (in principle) can yield better lateral resolution of structure than long–range refraction profiles.

The recordings of teleseisms are deconvolved to remove complicated waveforms generated by the finite source area and extended duration of fault motion. The result is a "receiver function" that consists of a series of well defined pulses corresponding to P–S conversions and reverberations within the crust. The relative timing of these pulses is used to place constraints on average V_P/V_S and total crustal thickness beneath the seismic station. V_P/V_S ratios then are compared with laboratory measurements of velocities for rocks of various compositions and metamorphic grade to place constraints on the average composition of the crust.

The structure of the crust was investigated with receiver function analysis of broadband seismic data from two permanent seismic stations operated by the United States National Seismic Network, USGS National Earthquake Information Center (NEIC). The results provide new calculations of crustal thickness and V_P/V_S beneath the two stations and allow for a comparison with previous results. Particular emphasis is placed on the analysis of data for earthquakes at different distances and azimuths from each station to help assess the importance of lateral variations in structure.

Chapter 2

Background

Geologic setting

The Appalachian orogen formed along the eastern margin of the North American craton (Laurentia) as the result of a complex series of Paleozoic tectonic events that included collisions with Africa and Europe (Keller and Hatcher, 1999). The orogenic history of the region includes assembly and accretion of multiple terrains along the eastern margin of Laurentia during the Taconic (Middle Ordovician–Middle Silurian), Acadian (Middle Devonian–Early Mississippian), and Alleghanian (Late Mississippian–Permian) orogenies (Thomas, 2004). The orogenies are recorded on both the east and west coast of the North Atlantic and are related to the opening (late Proterozoic), closing (mid–Ordovician to Permian), and reopening (Mesozoic) of the Atlantic Ocean basin (Musacchio *et al.*, 1997).

The southern and central Appalachian Mountains are divided into geologic provinces that, from east to west are the (1) Atlantic Coastal Plain, (2) Carolina Terrane (containing the Charlotte, Kiokee, Belair, and Carolina Slate belts), (3) Inner Piedmont, (4) Blue Ridge, (5) Valley and Ridge, and (6) Cumberland Plateau (Peavey *et al.* 2004). The Brevard Zone is a large linear feature that separates the Blue Ridge province from the Inner Piedmont. The zone extends from Virginia to Alabama and has been interpreted as a brittle-ductile shear zone with a long and complex history (Edelman et al., 1987). The geologic provinces are distinguished from one another on the basis of tectonic style, metamorphic grade, and origin of the rocks. The focus of this study is on the Blue Ridge Mountains and the Carolina Terrane. Figure 1 shows the location of the seismic stations and the geologic provinces of the area.

The southern Appalachian Blue Ridge is composed of an assemblage of crystalline metasedimentary, clastic sedimentary, and metavolcanic rocks, as well as granitic plutons and ultramafic igneous rocks (Hatcher *et al.*, 1989 ; Peavey *et al.*, 2004; Hopson *et al.*, 1989; Hatcher and Odom, 1980). The eastern Blue Ridge is predominately igneous and metavolcanic, while the western Blue Ridge is characterized by mostly non-volcanic sequences (Hopson *et al.*, 1989). The structure of the Blue Ridge is complex, reflecting the effects of multiple episodes of folding, faulting, and high–grade metamorphism during the Acadian, Taconic, and Alleghanian orogenic events (Settles *et al.*, 2002; Hatcher *et al.*, 1989; Hatcher and Odom, 1980). Undeformed and unmetamorphosed diabase dikes cut the structures in the area, providing evidence of Mesozoic rifting that produced the modern Atlantic Ocean (Hopson *et al.*, 1989; Valentino and Gates, 2001).

The long and complex history of the Brevard Zone includes both strike-slip and dip-slip motion (Edelman et al., 1987). The most recent displacements (late Alleghanian) that are well documented along the Brevard Zone involved thrust faulting along a series of planes referred to collectively as the Rosman Fault (Edelman et al., 1987). This fault zone may have been reactivated as an extensional zone during the Triassic. The Inner Piedmont consists of high grade metamorphic rocks (upper amphibolite facies) that include migmatites and small amounts of quartzite, amphibolite, and metagabbro. Metamorphic grade is higher than in the Carolina Terrane and deformation is more intense (Griffin, 1971). The Carolina Terrane consists of the Belair, Kiokee, Charlotte, and Carolina Slate belts. Rocks include clean to impure metasandstones and metagreywackes, pure to impure carbonates, metaconglomerates, metapelites, and felsic and mafic volcanic rocks with plutons ranging from ultramafic to granitic (Rogers, 1970). The Inner Piedmont and Carolina Terrance are structurally complex containing both folds and exposed faults that were ductile during the early stages of their evolution (Peavey

et al., 2004) and several faults in the eastern part also record a brittle movement history (Hatcher and Odom, 1980; Secor *et al.*, 1986).

Previous geophysical studies

The southern Appalachians have been studied with reflection and refraction seismic studies as well as gravity surveys. Figure 2 shows the Bouguer gravity anomaly data from the USGS (Phillips et al., 1993) with the location of the stations and the approximate area sampled by the arrivals.

Consortium for Continental Reflection Profiling (COCORP) results

COCORP was the first large-scale reflection study of the southern Appalachians and it helped to confirm the model of thin-skinned tectonics for this area. Much of the study focused on investigating the detachment faults and thrust sheets that underly the Blue Ridge, Inner Piedmont, and Carolina Terrane (Hatcher, 1986; Cook et al., 1979).

The results of COCORP profiling show a series of clear, continuous reflections to a depth of approximately 10 km and much weaker, less continuous reflections from the rest of the crust and Moho. Along COCORP Line #1 at the southern end, flat reflections that appear around 11 – 12 s may represent reflections from the Moho (Cook et al., 1979), but elsewhere along the profile these reflections are not present, and the sections show only a few reflections within basement rocks (Nelson et al., 1987). Layered reflections at 1.7 to 2.0 s (5 to 6 km) in the Valley and Ridge and Blue Ridge section of the profile are interpreted as a boundary between crystalline and sedimentary rocks, but reflections at depths that could be interpreted as the Moho are sparse. The shallower reflections have been traced to the surface and directly related to units in the Valley and Ridge (Hatcher et al., 1987). The profiles show eastward dipping reflections that are prominent throughout. Travel times increase from 1.7–2.0 s (5–6 km) beneath the Blue Ridge to 3.0–4.0 s (9–12 km) beneath the Inner Piedmont. These reflections have been interpreted as a

decollement, or thrust sheets of allochthonous crystalline rocks overlying sedimentary rocks which supports the thin-skinned tectonic model in the southern Appalachians (Cook et al., 1979; Iverson and Smithson, 1983). To the southeast, beneath the Carolina Terrane and Coastal Plain, these reflections become weaker and the geological interpretation is more controversial (Cook *et al.*, 1979; Iverson and Smithson, 1983).

Appalachian Ultra-Deep Core Hole (ADCOH) site study

The quality of the seismic data and the resolution from ADCOH profiles is much better than that from the COCORP profiles. ADCOH Line 3 is in the Blue Ridge and runs from northwest to southeast in North Carolina, northeast Georgia, and South Carolina. ADCOH Line 1 crosses the Brevard Zone and runs NW–SE in the Inner Piedmont. The rocks of the Inner Piedmont are more reflective than those of the Blue Ridge allowing the Brevard Zone to be well defined. Strong reflections beginning at 0.8 s (2.3 km) on the western end of ADCOH Line 3 and at 1.0 s (2.9 km) on the eastern end are interpreted as a thick sequence of tectonically imbricated sediments beneath the Blue Ridge crystalline thrust sheet and constrain the thickness of the thrust sheet to 2 or 3 km (Coruh et al., 1987). Reflections within the basement are observed at 5–9 s (15–27 km) and around 11–13 s (33–40 km, assuming an average velocity of 6.0 km/s) along both profiles but are not as strong as the shallow reflections. The interval and average velocities derived from the data are 4.2 to 6.5 km/s and 5.2 to 5.6 km/s respectively (Coruh et al., 1987). Average unit thicknesses of 0.9 to 1.2 km are resolved in the upper portion of the profile and are interpreted as representing Paleozoic shelf strata. Reflections around 2.3 s in the Inner Piedmont along ADCOH Line 1 constrain the maximum thickness of the thrust sheet to 7 km (Hubbard et al., 1991). Deeper reflections within Grenville basement rocks are locally high in amplitude but not as continuous. A westward thickening of the crust (from 36 to 42 km) has been suggested based on reprocessing of Seisdata, COCORP, and ADCOH profiles

(Hubbard et al., 1991). The deepest reflections at 14–15 s occur at the northwest end of ADCOH Line 3. The corresponding depth based on an assumed average crustal velocity of 6.0 km/s (Hubbard et al., 1991) is 45 km, but this should be treated as a minimum estimate because the average velocity of the crust may be much greater (see below).

Seismic refraction/wide–angle reflection profiles

Refraction/wide–angle reflection profiling is carried out with much longer recording arrays than conventional reflection profiling (Braile and Chiang, 1986). The advantages of the expanded geometry are two–fold: (1) the wide range of recording distances allows recovery of larger differential travel times, yielding better resolved estimates of deep crustal velocities, and (2) reflection coefficients become quite large as angles of incidence approach the critical angle, yielding higher–amplitude reflections.

Dorman (1972) estimated crustal velocities of 6.2 km/s and mantle velocities of 8.2 km/s in the Inner Piedmont using timed quarry blasts. Kean and Long (1980) used arrivals from southeastern earthquakes and untimed explosions to find crustal thickness estimates throughout the southern Appalachians. Estimates for the Blue Ridge range from 40 km to 71 km in North Carolina and from 40 to 54 km in NW Georgia and SE Tennessee. Inner Piedmont and Carolina Terrane crustal thickness is estimated to be 33 km.

Prodehl *et al.* (1984) modeled crustal thicknesses in the range of 49–50 km in the Blue Ridge with a thickening to the northwest into the Interior Low Plateaus in Tennessee to about 49–55 km. Their derived models consisted of a three–layer crust with high velocities (6.1–6.2 km/s, 6.7–6.8 km/s, and 7.1–7.4 km/s for upper, middle, and lower crust respectively) as well as transition zones between the layers and the crust–mantle boundary ranging from 2 to 11 km in thickness. They also note that the COCORP data for the southern Appalachians typically do not have reflections deeper than roughly 10 s TWT in the Blue Ridge, and between the Valley and

Ridge and Inner Piedmont reflections below 4–5 s are absent. More recent refraction/wide–angle reflection profiles in the Carolina Terrane of Georgia (Hawman, 1996) suggest a crustal thickness of 37–39 km with an average V_P for the crust between 6.5 and 6.6 km/s. V_P/V_S ratios estimated from travel time ratios of S and P arrivals range between 1.72 and 1.75, suggesting an intermediate average composition for the crust. Preliminary analysis of wide–angle reflection data in the Blue Ridge Mountains of Georgia, South Carolina, and North Carolina suggests a crustal thickness of approximately 50 km along the southeast flank of the Blue Ridge Mountains in South Carolina (Hawman *et al.*, 2005).

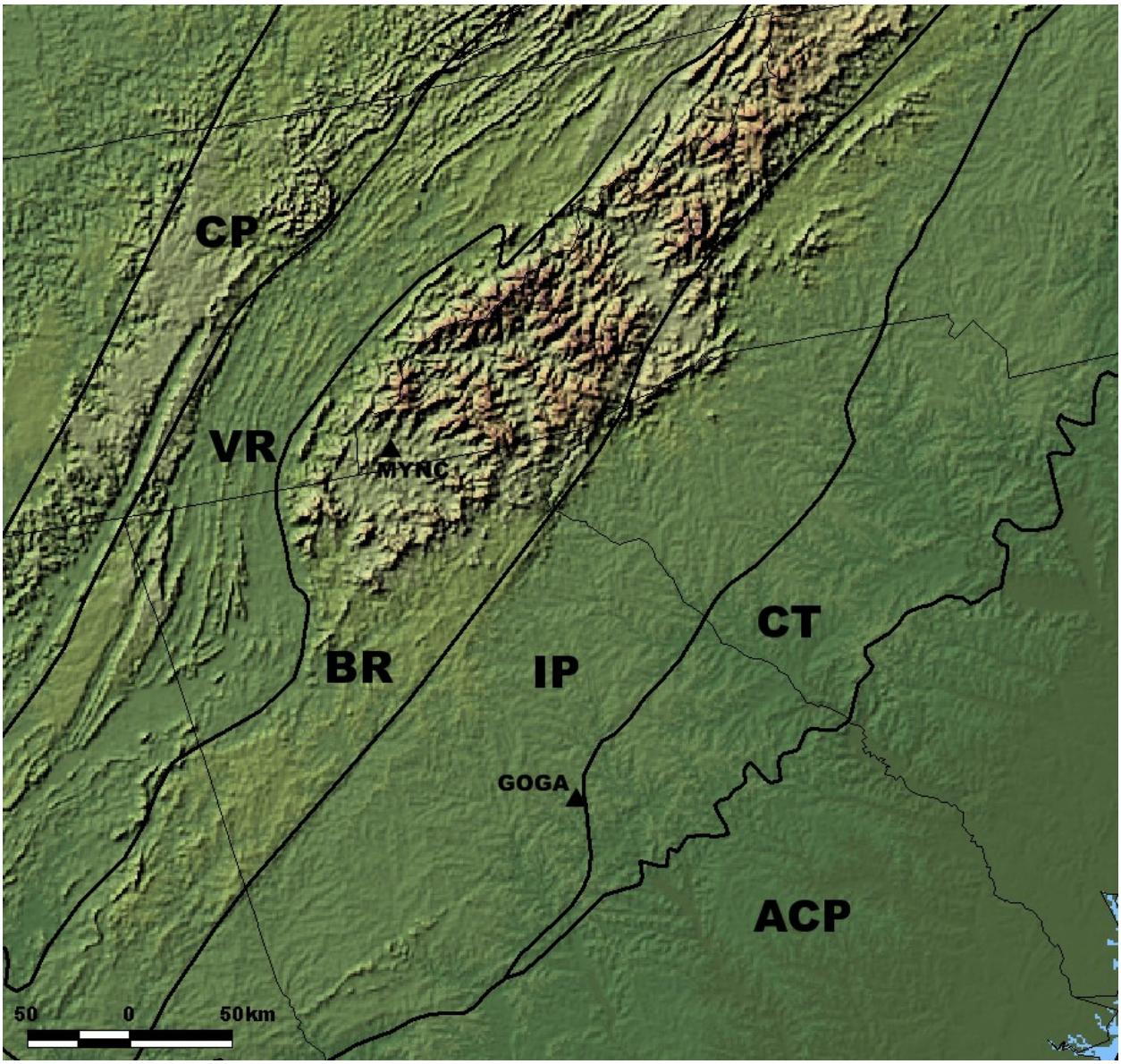

Figure 1: Shaded relief map of the study area showing the location of the broadband seismic stations in Murphy, NC (MYNC) and Godfrey, GA (GOGA) and the geologic provinces of the southern Appalachian mountains (ACP=Atlantic Coastal Plain, CT=Carolina Terrane, IP=Inner Piedmont, BR=Blue Ridge, VR=Valley & Ridge, CP=Cumberland Plateau) (Hatcher, 1989). Base map is the Shaded Relief Land – Color – 1 Kilometer Resolution from the National Atlas of the United States (http://www.nationalatlas.gov).

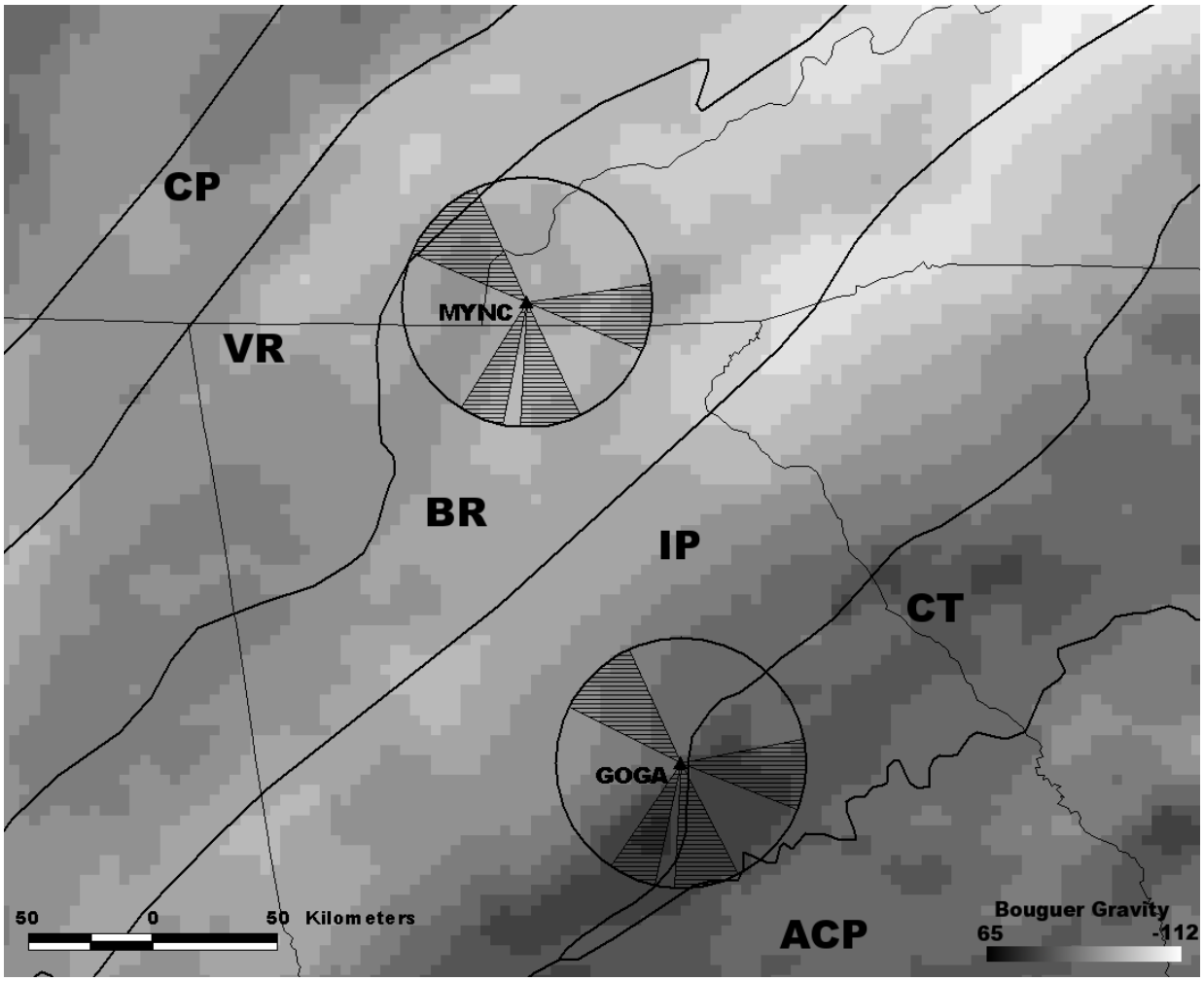

Figure 2a: Bouguer gravity anomaly map showing the location of the broadband seismic stations, the azimuthal ranges sampled by the incoming teleseismic waves, and the geologic provinces of the southern Appalachian mountains from Figure 1 (ACP=Atlantic Coastal Plain, CT=Carolina Terrane, IP=Inner Piedmont, BR=Blue Ridge, VR=Valley & Ridge, CP=Cumberland Plateau). Gravity data obtained from the USGS Digital Data Series DDS–9 (Phillips *et al.*, 1993)

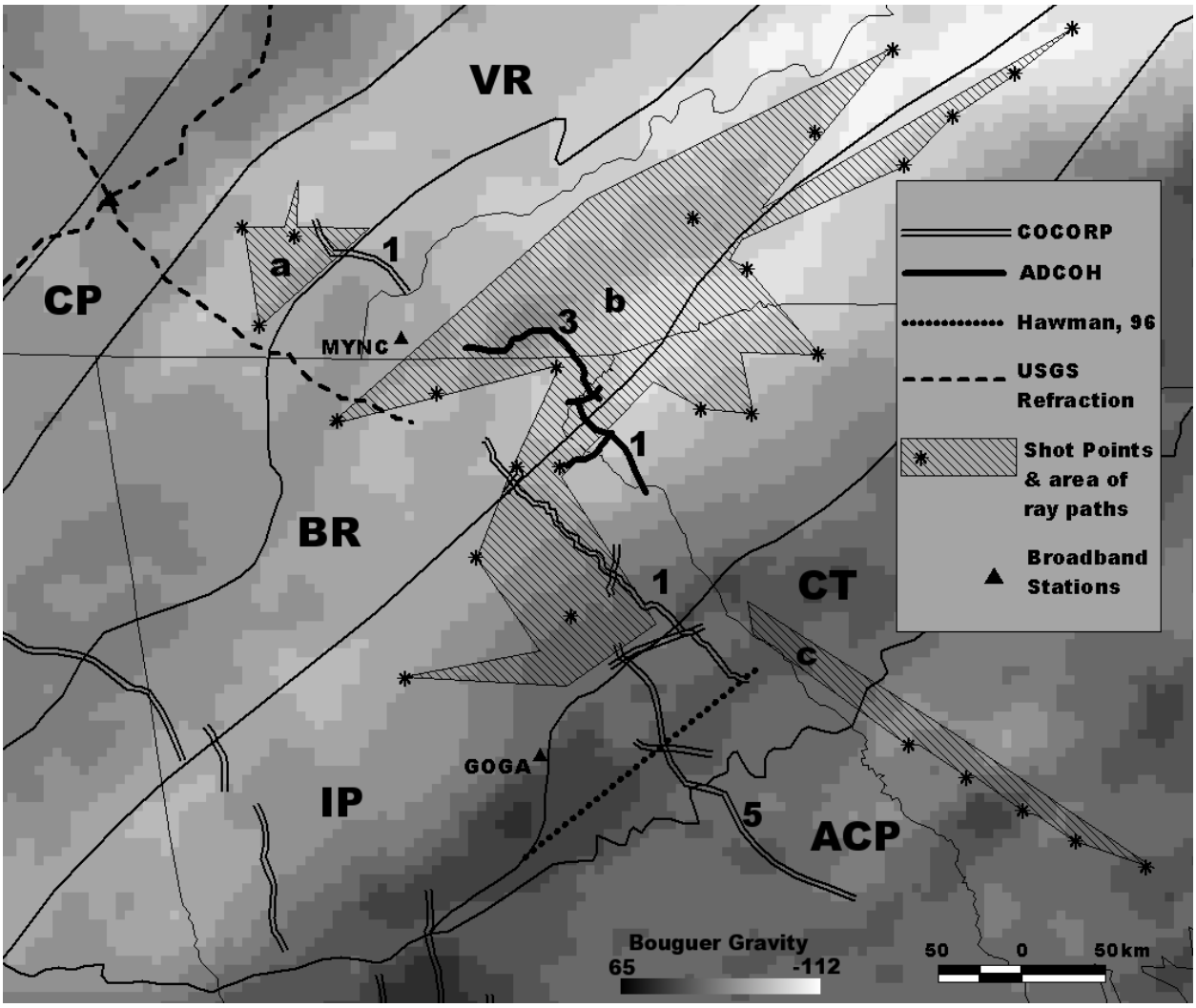

Figure 2b: Bouguer gravity anomaly map showing previous geophysical study locations and the geologic provinces of the southern Appalachian mountains from Figure 1 (ACP=Atlantic Coastal Plain, CT=Carolina Terrane, IP=Inner Piedmont, BR=Blue Ridge, VR=Valley & Ridge, CP=Cumberland Plateau). Shot points and area of ray paths are from (a) Hawman et al. (2001), (b) Hawman et al. (2005), and (c) Hawman (1991, unpublished data). Numbers refer to the relevant ADCOH and COCORP profiles.

Chapter 3

Receiver Function Analysis

Recordings of earthquakes can be difficult to interpret because of the extended waveforms generated by long–duration slip and reverberations near the source region. This results in a substantial amount of overlap in the waveforms for individual arrivals (direct P wave, P–to–S conversions, and reverberations within the crust). The generation of a "receiver function" involves the deconvolution or removal of this extended source pulse to improve the resolution of individual arrivals (Langston, 1979). The timing of the principal arrivals in a receiver function varies in a systematic way with distance from the epicenter. This variation in travel time can be used to constrain the average P–wave and S–wave velocity structure beneath the station. These regular variations are disturbed by lateral variations in structure. This fact was taken into account when searching for events, and event data were gathered from a number of azimuths to investigate this effect.

Acquisition of data

The events used in the analysis were found with the program JWeed obtained from the Incorporated Research Institutes in Seismology (IRIS). JWeed is the Java version of the X–windows program Windows Extracted from Event Data (WEED). The user selects an area from an interactive map of the world and specifies event parameters and stations of interest. The seismic stations used were from the US National Network (US) and are located in Murphy, NC (MYNC) and Godfrey, GA (GOGA). The event parameters specified were events greater than 5.7 magnitude with distances between 25º and 110º away from each of the stations. A search for events in various azimuthal ranges for the two seismic stations resulted in earthquakes from the

south (SA) in South America, the northwest (NW) in the Aleutians, Alaska, and Japan, the east (EAST) along mid ocean ridges in the Atlantic, the northeast (NE) in the Mediterranean and Europe, the south–southwest (SSW) along the East Pacific Rise, and the west (WEST) in the Fiji/Tonga area. Once events are located and stations selected, JWeed creates a summary file and an event request file. The event request files were submitted to the IRIS Data Management Center (DMC) via email. The requested events were extracted and made available for download via file transfer protocol (FTP). Once the queries were returned, the headers (comment fields) for each trace were updated with the event information that allowed for the calculation of azimuth, distance, and great circle arc parameters needed for the rotation of the traces. The number of usable events from each azimuthal range varied and was largely influenced by the tectonics associated with the earthquakes (*e.g.* subduction zones produced better event data than mid–ocean ridges or transforms).

Preliminary processing

The program Seismic Analysis Code (SAC) developed by the Lawrence Livermore National Lab (LLNL) was used to process the raw seismic traces for input into the computation of the receiver functions. Various filtering parameters were tested in SAC to determine the optimal values for processing the traces to eliminate unwanted noise. Once a filter setting was found that looked adequate for viewing the traces (highpass filter with a corner frequency at 0.05 Hz), the traces were processed and usable events were sorted out from unusable events with a SAC macro based on the signal–to–noise level and the quality of the direct P wave arrival. Processing of the traces consisted of "windowing" (extracting a time window of) the data so that the vertical (Z), north (N), and east (E) component traces for each event were the same length, removing the mean and linear trend from the traces, bandpass filtering, and rotating the N and E components into the theoretical radial (R) and transverse (T) components. This was done in

SAC with a macro that was written to systematically process the traces one after another with input from the user to determine the time of the initial P–wave arrival. The window chosen was 30 seconds before and 90 seconds after the initial P arrival. The ray parameters for each event were calculated for use in the moveout corrections and the $H - \kappa$ stacking described below. Using the event distance and source depth, ray parameters were computed using the IASP91 model of the Earth (Kennett and Engdahl, 1991). The ray parameter (Figure 3 (b), inset) is related to the angle of incidence of the P wave:

$$p = \frac{\sin(\theta_1)}{V_{P_1}} = \frac{\sin(\theta_2)}{V_{P_2}} = \frac{\sin(\delta_1)}{V_{S_1}} = \frac{\sin(\delta_2)}{V_{S_2}} \quad (1)$$

where θ_1 is the angle of incidence of the incoming P wave, θ_2 is the angle of the refracted P wave, δ_1 is the angle of incidence of the incoming S wave, δ_2 is the angle of the refracted S wave, V_{Pi} are the P wave velocities, and V_{Si} are the S wave velocities.

Computation of receiver functions

Receiver function analysis has been used with success to image major discontinuities in the crust and uppermost mantle and to place constraints on average P and S velocities (Langston, 1979; Owens and Zandt, 1985; Ammon, 1991; Zandt et al., 1995; Zhu and Kanamori, 2000). A receiver function is a time series waveform computed from three–component broadband seismic data that shows how seismic waves respond to the Earth structure around a particular seismic station (Langston, 1979). It consists of a direct P wave along with a P–to–S conversion (P_S) at the Moho and multiple converted phases (for instance P_PP_S and P_PS_S+P_SP_S) from reverberations in the crust beneath the station (Figure 3 (b)).

The particle velocities, or the displacement as a function of time, for a planar P wave incident on a stack of horizontal or dipping interfaces are given by:

$$D_Z(t) = I(t) * S(t) * E_Z(t) \quad (2)$$

$$D_R(t) = I(t) * S(t) * E_R(t) \tag{3}$$

$$D_T(t) = I(t) * S(t) * E_T(t) \tag{4}$$

where *S(t)* is the effective source–time function of the incoming wave (the shape of the pulse propagated away from the source region, with a duration determined by the duration of slip and degree of reverberation in the source region), *I(t)* is the instrument impulse response, $E_Z(t)$, $E_R(t)$, and $E_T(t)$ are the vertical, radial, and transverse Earth structure impulse responses directly beneath the station, and * represents convolution (Langston, 1979). The source–time function can be complicated, especially for large, shallow earthquakes (Langston, 1979). A key assumption can be made that for steep angles of incidence (corresponding to events with a distance greater than 30°, Figure 3 (a)), the Z component will consist almost entirely of P waves, mostly the direct P wave (Langston, 1979) but also P–wave reverberations (Ammon, 1991). The radial and transverse components of motion will contain mostly shear waves, including P_S (the P wave converted to a shear wave at the Moho) and S–wave reverberations. Therefore:

$$D_Z(t) = I(t) * S(t) * E_Z(t) \simeq I(t) * S(t) \tag{5}$$

The convolution in the time domain is equivalent to multiplication in the frequency (ω) domain, so the receiver function for the radial component in the frequency domain is given by:

$$E_R(\omega) = \frac{D_R(\omega)}{I(\omega)S(\omega)} \simeq \frac{D_R(\omega)}{D_Z(\omega)} \tag{6}$$

That is, dividing the spectrum of the radial–component trace by the spectrum of the vertical–component trace is equivalent to dividing by the spectra of the instrument response and source–time function. This removes these complicating effects, leaving a series of pulses that represent P–S conversions and S–wave reverberations at major interfaces beneath the seismic station. Likewise, the receiver function for the transverse component is given by:

$$E_T(\omega) = \frac{D_T(\omega)}{I(\omega)S(\omega)} \simeq \frac{D_T(\omega)}{D_Z(\omega)} \quad (7)$$

assuming that the instrument response $I(\omega)$ is the same for all components. Values of $D_Z(\omega)$ that are approximately zero cause instabilities in the computation of the receiver function, so small values in the denominator are replaced with a fraction of the maximum value of the denominator. This fraction is known as the water-level parameter. It dampens the effect of small amplitude frequencies on the Z component. The level of detail that is present in the receiver function is controlled by the Gaussian parameter (alpha). Alpha is a low–pass filter that limits the frequency content and smooths the output receiver function based on the level chosen. Decreasing alpha increases the amount of smoothing of the output waveform.

Receiver functions were generated using the Computer Programs in Seismology version 3.30 software package from St. Louis University. Tests were run on various traces to determine the optimal values for the water–level parameter and alpha. Values tested for the water–level parameter were 0.0001, 0.001, 0.01, and 0.1. Values chosen for alpha ranged between 0.5 and 2.0. The optimal setting for the water level was 0.01 based on the quality of the resulting receiver functions. Four Gaussian values (0.5, 1.0, 1.5, and 2.0) were used for computing the final receiver functions.

Once the receiver functions were computed, gathers (multi-trace plots) of receiver functions were created based on azimuth using Seismic Unix (SU), maintained by the Colorado School of Mines. Creating multitrace gathers of receiver functions makes it possible to identify important arrivals based on waveform coherence. Moreover, it is possible to distinguish between conversions and multiples based on their moveout (variation in travel time with distance) characteristics, as travel times for P_S conversions decrease with distance from the epicenter, while travel times for multiples increase with distance (see below). Additional filtering was

done in SU to eliminate low frequency noise in some of the traces. To determine the optimal filter setting, low frequencies were filtered out in stepwise fashion until ringing in the data began, allowing for the location of the best filter setting.

H – κ stacking

The H – κ stacking method (H = Moho Depth and $\kappa = V_P/V_S$) developed by Zhu and Kanamori (2000) was used to estimate the thickness and composition of the crust. With this technique, the receiver functions are stacked using an algorithm that sums the receiver function amplitudes at predicted arrival times of converted and later multiple phases (P_S, P_PP_S, and $P_SP_S+P_PS_S$), transforming them from the time–ray parameter domain into the H – κ domain. This approach assumes a one–dimensional structure and an average V_P for the crust.

The travel time differences between the direct P arrival and the other arrivals are calculated following Zandt *et al.* (1995):

$$t_1 = t_{Ps} - t_P = h[(V_S^{-2} - p^2)^{1/2} - (V_P^{-2} - p^2)^{1/2}] \quad (8)$$

$$t_2 = t_{PpPs} - t_P = h[(V_S^{-2} - p^2)^{1/2} + (V_P^{-2} - p^2)^{1/2}] \quad (9)$$

$$t_3 = t_{PsPs+PpSs} - t_P = 2h\left(\frac{1}{V_S^2} - p^2\right)^{1/2} \quad (10)$$

where h is the crustal thickness, V_P and V_S are the average crustal P and S velocities, and p is the ray parameter in s/km from equation (1). The P_S and P_PP_S branches have a positive polarity on the receiver function trace while the $P_PS_S+P_SP_S$ branch has a negative polarity. The moveout (time versus distance) behavior for the P_S branch is different than that for the multiples. The P_S branch has a negative slope (closer events have a greater time difference between P and P_S than further events) and the multiples have a positive slope (closer events have a smaller time difference).

The H – κ stack is given by:

$$s(H,\kappa)=\sum_{i=1}^{np}(w_1 r_i(t_1)+w_2 r_i(t_2)-w_3 r_i(t_3)) \quad (11)$$

where $r_i(t)$ is the radial receiver function for a given ray parameter, *np* is the number of ray parameters (number of receiver function traces) in the input gather, and t_1, t_2, and t_3 (equations (8)–(10)) are the travel time differences computed for trial values of H, V_P, and V_P/V_S (κ). The parameters w_1, w_2, *and* w_3 are weights assigned to each phase, with the constraint that

$$w_1+w_2+w_3=1 \quad (12)$$

The summation is repeated over a range of values for H and κ (V_P is held fixed) and the results are plotted and contoured. The best estimate of crustal thickness and V_P/V_S is where all the phases (P_S, P_PP_S, and $P_SP_S+P_PS_S$) coherently stack. V_P/V_S can then be used to estimate the average composition of the crust based on studies of seismic wave velocities in rocks and minerals (Christensen and Mooney, 1995; Christensen, 1996; Musacchio *et al.*, 1997).

It is necessary to assign weights (w_1, w_2, *and* w_3) to the converted and multiple phases when applying the H – κ stacking method as well as a value for V_P. The weights are assigned based on the coherence of the phases in the receiver functions and more weight is given to those phases that are easily identified. The weighting used for the stacks shown in Appendix C was w_1=0.34, w_2=0.33, and w_3=0.33. To evaluate the sensitivity of the stacking results to the choice of weights, other combinations were tested as well. The value of V_P was varied from 6.1 km/s to 6.9 km/s in increments of 0.1 km/s to yield 9 separate H – κ stacks for each azimuth and alpha setting. The depth range (H) was 20 – 80 km in 100 m increments and the V_P/V_S range (κ) was from 1.500 – 2.200 in 0.001 increments. By repeating the stacking over a range of plausible values for V_P, it was possible to evaluate the effect of V_P on the tradeoff between V_P/V_S and crustal thickness. Appendix C shows all of the results for the H – κ stacking.

Simple stacks of receiver functions

The receiver functions in each gather were time-shifted to correct for moveout and then stacked (summed) to evaluate the coherence of the arrivals and to help eliminate noise. The reference ray parameter for the moveout correction was 0.06 s/km (corresponding to a shallow source about 60º away). Different values for H, V_P, and V_S were used for each azimuth based on the peaks seen in the H – κ stacks (Appendix C; Tables 1 and 2). Predicted arrival times of the converted and multiple phases for an average reference model are shown on the stacks to allow for a quick comparison of results for different azimuths. For station MYNC, two reference models were used to account for the uncertainty in V_P. Parameters for the first reference model are H=50 km, V_P=6.3 km/s, V_S=3.6 km/s, and V_P/V_S=1.750. Parameters for the second reference model are H=52 km, V_P=6.5 km/s, V_S=3.7 km/s, and V_P/V_S=1.756. For station GOGA, the average crustal V_P is constrained by refraction results (Hawman, 1996), so only one reference model was used (H=42 km, V_P=6.5 km/s, V_S=3.7 km/s, V_P/V_S=1.756).

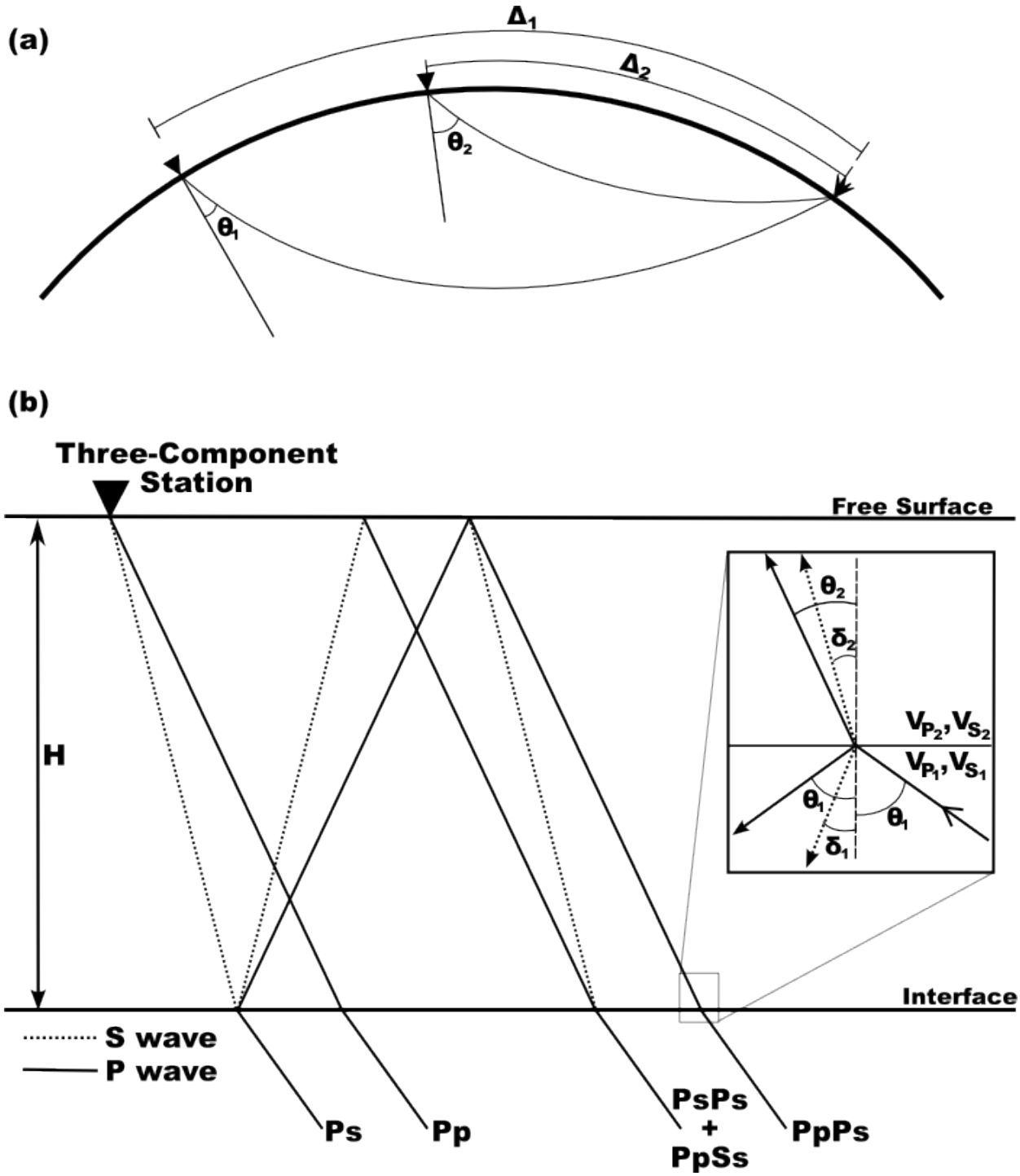

Figure 3: Ray path diagrams. (a) Ray paths showing the relationship between the distance from the station (Δ) and angle of incidence (θ). (b) Ray path diagram showing phases and ray parameter definition.

Chapter 4

Results of Receiver Function Analysis

Appendix A contains a list of events for MYNC and GOGA and a map showing the location of the stations and events, Appendix B shows the gathers of receiver functions, and Appendix C shows the results of the $H - \kappa$ stacking. Figure 4 is a typical example of the computed receiver function for the various Gaussian settings. The converted phase as well as multiple phases are shown, and the low level of noise is apparent by examining the 20 seconds before the direct P wave arrival. The arrivals are seen as distinct peaks in the trace and comparing these with the entire trace shows that these arrivals are unique and are not the result of random noise.

An example of a gather of receiver functions is shown in Figure 5 with and without the normal moveout correction. These gathers and the ones in Appendix B are the input for both the $H - \kappa$ stacking and the simple stacking routines. The gathers show well defined phase arrivals that match the predicted arrivals as well as others that may be related to interfaces both within the crust and below the Moho. Determining whether a branch is a P_S conversion or a reverberation is done by examining the behavior of its moveout. In the gathers, conversions will have a negative slope (closer events will have a greater time difference) and reverberations will have a positive slope (closer events will have a smaller time difference). The moveout of the branches is best seen by looking at the first 50 s of the gathers rather than the entire 100 s (Figures B8, B9, and B10 (GOGA) and Figures B17 and B18 (MYNC)). This allows for the gather to be stretched out, which accentuates the effects of moveout on the branches.

Data issues

Not all of the azimuths investigated in this study yielded adequate results for use in the interpretation of crustal thickness and composition. The NE azimuth for MYNC yielded few traces with good signal to noise. The data from the NE azimuth for GOGA was slightly better than that for MYNC, but it was still noisier than the gathers for other azimuths. For MYNC, this may be related to scattering from the topography which the raypaths are arriving under or it could be caused by lateral variations at greater depths. The NE lacks the advantage of numerous large earthquakes at subduction zones. The $H - \kappa$ stacks from the NE azimuth for GOGA did not yield well defined peaks, but the simple stacks of receiver functions do show coherent arrivals for the conversion and multiples. The results of the $H - \kappa$ stacks and the simple stacks from the WEST azimuth for both MYNC and GOGA lack adequate events within the 100º cutoff. Raypaths from events at distances greater than 100º experience diffraction at the core–mantle interface which complicates the seismograms and the deconvolution is not as successful. Except for the simple stacks from the NE azimuth of GOGA, these two azimuths were left out of the interpretation. The results are made available in the appendices to show the quality of the data from these azimuths compared to the others.

The SA azimuth had the best signal–to–noise levels for both seismic stations. The NW azimuth had good signal–to–noise levels allowing for clear distinction of the branches, but the SSW and EAST azimuths have higher noise levels that began to interfere with arrivals in some cases. Plotting the receiver functions as multitrace gathers made it possible to evaluate the coherence of the arrivals in all cases and even allowed identification of other arrivals.

Resolution

A measure of horizontal resolution is given by the radius of the first Fresnel zone, which is that part of an interface that contributes energy to the first half cycle of the waveform. The radius of the first Fresnel zone is given by:

$$R_1 = \sqrt{\frac{\lambda H}{2}} = \sqrt{\frac{V H}{2 f}} \tag{15}$$

where λ is the dominant wavelength, H is the depth, V is the average velocity, and f is the dominant frequency (Sheriff and Geldart, 1982). The dominant frequency in the receiver functions is between 0.2 and 0.4 Hz, corresponding to a Fresnel zone radius of 15 – 22 km for an interface with a depth of 50 km and 13 – 19 km for an interface with a depth of 40 km (Figure 6). The limit of vertical resolution is generally assumed to be $\lambda/4$ (Sheriff and Geldart, 1982). For the data considered here, the thinnest resolvable layer is 2–3 km thick.

H – κ stacking results

Results for the $H - \kappa$ stacking for all azimuths for both stations are shown in Appendix C. Tables 1 and 2 list the V_P/V_S ratio and depth to Moho for each azimuth for both stations as well as the overall average for each station for a range of plausible values for V_P. The results from the $H - \kappa$ stacking method yielded well resolved estimates of thickness and V_P/V_S for most of the azimuths. For station MYNC, the SA, NW, EAST and SSW azimuths gave useful results, but the other azimuths (NE and WEST) did not because of the high noise levels. The NW, EAST, and SSW azimuths for station GOGA yielded results that are in agreement with previous studies, but the SA azimuth showed a much shallower Moho depth and a much higher V_P/V_S that is beyond the range of reasonable values for crustal rocks (Christensen, 1996).

Figure 7 demonstrates how sensitive the stacking is to the value of V_P. A variation of 0.2 km/s in V_P results in approximately a 2 km difference in thickness and a change in the V_P/V_S

ratio of 0.01. The stacking results are also affected by the weightings chosen for the phases. Figure 7 shows the stacking results when equal weights (w_1=0.34, w_2=0.33, w_3=0.33) for all three branches are used. In Figure 8, only the P_S arrival is used in the stacking (w_1=1, w_2=0, w_3=0). A broad band of depths and V_P/V_S ratios is possible and the tradeoff between the two is clearly demonstrated. Finally, Figure 9 shows a slight variation in the weightings (w_1=0.75, w_2=0.125, w_3=0.125). Here the peak is smeared out and is not as well defined as in the equal weighting stack, but the position of the peak is almost the same.

Simple stacks of receiver functions

Simple stacks of receiver functions compliment the results of the $H - \kappa$ stacking. Figures 10 and 11 are the stacks for station MYNC with different values for V_P. The reference ray parameter used for the moveout correction was 0.06 s/km (corresponding to a shallow source about 60º away). The values for V_P/V_S and H were taken from the $H - \kappa$ stacking results (Tables 1 and 2) for each azimuth to get the optimal moveout correction. In Figure 10, the moveout correction was done with V_P = 6.3 km/s and the predicted arrival times were calculated with V_P=6.3 km/s, V_S=3.6 km/s, V_P/V_S=1.750, and H=50 km. The moveout correction for Figure 11 was done with V_P = 6.5 km/s and the predicted arrival times were calculated with V_P=6.5 km/s, V_S=3.7 km/s, V_P/V_S=1.756, and H = 52 km. Figure 12 is the stack for station GOGA and the moveout correction was done with V_P = 6.5 km/s and the predicted arrival times were calculated with V_P=6.5 km/s, V_S=3.7 km/s, V_P/V_S=1.756, and H = 42 km.

On the simple stacks of receiver functions (Figures 10, 11, and 12), the calculated arrivals align well with the predicted arrivals. In Figure 12, the arrivals for station GOGA align well with the predicted arrival times suggesting the thickness is approximately 42 km. For both stations, there is a distinct side lobe that arrives between the direct P and the Moho conversion arrival and is smaller in amplitude. This is evidence of an inter crustal layer producing the

conversion. The arrival time of the side lobe is 2–3 s after the initial P wave arrival. The depth to this interface is about 19 km for GOGA (Figure C8) and about 16 km for MYNC (Figure C16). Hawman (1996) reported a midcrustal reflection around 24 km, which is significantly deeper than the midcrustal arrival for GOGA. The arrival at 16 km for MYNC is consistent with times for reflections observed in the ADCOH lines (Hubbard *et al*., 1991).

Previous receiver functions studies for the Cumberland Plateau (Zandt and Owens, 1986; Owens and Zandt, 1985) showed clear Moho P_S arrivals and associated multiples. The Moho P_S arrivals obtained for stations MYNC and GOGA are very clear and sharp (Figures 10–12). Multiples are clearly visible in the stacks and for some azimuths other P_S arrivals are apparent in the gathers. There are arrivals between the Moho P_S and the first multiple with a negative slope which indicates that this arrival is a conversion and not a multiple. There are arrivals that occur later in the traces with a negative slope which again indicate a conversion at an interface and not multiple energy. These later conversions are likely generated at discontinuities within the upper mantle given the timing of the arrivals. The arrival time for the topmost mantle discontinuity is about 16 s, which falls between the Moho conversion and the first multiple. For a model with average velocities of V_P=6.5 km/s (crust) and V_P=8.2 km/s (mantle), the depth to this interface is approximately 150–160 km. Two arrivals that show up later in the traces occur close to the predicted arrival times for the 400 km and 670 km discontinuities. All of these arrivals are best seen on the gather from the SA azimuth for station MYNC (Figures 6 and B13), but are also seen in others.

Lateral variations in structure beneath each station

As noted in Chapter 1, compared to other seismic methods, lateral averaging of velocities in the crust with receiver function analysis is greatly reduced. The lateral variation around each station is investigated by grouping arrivals into azimuths and finding the thickness and V_P/V_S for

each section of crust. For MYNC, there is a large amount of lateral variation along a NW–SE line. For the NW azimuth, the receiver functions show thicker crust and a higher V_P/V_S ratio than the other azimuths which sample crust to the south and east. The other azimuths are close to one another spatially and show only slight variations in velocity from one another. From the $H - \kappa$ stacks, there is a trend of crustal thickening from SSW–SA–EAST azimuths with roughly the same V_P/V_S ratio. This observation suggests that the variation is due to changes in crustal thickness and not changes in the composition of the crust being sampled.

The trend of crustal thinning to the SE around MYNC is also present around GOGA. The NW azimuth exhibits the thickest crust with the SA azimuth having the thinnest. Crustal thickness for the EAST azimuth is slightly less, but greater than the thickness for the SSW and SA azimuths.

Table 1: Thickness and V_P/V_S ratio from H – κ stacks for GOGA. The ranges of values were determined by zooming in on the chosen peak and finding the upper and lower values of the associated contour. The lower V_P/V_S goes with the higher H. The double entries are a result of double peaks in the H – κ stacks. Rock types with compatible Poisson's Ratio and V_P are defined as follows: BGN=biotite gneiss, PHY=phyllite, PGR=paragranulite, FGR=felsic granulite, DIO=diorite, GGN=granite gneiss (Christensen, 1996).

	V_P (km/s)	V_P/V_S Ratio	Thickness (km)	Poisson's Ratio	Rock Types
EAST	6.3	1.728 – 1.738	40.90 – 41.10	0.250 – 0.255	BGN
	6.4	1.724 – 1.736	41.66 – 41.94	0.245 – 0.250	GGN
	6.5	1.720 – 1.732	42.49 – 42.76	0.245 – 0.250	GGN
	6.6	1.713 – 1.729	43.28 – 43.64	0.240 – 0.250	GGN
SA	6.3	2.002 – 2.048	29.49 – 30.20	0.335 – 0.345	
	6.4	2.004 – 2.033	30.19 – 30.62	0.335 – 0.340	
	6.5	1.991 – 2.036	30.65 – 31.35	0.330 – 0.340	
	6.6	1.966 – 2.051	30.89 – 32.29	0.325 – 0.345	
SSW	6.3	1.750 – 1.791	39.05 – 40.06	0.260 – 0.275	BGN, PHY
	6.4	1.752 – 1.785	39.87 – 40.66	0.260 – 0.270	PGR
	6.5	1.755 – 1.777	40.70 – 41.22	0.260 – 0.270	FGR
	6.6	1.725 – 1.801	40.72 – 42.72	0.245 – 0.275	DIO
NW	6.3	1.741 – 1.757	41.34 – 41.79	0.255 – 0.260	BGN
	6.4	1.737 – 1.756	42.09 – 42.55	0.250 – 0.260	BGN
	6.5	1.734 – 1.752	42.88 – 43.32	0.250 – 0.260	BGN
	6.6	1.733 – 1.747	43.69 – 44.06	0.250 – 0.255	BGN
ALL	6.3	1.722 – 1.776 2.028 – 2.083	40.10 – 41.90 28.89 – 29.82	0.245 – 0.270 0.340 – 0.350	BGN, PHY
	6.4	1.721 – 1.769 2.022 – 2.079	40.94 – 42.62 29.44 – 30.43	0.245 – 0.265 0.340 – 0.350	PHY, PGR
	6.5	1.720 – 1.762 2.015 – 2.075	41.82 – 43.32 29.88 – 31.04	0.245 – 0.260 0.335 – 0.350	BGN
	6.6	1.720 – 1.754 2.008 – 2.070	42.74 – 43.99 30.52 – 31.67	0.245 – 0.260 0.335 – 0.350	BGN

Table 2: Thickness and V_P/V_S ratio from H – κ stacks for MYNC The ranges of values were determined by zooming in on the chosen peak and finding the upper and lower values of the associated contour. The lower V_P/V_S goes with the higher H. The double entries are a result of double peaks in the H – κ stacks. Rock types with compatible Poisson's Ratio and V_P are defined as follows: BGN=biotite gneiss, PHY=phyllite, PGR=paragranulite, FGR=felsic granulite, DIO=diorite, GGN=granite gneiss, BZE=zeolite facies basalt, BPP=prehnite-pumpellyite facies basalt, SLT=slate, DIA=diabase, QSC=mica quartz schist (Christensen, 1996).

	V_P (km/s)	V_P/V_S Ratio	Thickness (km)	Poisson's Ratio	Rock Types
		1.758 – 1.787	49.55 – 50.54	0.260 – 0.270	PHY, BGN
EAST	6.3	1.968 – 2.002	39.20 – 39.92	0.325 – 0.335	
		1.760 – 1.778	50.69 – 51.33	0.260 – 0.270	PGR
	6.4	1.962 – 2.001	39.89 – 40.75	0.325 – 0.335	
		1.759 – 1.772	51.73 – 52.23	0.260 – 0.265	FGR
	6.5	1.954 – 1.999	40.58 – 41.61	0.325 – 0.335	
		1.740 – 1.785	51.97 – 53.85	0.250 – 0.270	DIO
	6.6	1.947 – 1.995	41.30 – 42.42	0.320 – 0.330	
SA	6.3	1.749 – 1.770	49.35 – 50.12	0.255 – 0.265	BGN, PHY
	6.4	1.745 – 1.767	50.28 – 51.10	0.255 – 0.265	PGR
	6.5	1.742 – 1.762	51.24 – 52.05	0.255 – 0.260	
	6.6	1.738 – 1.758	52.20 – 53.02	0.255 – 0.260	
SSW	6.3	1.756 – 1.783	48.16 – 49.06	0.260 – 0.270	PHY, BGN
	6.4	1.756 – 1.774	49.25 – 49.90	0.260 – 0.265	
	6.5	1.745 – 1.776	49.98 – 51.10	0.255 – 0.270	
	6.6	1.744 – 1.768	51.09 – 51.93	0.255 – 0.265	
		1.814 – 1.852	59.75 – 61.27	0.280 – 0.295	SLT
NW	6.3	1.903 – 1.939	55.44 – 56.76	0.310 – 0.320	
		1.804 – 1.853	60.68 – 62.64	0.280 – 0.295	BZE
	6.4	1.896 – 1.939	56.34 – 57.96	0.305 – 0.320	
		1.806 – 1.842	62.16 – 63.62	0.280 – 0.290	BPP
	6.5	1.899 – 1.930	57.57 – 58.72	0.310 – 0.315	
		1.788 – 1.853	62.66 – 65.35	0.270 – 0.295	DIA
	6.6	1.882 – 1.939	58.16 – 60.38	0.305 – 0.320	
ALL	6.3	1.754 – 1.781	48.88 – 49.98	0.260 – 0.270	PHY
	6.4	1.753 – 1.776	49.82 – 50.80	0.260 – 0.270	PGR, QSC
	6.5	1.754 – 1.769	50.88 – 51.52	0.260 – 0.265	
	6.6	1.744 – 1.773	51.47 – 52.76	0.255 – 0.265	DIO

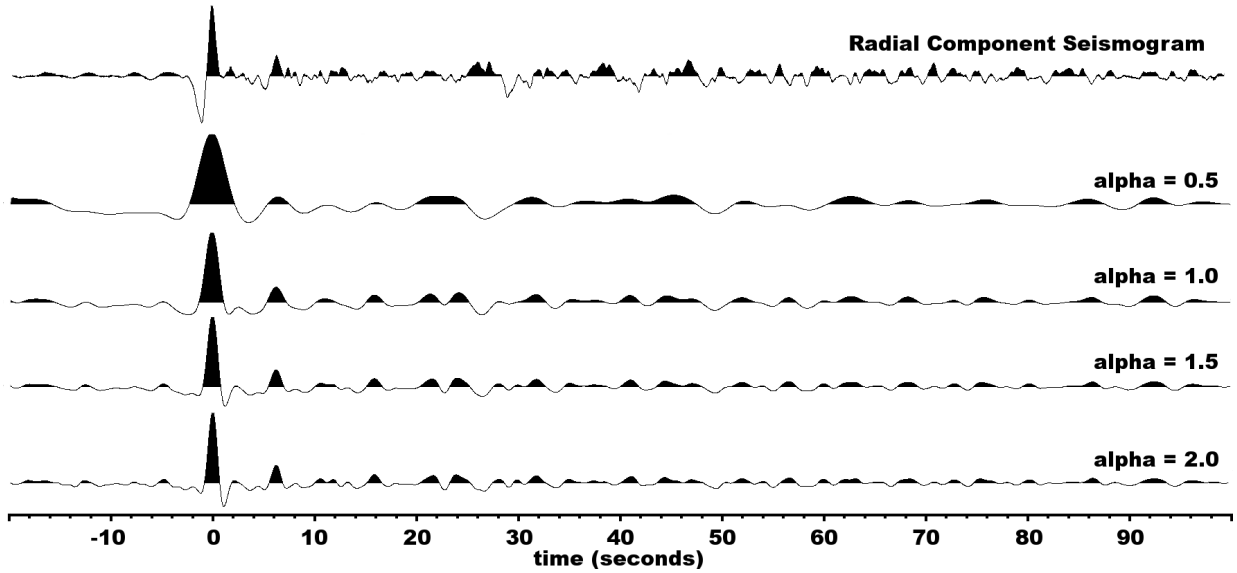

Figure 4: Example of a receiver function with varying Gaussian values (alpha) from station MYNC. The top trace is the radial component seismogram before the deconvolution. All traces are for the same event (2002, 267) from the SA azimuth. The event occurred at a distance of 43.72º away from the station and has a ray parameter of 8.00 s/degree (0.072 s/km). The raw seismic traces were bandpassed filtered with corner frequencies at 0.05 and 2 Hz, windowed, and the N and E components rotated to the theoretical radial and transverse components for computation of the receiver function. A water level of 0.01 was used.

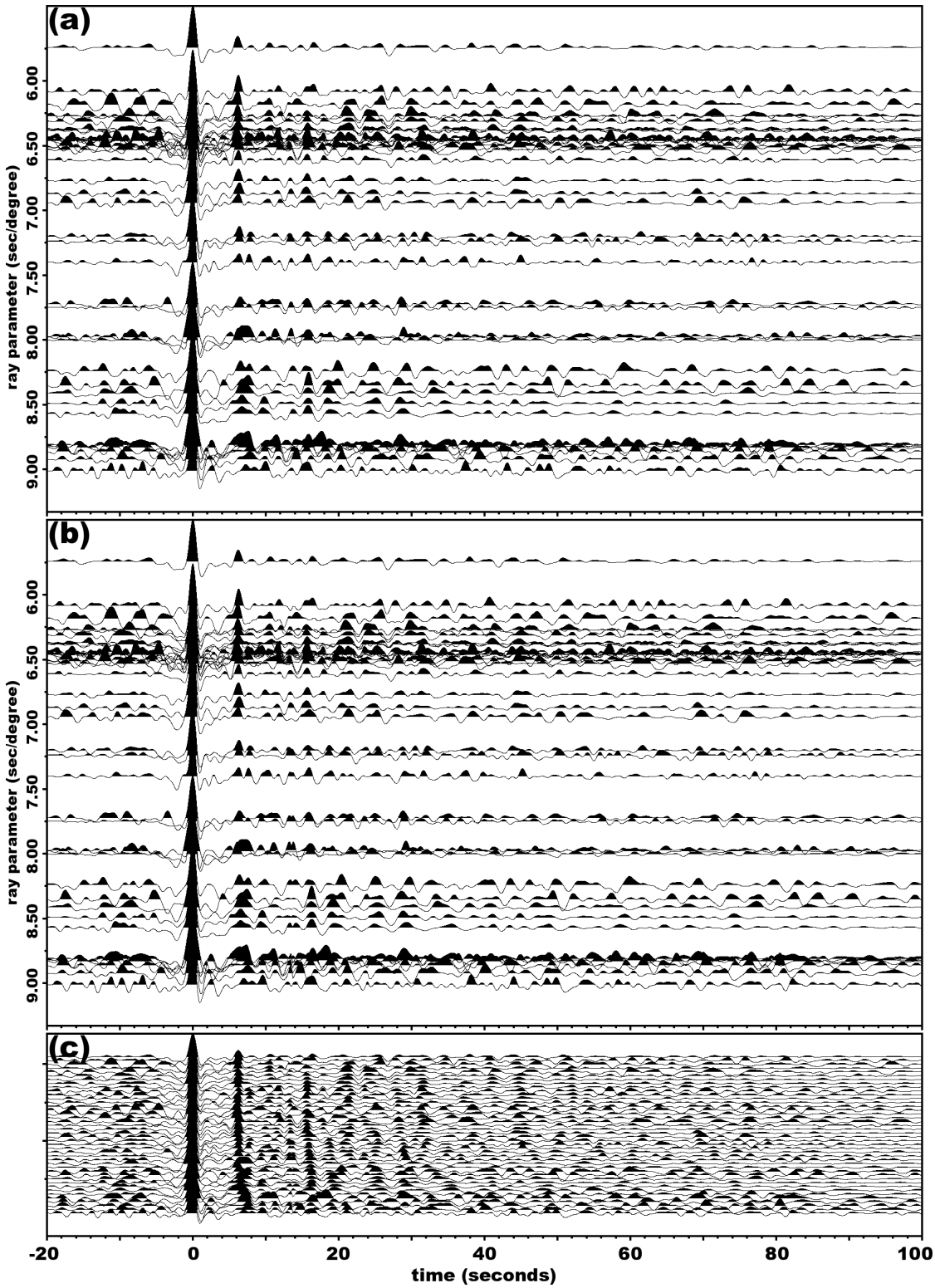

Figure 5: Example of receiver function gathers from the SA azimuth for station MYNC. Alpha = 2.0. (a) Gathers plotted by ray parameter (b) Gathers plotted by ray parameter and moveout corrected; plot preserves relative p spacing between traces (c) Same as (b), but plotted with equal spacing. Parameters for moveout correction are V_P=6.5, V_S=3.7, H=52, and V_P/V_S=1.756 with a reference ray parameter of 0.06 s/km.

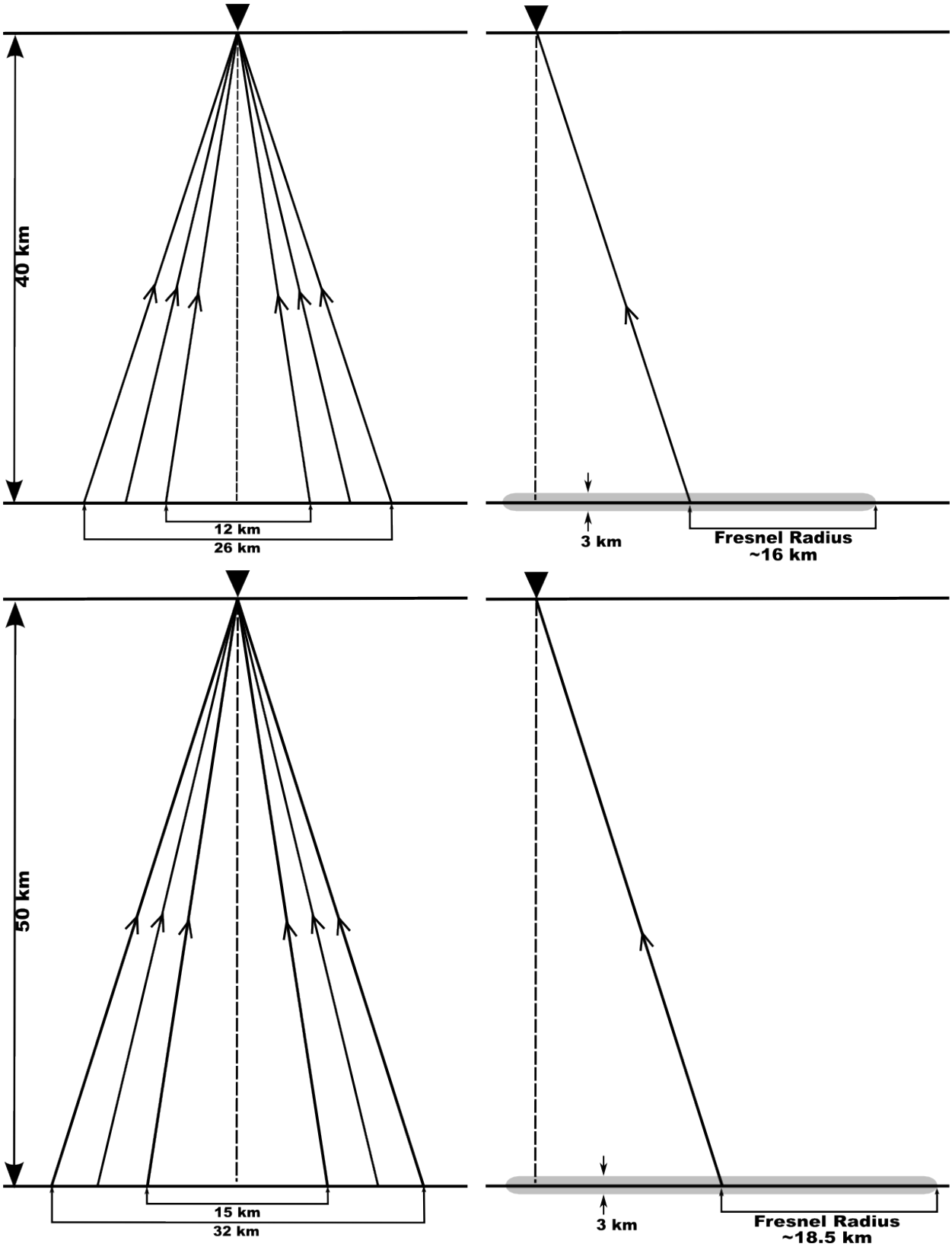

Figure 6: Ray path diagram showing the horizontal extent and resolution of P_S conversions.

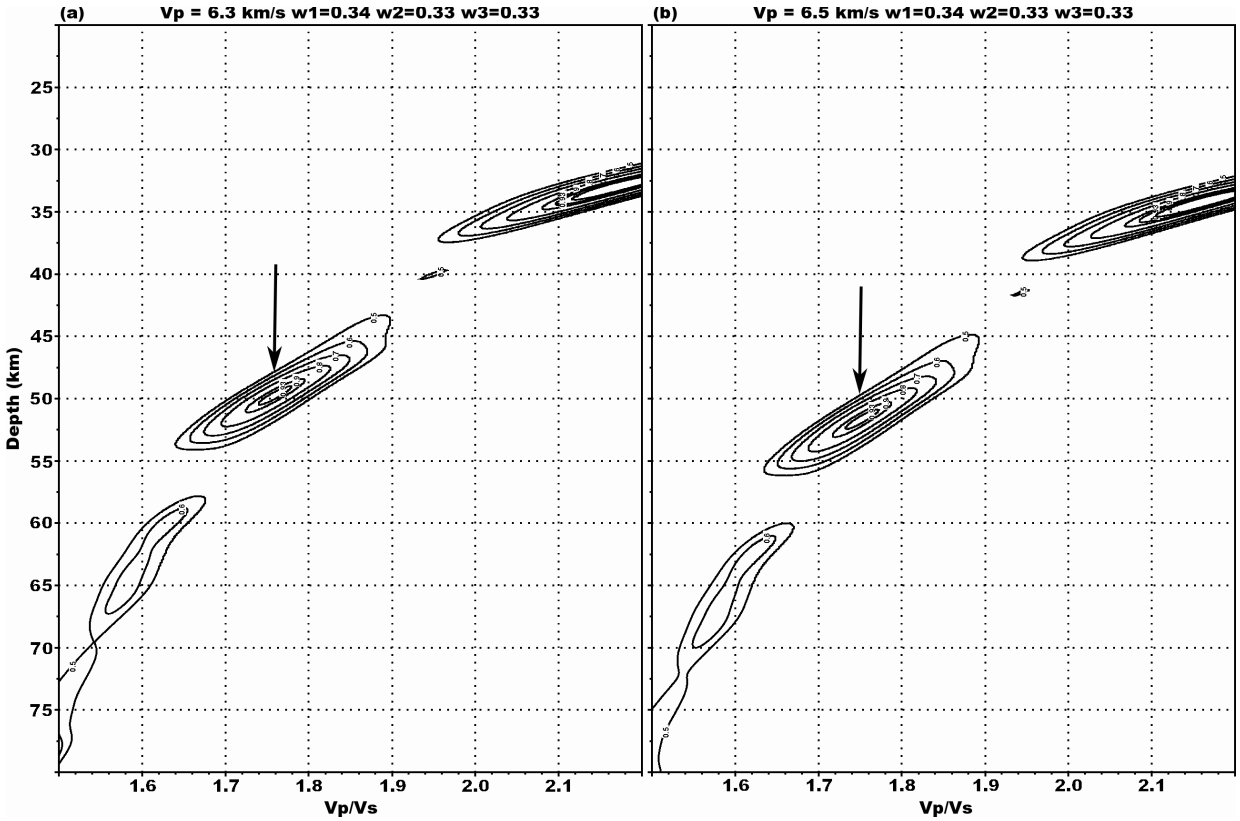

Figure 7: Example of $H - \kappa$ stacks of receiver functions for a range of V_P. Receiver functions are from the SA azimuth for station MYNC and Figure 5 shows the gather used to generate the stacks. (a) V_P = 6.3 km/s (b) V_P = 6.5 km/s. The arrows mark the resulting peaks and correspond to (a) H=49.74 km and V_P/V_S=1.760 and (b) H=51.65 km and V_P/V_S=1.752. Weightings for different phases are indicated at the top of each plot; w1 = P_S weight, w2 = P_PP_S weight, w3 = P_SP_S+ P_PS_S weight.

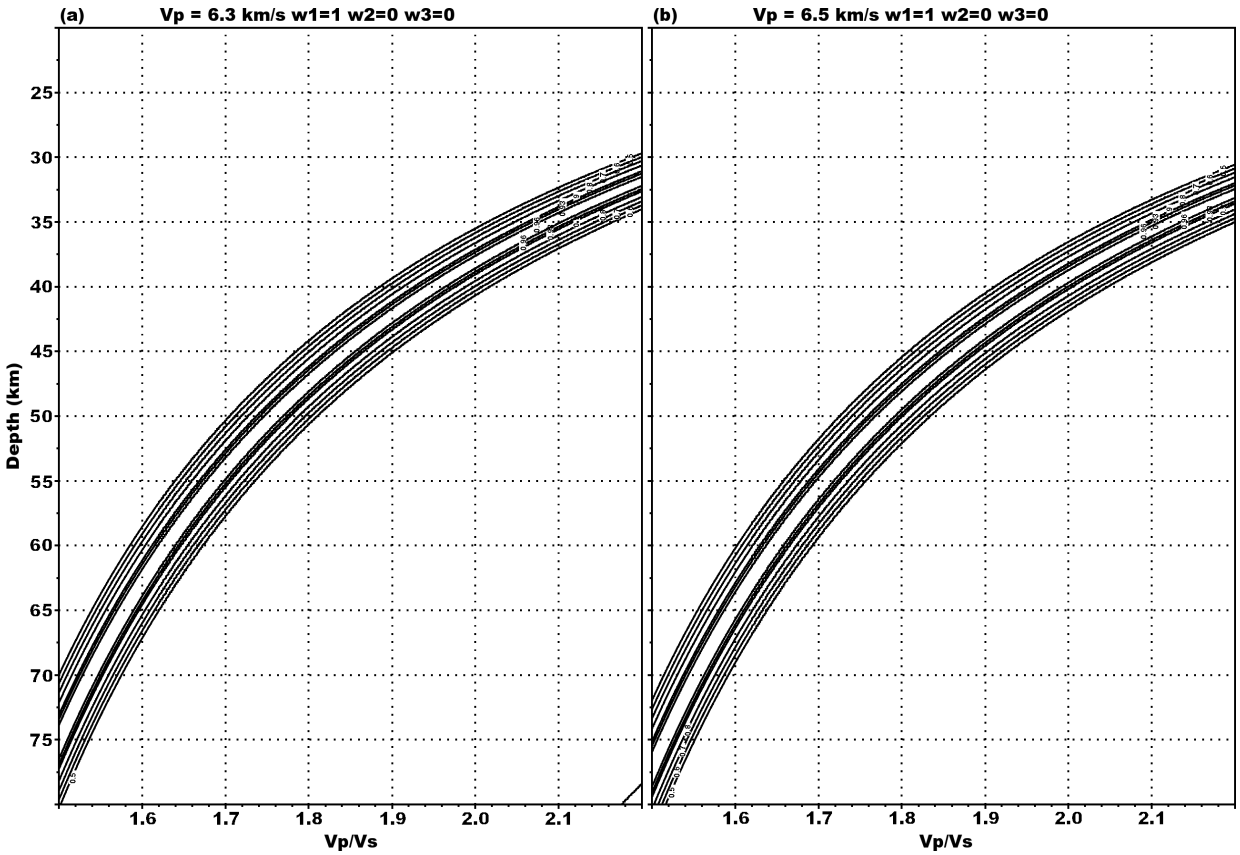

Figure 8: Example of H – κ stacks of receiver functions using the P_S arrival only. Receiver functions are from the SA azimuth for station MYNC and Figure 5 shows the gather used to generate the stacks. (a) V_P = 6.3 km/s (b) V_P = 6.5 km/s.

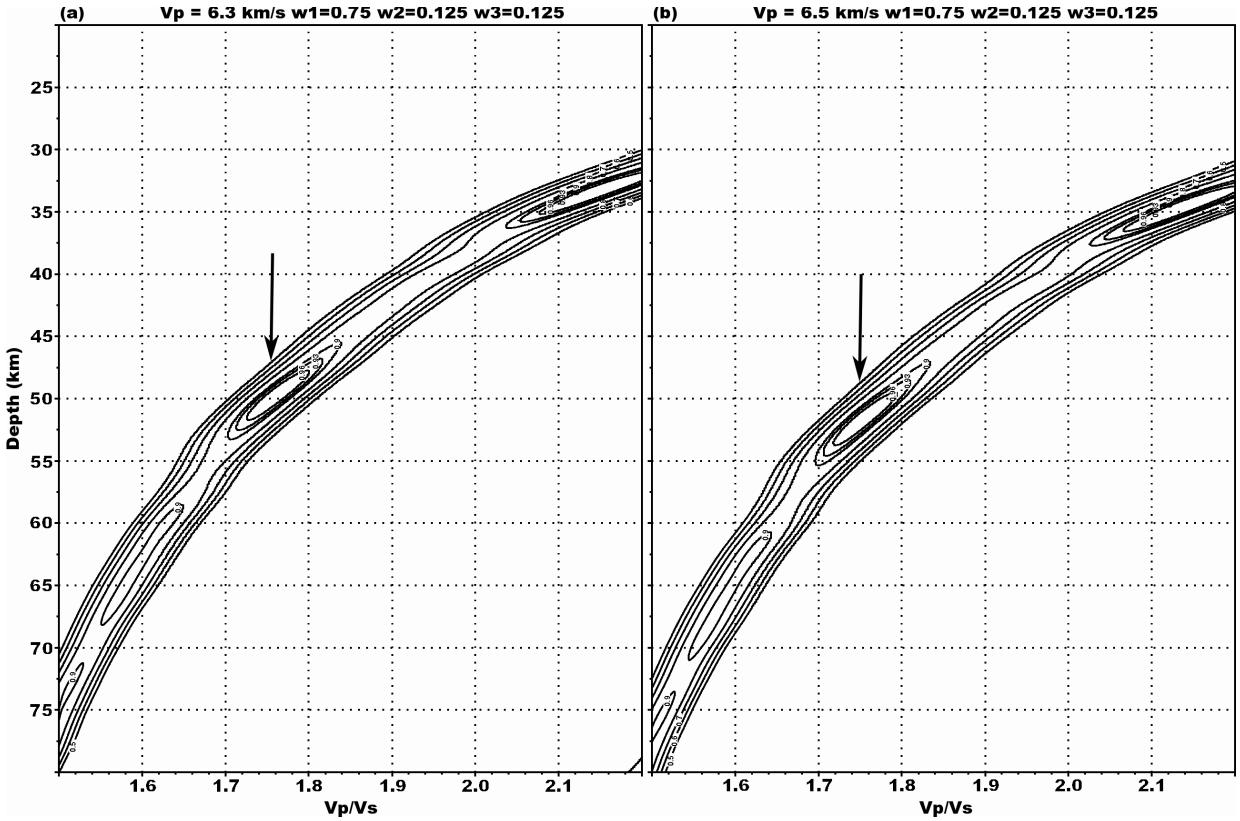

Figure 9: Example of H – κ stacks of receiver functions with different weighting of phases. Receiver functions are from the SA azimuth for station MYNC and Figure 5 shows the gather used to generate the stacks. (a) V_P = 6.3 km/s (b) V_P = 6.5 km/s. The arrows mark the resulting peaks. Weightings for different phases are indicated at the top of each plot; w1 = P_S weight, w2 = P_PP_S weight, w3 = P_SP_S+ P_PS_S weight.

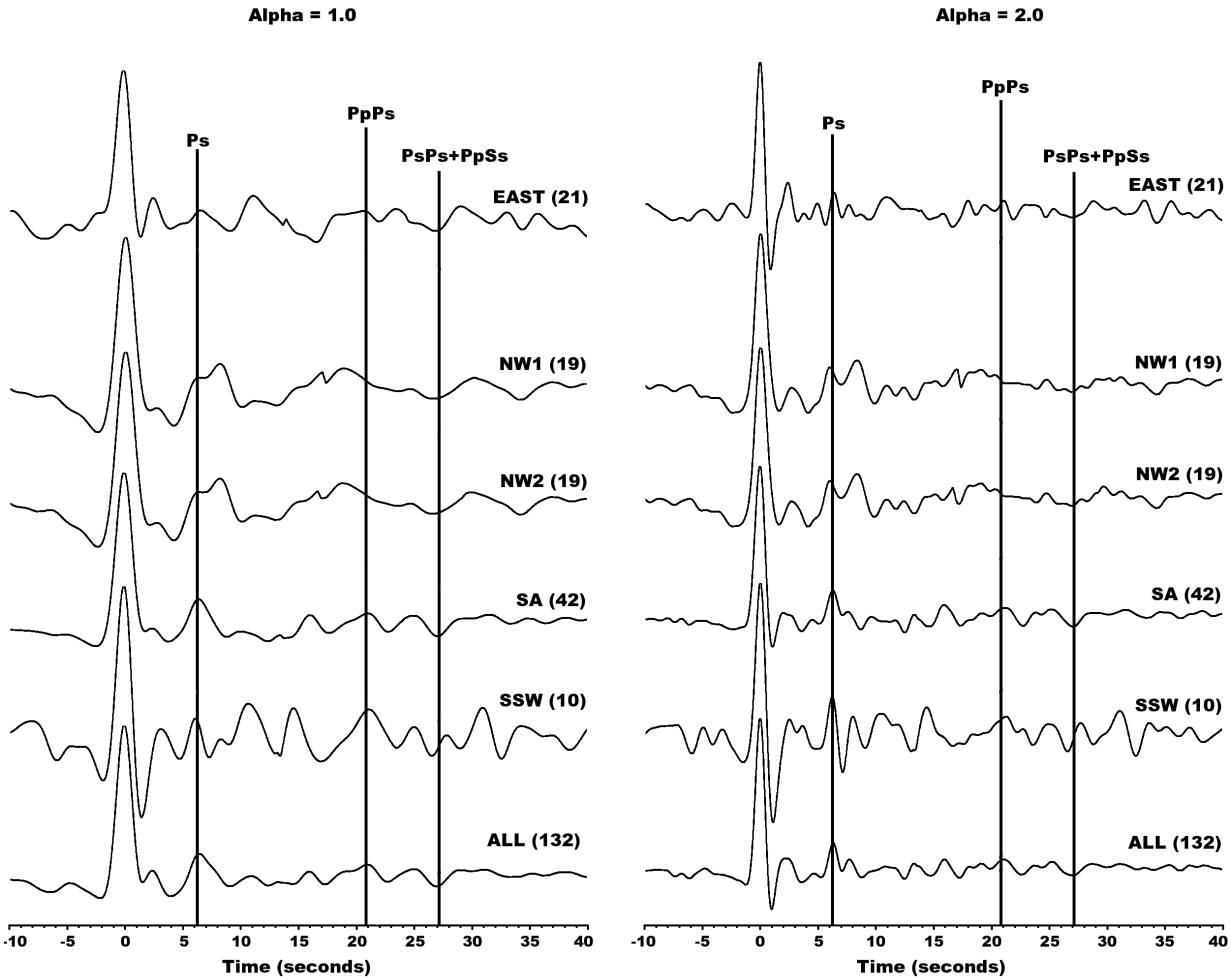

Figure 10: Stacked receiver functions for MYNC for H=50 km. Two different Gaussian (Alpha) settings are shown. Azimuth and number of receiver functions in stack are to the right of each trace. NW1 and NW2 correspond to the first and second set of values in the Table 2 respectively. The selection of parameter values used for the moveout correction were based on the values in Table 2. A reference ray parameter of 0.06 s/km was used for the moveout correction. Vertical lines are predicted arrival times computed for H=50, V_P=6.3, V_S=3.6, and V_P/V_S=1.750 using equations (8)–(10).

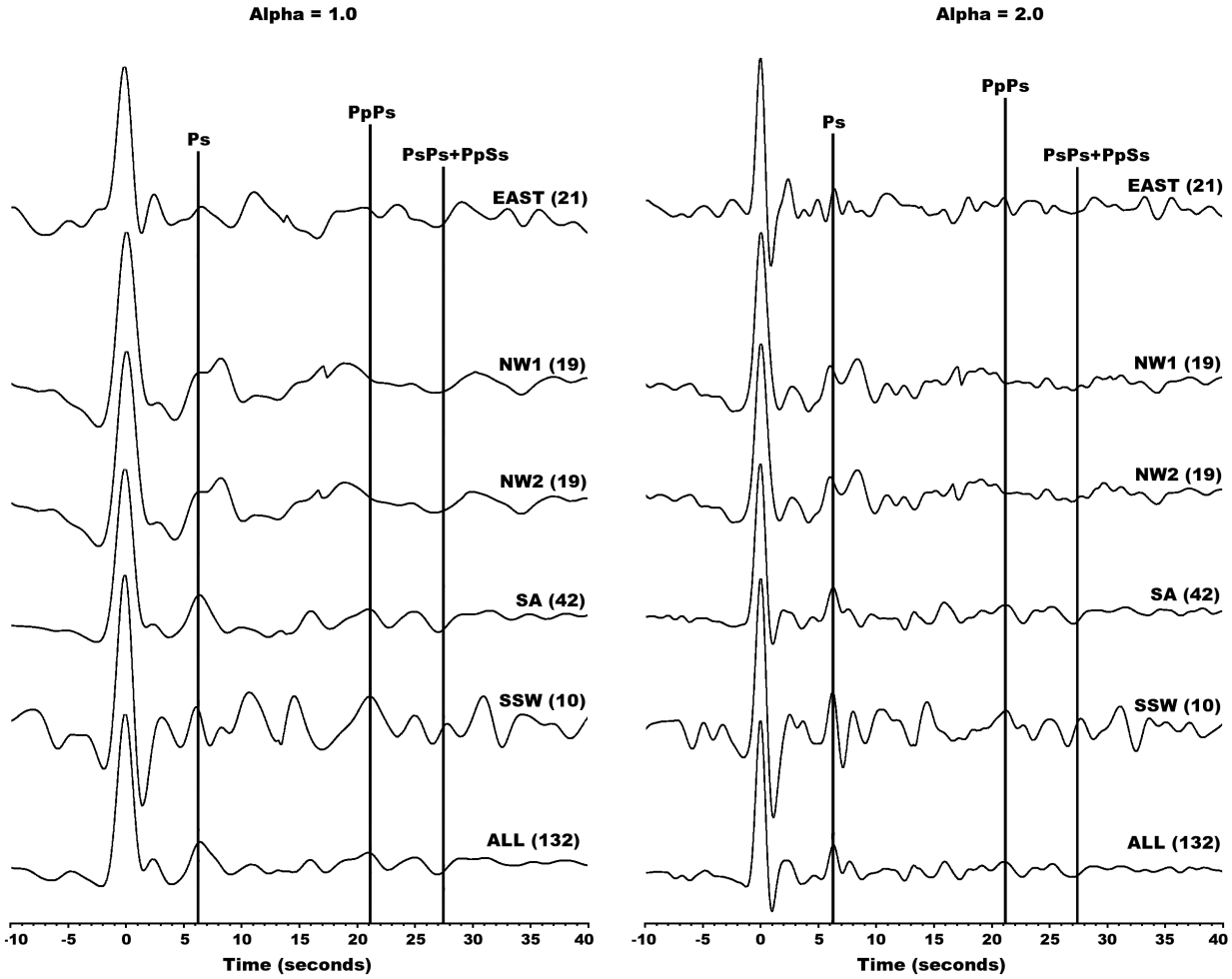

Figure 11: Stacked receiver functions for MYNC for H=52 km. Two different Gaussian (Alpha) settings are shown. Azimuth and number of receiver functions in stack are to the right of each trace. NW1 and NW2 correspond to the first and second set of values in the Table 2 respectively. The selection of parameter values used for the moveout correction were based on the values in Table 2. A reference ray parameter of 0.06 s/km was used for the moveout correction. Vertical lines are predicted arrival times computed for H=52, V_P=6.5, V_S=3.7, and V_P/V_S=1.756 using equations (8)–(10).

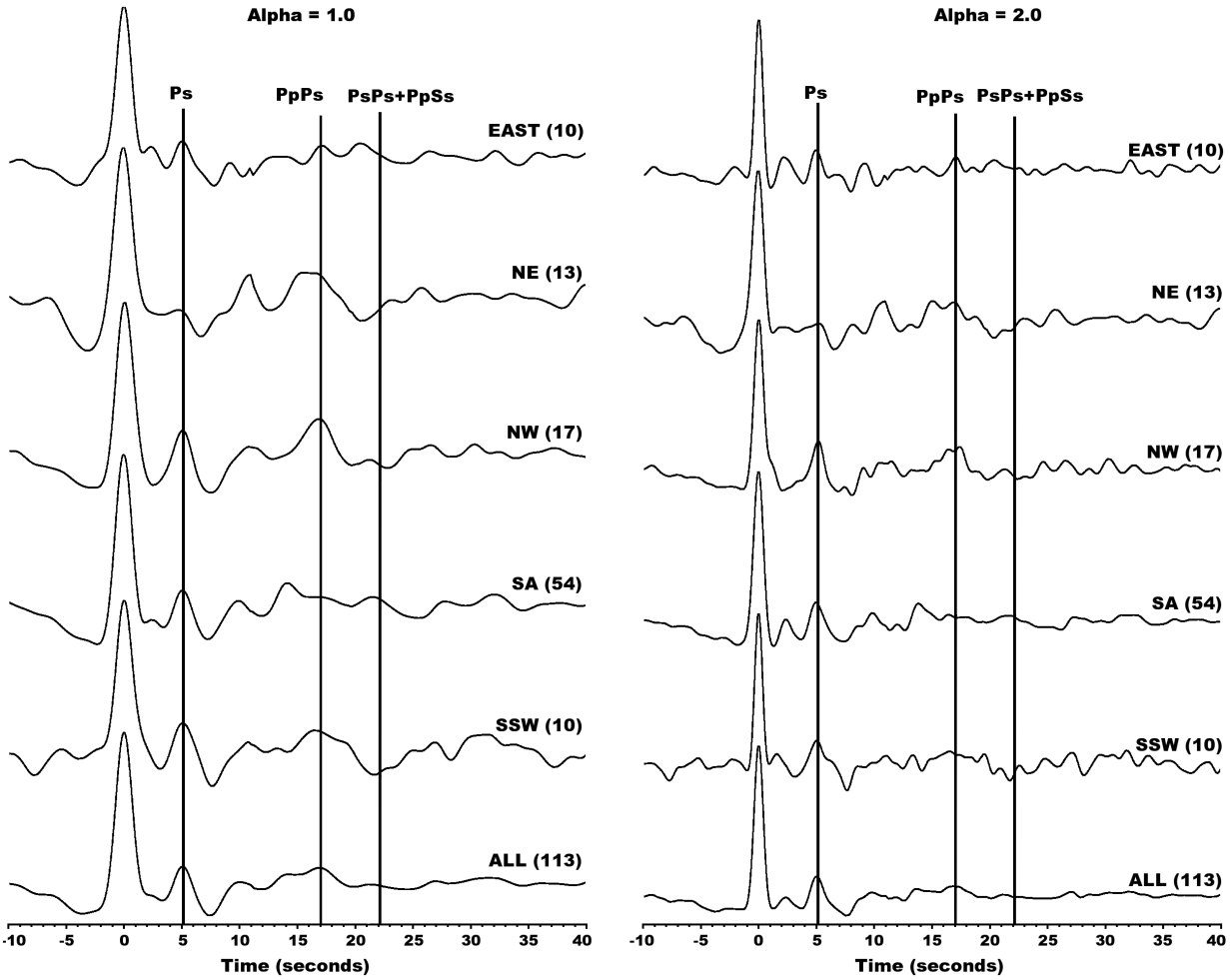

Figure 12: Stacked receiver functions for GOGA for H=42 km. Two different Gaussian (Alpha) settings are shown. Azimuth and number of receiver functions in stack are to the right of each trace. The selection of parameter values used for the moveout correction were based on the values in Table 1. A reference ray parameter of 0.06 s/km was used for the moveout correction. Vertical lines are predicted arrival times computed for H=42, V_P=6.5, V_S=3.7, and V_P/V_S=1.756 using equations (8)–(10).

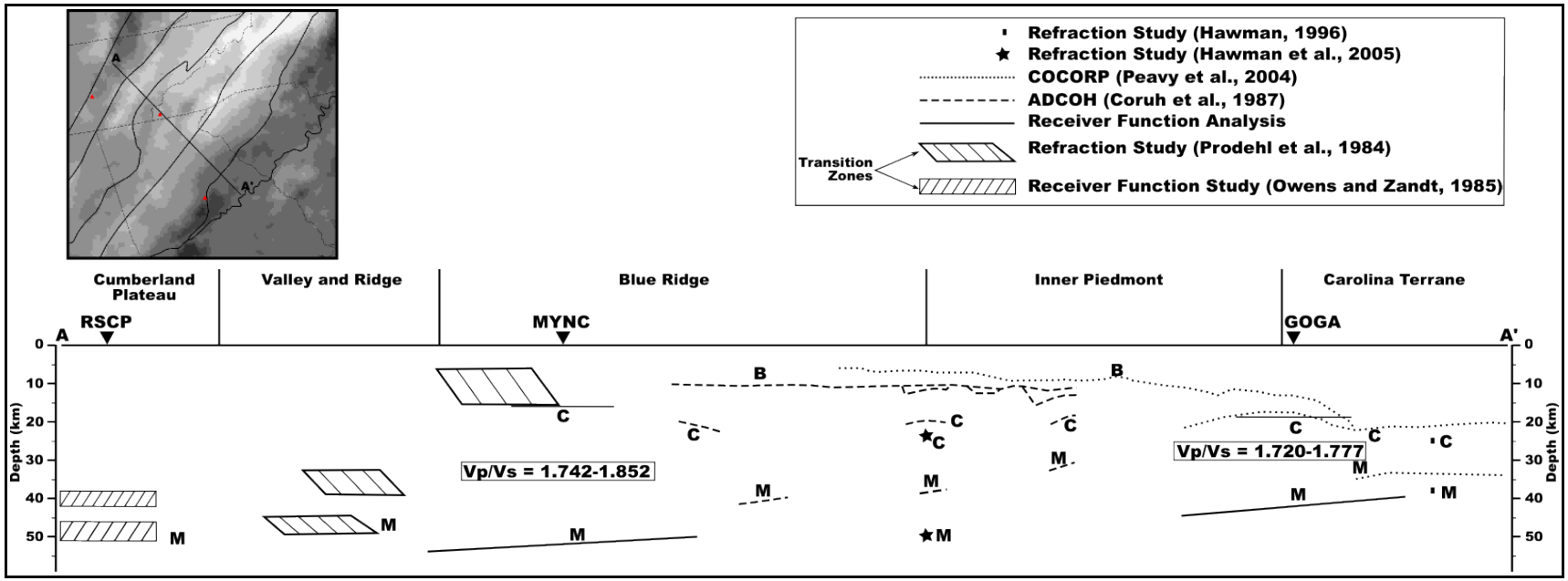

Figure 13: Generalized cross-section of the southern Appalachians. The cross-section is plotted at 1:1 (horizontal scale is equal to vertical scale). "B" is the top of basement, "C" is the mid-crustal discontinuity, and "M" is the Moho.

Chapter 5

Discussion

Crustal thickness variations: Carolina Terrane to Cumberland Plateau

Based on the receiver function analysis, the crustal thickness around station MYNC is considerably greater than the crustal thickness around station GOGA. The results of this research are consistent with the estimates for previous refraction studies in both areas, but the crustal thicknesses are slightly greater on average.

Estimates of crustal thickness from the receiver function analysis for station GOGA range from 40 to 44 km (Table 1), compared with 37–39 km for the most recent refraction/wide–angle reflection experiments in the Carolina Terrane (Hawman, 1996). The smaller values (30–33 km) inferred from two–way times (11–12 s) for events interpreted as Moho reflections on COCORP profiles 1 and 5 (Cook et al., 1979) were computed assuming an average crustal P–wave velocity of 6.0 km/s. Average crustal velocities constrained by strong reflections from the lower crust and Moho (Hawman, 1996) are significantly higher (6.5–6.6 km/s), indicating that earlier crustal thickness estimates are too small. Estimates of crustal thickness from the receiver function analysis for station MYNC range from 48–55 km (Table 2). Thicknesses reported from refraction profiles in the Blue Ridge, Valley and Ridge, and eastern Cumberland Plateau range from 49 to 55 km (Prodehl et al., 1984). A clustering of migrated reflections at depths between 40 and 50 km has also been observed in wide–angle soundings in the Valley and Ridge portions of the Eastern Tennessee Seismic Zone, roughly 50 km west of MYNC (Hawman et al., 2001). Preliminary migration of wide–angle reflections shows a crustal thickness of about 50 km along the southeast flank of the Blue Ridge Mountains in South Carolina (Hawman et al., 2005).

The deepest reflections observed in the ADCOH profiles dip steadily northwest from a minimum of 11 s TWT beneath the Inner Piedmont to a maximum of 15 s at the northwest end of ADCOH line 3. Corresponding Moho depths depend on the value assumed for the average velocity of the crust. As noted in Chapter 2, a value of 6.0 km/s (Hubbard et al., 1991) corresponds to a thickness between 33 and 45 km, while values of 6.4–6.5 km/s (closer to the global average for continental crust; Christensen and Mooney, 1995) yield thicknesses between 35 and 49 km. Further analysis of wide–angle reflection data from the Blue Ridge (Hawman et al., 2005) should help to constrain these values.

A comparison of Moho reflection travel times predicted from the crustal models derived from refraction and receiver function analysis with observed times for events interpreted as Moho reflections in COCORP and ADCOH profiles yields interesting comparisons. Normal–incidence Moho reflection travel times predicted from the most recent refraction models for the Carolina Terrane (Hawman, 1996) are 11.4–11.9 s; Moho reflection times predicted for the models derived for GOGA are slightly greater (12.8–13.1 s). Both sets of predicted times are greater than the times observed on the COCORP sections (11–11.5 s). Moho reflection travel times predicted for the models derived for MYNC range from 15.2 to 16.1 s, which again is greater than the range (14–15 s) observed in the reflection (ADCOH) profiles. These results are consistent with the different sampling depths expected for the different ranges in wavelength for the arrivals used in the three types of surveys (Braile and Chiang, 1986).

Receiver function analysis for other parts of the Appalachians

The refraction results from Prodehl et al. (1984) and receiver function results of Zandt and Owens (1986) for the Cumberland Plateau and the Valley and Ridge are similar. Langston and Isaac (1981) estimated crustal thicknesses much greater than previously proposed from refraction work (41 km opposed to 33 km) in central Pennsylvania using receiver function

analysis. Velocity gradients within the crust were not obtained nor were intermediate layers recognized. Owens and Zandt (1985) modeled the Moho as a transition zone with a thickness of 4–5 km using receiver function analysis and data from the broadband stations in the Cumberland Plateau in eastern Tennessee (RSCP) and the Adirondacks in New York (RSNY). They obtained a crustal thickness of 49–51 km for the Cumberland Plateau and 50–51 km for the Adirondacks (Owens and Zandt, 1985; Zandt and Owens, 1986).

Station GOGA is close to the East Coast Gravity high and the Appalachian gravity gradient. The gradient has been interpreted as marking the southeastern boundary of Grenville basement but other interpretations are possible (Hutchinson et al., 1983; Hawman, 1996). Near station GOGA in the Carolina Terrane, Hawman (1996) estimated crustal thicknesses between 37 and 39 km with an average V_P of 6.5–6.6 km/s. That work also reported a midcrustal discontinuity at a depth of 24–26 km which is also apparent in the COCORP and ADCOH profiles. Using the estimates from Hawman (1996) for the reference compressional wave velocities, the thicknesses and V_P/V_S ratios from the $H - \kappa$ stacking of GOGA data in this study are close to the thicknesses and V_P/V_S ratio found by Hawman (1996).

As noted above, the overall trend in crustal thicknesses for the southern Appalachians from previous results and this study shows a thickening of the crust from the SE to the NW, providing evidence for the crustal root hypothesis (Hawman, 1996; Hawman *et al.*, 2005). There is an approximately 10 km difference in crustal thickness between MYNC and GOGA. This is close to the expected difference between the Blue Ridge and Inner Piedmont for isostatically compensated topography. Gravity modeling by Hawman (1996) shows that the variations in crustal thicknesses adequately account for the long–wavelength gravity anomalies that exist along some of the profiles but not along others. Hawman (1996) suggests that the mismatches could be accounted for by compositional differences in the lower crust involving a transition

from a more granitic average composition in the Inner Piedmont to a more intermediate average composition in the Carolina Terrane.

Crustal composition

The average crustal V_P/V_S ratio of 1.75 for station MYNC is consistent with rocks of granitic to intermediate composition (Christensen and Mooney, 1995; Christensen, 1996). The lateral variation around the station is readily seen when comparing the other azimuths with the NW. The NW azimuth is consistent with a more mafic composition than the other azimuths. A second explanation for the increase in V_P/V_S would be the presence of limestone. Limestone has a higher V_P/V_S than sandstone (Christensen and Szymanski, 1991), and if the sedimentary rocks underlying the crystalline thrust sheet are predominately limestone, then this could explain the increase in V_P/V_S to the NW.

The V_P/V_S ratio for station GOGA is about 1.74 and again is consistent with rocks of granitic to intermediate composition. This is similar to the average composition inferred for the crust underneath MYNC, but the V_P/V_S ratio is slightly less. One possible mechanism for decreasing the V_P/V_S ratio for a package of rock is increasing the silica content. For the crust underneath GOGA, this could be due to a large volume of rock with high quartz content somewhere within the crust which would have the effect of lowering the V_P/V_S ratio slightly, but not enough to characterize the average composition of the entire crust as quartz–rich (Hawman, 1996). If the underlying sedimentary rocks in the Inner Piedmont and Carolina Terrane were predominately sandstones rather than limestone, this could explain the slight decrease in V_P/V_S for crust beneath GOGA.

Anomalous results

The NW azimuth of MYNC shows a distinct double peak in both the $H - \kappa$ stacks and simple stacks. The thickness of the crust is considerably greater than the other azimuths around

MYNC with one peak indicating a crustal thickness of approximately 55 km and the other peak a thickness of 60 km. The double peak may be related to a thick transition zone or more simply two separate interfaces. More modeling is required to determine the exact nature of the crust for this azimuth. Migration of raypaths to determine the exact locations of conversions would allow a mapping of Moho depth variations around each station. Compared with other azimuths, the phase coherence of major arrivals is fairly poor (Appendix B); the addition of more receiver functions for deep earthquakes along this azimuth might help to clarify the gathers and the stacks.

The $H - \kappa$ stacks from the SA azimuth for station GOGA show quite different crustal structure than all of the other azimuths around GOGA. The thickness is considerably less (~32 km) than the ~42 km of the other azimuths. An explanation for this is interference with the multiples. The $H - \kappa$ stack with just the P_S arrival shows the same trend as the other stations, but when the multiples are incorporated in the stacking, the peak shows unrealistically high V_P/V_S ratios and much shallower depths to Moho. The predicted arrival time for the first multiple (P_PP_S) is approximately 17 s for acceptable values of H, V_P, V_S, and V_P/V_S for GOGA, and on the gathers from MYNC (where the predicted P_PP_S is about 21 s) there is a prominent arrival around 16–17 s that is likely a conversion from the upper mantle. If the same arrival is present in the SA gather for GOGA, then it may be interfering with multiples to generate the smeared out branch around 16 to 17 s.

The higher V_P/V_S ratio of ~1.80 for the NW azimuth for station MYNC can be related to increased fluid pore pressure or compositional variation (*e.g.* decrease in silica content). An increase in fluid–filled fractures would decrease V_S by a greater amount than V_P, thereby increasing the V_P/V_S ratio. Composition on the other hand can explain the increase in V_P/V_S as well. Minerals such as amphibole, plagioclase, pyroxene, and Fe-olivine have a V_P/V_S ratio

greater than 1.80. An increase in Ca increases the V_P/V_S ratio, as does Fe substitution for Mg in olivine and pyroxene (Christensen, 1996; Musacchio *et al.*, 1997). If this is the case, then the crust in the NW could be compositionally different (more mafic) than the crust sampled along other azimuths.

The interpretation of V_P/V_S in terms of composition is further complicated by the effects of metamorphism. V_P and V_P/V_S can vary with metamorphic grade, without a change in bulk chemical composition (Christensen, 1996). Examples include the increase in V_P and decrease in V_P/V_S as clay minerals are replaced by micas in pelitic rocks. Mafic rocks show a more complicated variation in V_P/V_S as the mineral assemblages change (Christensen, 1996). In general, V_P for mafic rocks steadily increases with metamorphic grade, while V_P/V_S first decreases (as metamorphic grade increases through the greenschist and amphibolite facies), then increases (with the transition to granulite facies) and finally decreases again with the transition to eclogite facies, as plagioclase is replaced by garnet. Tighter constraints on the V_P structure of the crust beneath the Blue Ridge from wide-angle seismic data would help to narrow the range of possible interpretations of the receiver-function results.

Chapter 6

Conclusions

Receiver function analysis provides a means of estimating the thickness and composition of the crust in the area surrounding a broadband seismic station. It is possible to analyze the data so that lateral variations around the station can be investigated by grouping events into azimuths. Beneath station MYNC, the thickness of the crust is approximately 52 km with a decrease in thickness from the NW to SE, and the V_P/V_S ratios are approximately 1.75, which suggests an intermediate average composition for the crust. For station GOGA, the crustal thickness is approximately 42 km with a decrease in thickness from the NW to the SE. The V_P/V_S ratio for GOGA is slightly lower (approximately 1.74) than MYNC, but still consistent with an intermediate average composition, perhaps with a quartz–rich layer (overthrust sediments?) somewhere within the crust. The estimates for crustal thickness and V_P/V_S are consistent with previous refraction and reflection studies, but on average the crustal thicknesses are slightly greater. Variations around station MYNC are intriguing and further investigation of the NW azimuth is recommended.

REFERENCES

Ammon, C. J., The isolation of receiver functions from teleseismic P waveforms, *Bulletin of the Seismological Society of America*, 81, 2504–2510, 1991.

Braile, L. W. and C. S. Chiang, The continental Mohorovicic discontinuity: Results from near–vertical and wide–angle seismic reflection studies, in *Reflection Seismology: A Global Perspective*, edited by Muawia Barazangi and Larry Brown, American Geophysical Union, Washington, D. C., 257-272, 1986.

Cook, F. A., D. S. Albaugh, L. D. Brown, S. Kaufman, J. E. Oliver, and R. D. Hatcher, Jr., Thin–skinned tectonic in the crystalline southern Appalachians; COCORP seismic-reflection profiling of the Blue Ridge and Piedmont, *Geology*, 7, 563–567, 1979.

Coruh, C., J. K. Costain, R. D. Hatcher, Jr., T. L. Pratt, R. T. Williams, and R. A. Phinney, Results from regional vibroseis profiling: Appalachian ultra-deep core hole site study, *Geophys. J. R. astr. Soc.*, 89, 147–156, 1987.

Christensen, N. I. and W. D. Mooney, Seismic velocity structure and composition of the continental crust: A global view, *Journal of Geophysical Research*, 100, p 9761–9788, 1995.

Christensen, N. I., Poisson's ratio and crustal seismology, *Journal of Geophysical Research*,101, 3139–3156, 1996.

Christensen, N. L. and D. L. Szymanski, Seismic properties and the origin of reflectivity from a classic Paleozoic sedimentary sequence, Valley and Ridge province, southern Appalachians, *Geol Soc. Am. Bull.*, 103, 277–289, 1991.

Dorman, L. M., Seismic crustal anisotropy in norther Georgia, *Bulletin of the Seismological Society of America*, 62, 39–45, 1972.

Edelman, S. H., A. Liu, and R. D. Hatcher, Jr., The Brevard Zone in South Carolina and adjacent areas: An Alleghanian orogen–scale dextral shear zone reactivated as a thrust fault, *J. Geology*, 95, 793–806, 1987.

Griffin, V. S., The Inner Piedmont belt of the southern crystalline Appalachians, *Geol Soc. Am. Bull.*, 82, 1885-1898, 1971

Hatcher, R. D., Jr., Interpretation of seismic reflection data in complexly deformed terranes: A geologist's prespective, in *Reflection Seismology: The Continental Crust*, edited by Muawia Barazangi and Larry Brown, American Geophysical Union, Washington, D. C., 9–12, 1986.

Hatcher, R. D., Jr., Appalachians introduction, in *The Appalachian–Ouachita Orogen in the United States*, edited by Hatcher, R. D., Jr., W. A. Thomas, and G. W. Viele, Boulder, CO, The Geological Society of America, The Geology of North America, v. F-2, 233–318, 1989.

Hatcher, R.D., Jr. and A.L. Odom, Timing of thrusting in the southern Appalachians, USA: model for orogeny?, *Journal of the Geological Society London,* 137, 321–327, 1980.

Hatcher, R. D., Jr., J. K. Costain, C. Coruh, R. A. Phinney, and R. T. Williams, Tectonic implications of new Appalachian Ultradeep Core Hole (ADCOH) seismic reflection data from the crystalline southern Appalachians, *Geophys. J. R. astr. Soc.*,89, 157–162, 1987.

Hatcher, R. D., Jr., W. A. Thomas, P. A. Geiser, A. W. Snoke, S. Mosher, D. V. Wiltschko, Alleghanian orogen, in *The Appalachian–Ouachita Orogen in the United States*, edited by Hatcher, R. D., Jr., W. A. Thomas, and G. W. Viele, Boulder, CO, The Geological Society of America, The Geology of North America, v. F-2, 233–318, 1989.

Hawman, R.B., Wide–angle, three–component seismic reflection profiling of the crust beneath the East Coast Gravity High, southern Appalachians, using quarry blasts, *Journal of Geophysical Research*, 101, 13933–13945, 1996.

Hawman, R.B., M.C. Chapman, C.A. Powell, J.E. Clippard, and H.O. Ahmed, Wide-angle reflection profiling with quarry blasts in the Eastern Tennessee seismic zone, *Seismological Research Letters*, 72, 108-–122, 2001.

Hawman, R. B., Using delay–fired quarry blasts to image the crust: A comparison of methods for deconvolving mixed–delay source wavelets, *Bulletin of the Seismological Society of America*, 94, 1476–1491, 2004.

Hawman, R.B., M.O. Khalifa, J.A. Kucinskis, and J.E. Clippard, Seismic profiling with quarry blasts in the Blue Ridge Mountains, North Carolina: An alternative procedure for migrating wide-angle reflection data (abstract), *Seismological Research Letters,* 76, 122, 2005.

Hopson, J. L., R. D. Hatcher, Jr. and A. L. Stieve, Geology of the eastern Blue Ridge, northeastern Georgia and the adjacent Carolinas, *Georgia Geological Society Field Trip Guidebook*, 9, 1–39, 1989.

Hubbard, S. S., C. Coruh, and J. K. Costain, Paleozoic and Grenvillian structures in the southern Appalachians: Extended interpretation of seismic reflection data, *Tectonics*, 10, 141–170, 1991.

Hutchinson, D. R., J. A. Grow, and K. D. Klitgord, Crustal structure beneath the southern Appalachians: Nonuniqueness of gravity modeling, *Geology*, 11, 611–615, 1983.

Iverson, W. P. and S. B. Smithson, Reprocessing and reinterpretation of COCORP southern Appalachian profiles, *Earth and Planetary Science Letters*, 62, 75–90, 1983.

Kean, A. E. and L. T. Long, A seismic refraction line along the axis of the southern Piedmont and crustal thicknesses in the southern United States, *Earthquake Notes*, 51, 3–13, 1980.

Keller, G. R. and R. D. Hatcher, Jr., Some comparisons of the structure and evolution of the southern Appalachian–Ouachita orogen and portions of the Trans–European Suture Zone region, *Tectonophysics,* 314, 43–68, 1999.

Kennett, B. L. N. and E. R. Engdahl, Traveltimes for global earthquake location and phase identification, *Geophys. J. Int.*, 105, 429–465, 1991.

Langston, C. A., Structure under Mount Rainier, Washington, inferred from teleseismic body waves, *Journal of Geophysical Research*, 84, 4749–4762, 1979.

Langston, C. A. and C. M. Isaacs, A crustal thickness constraint for central Pennsylvania, *Earthquake Notes*, 52, 13–22, 1981.

Musacchio, G., W. D. Mooney, J. H. Luetgert, and N. I. Christensen, Composition of the crust in the Grenville and Appalachian Provinces of North America inferred from V_P/V_S ratios, *Journal of Geophysical Research*, 102, 15225–15241, 1997.

Nelson, K. D., J. H. McBride, J. A. Arnow, D. M. Wille, L. D. Brown, J. E. Oliver, and S. Kaufman, Results for recent COCORP profiling in the southeastern United States, *Geophys. J. R. astr. Soc.*, 89, 141–146, 1987.

Owens, T. J. and G. Zandt, The response of the continental crust-mantle boundary observed on broadband teleseismic receiver functions, *Geophysical Research Letters*, 12, 705–708, 1985.

Peavey, Samuel T., Cahit Coruh, John K. Costain and William J. Domoracki, Contrasts in tectonic style of the Central and Southern Appalachians, United States: Insights from seismic reflection data, *Journal of Geodynamics*, 37, 633–655, 2004.

Phillips, J. D., J. S. Duval, and R. A. Ambroziak, U. S. Geological Survery Digital Data Series DDS–9: National Geophysical Data Grids: Gamma–Ray, Gravity, Magnetic, and Topographic Data for the Conterminous United States [CD–ROM], *USGS Map Distribution*, Denver, CO, 1993.

Prodehl, C., J. Schlittenhardt, and S. W. Stewart, Crustal structure of the Appalachian highlands in Tennessee, *Tectonophysics*, 109, 61–76, 1984.

Rogers, John, *The Tectonics of the Appalachians*, Wiley-Interscience, New York, 1970.

Secor, D. T., A. W. Snoke, K. W. Bramlett, O. P. Costello, and O. P. Kimbrell, Character of the Alleghanian orogeny in the southern Appalachians, I, Alleghanian deformation in the eastern Piedmont of South Carolina, *Geol Soc. Am. Bull.*, 97, 1319–1328, 1986.

Settles, D. J., R. D. Hatcher, Jr., and B. R. Bream, The Hayesville-Soque River and Allatoona faults and an Ordovician arc assemblage in the central Blue Ridge northwest of Dahlonega, Georgia, *Georgia Geological Society Guidebooks,* 22, 17–42, 2002.

Sheriff, R. E. and L. P. Geldart, *Exploration Seismology Volume 1: History, theory, & data acquisition*, Cambridge University Press, Cambridge, 1982.

Thomas, W. A., Genetic relationship of rift-stage crustal structure, terrane accretion, and foreland tectonics along southern Appalachian–Ouachita orogen, *Journal of Geodynamics*, 37, 549–563, 2004.

Valentino, D. W. and A. E. Gates, Asynchronous extensional collapse of a transpressional orogen: the Alleghanian central Appalachian Piedmont, USA, *Journal of Geodynamics*, 31, 145–167, 2001.

Zandt, G., S. C. Myers, and T. C. Wallace, Crust and mantle structure across the Basin and Range – Colorado Plateau boundary at 37º N latitude and implications for Cenozoic extensional mechanism, *Journal of Geophysical Research*, 100, 10529–10548, 1995.

Zandt, G. and T. J. Owens, Comparison of crustal velocity profiles determined by seismic refraction and teleseismic methods, *Tectonophysics*, 128, 155–161, 1986.

Zhu, L., and H. Kanamori, Moho depth variations in southern California from teleseismic receiver functions, *Journal of Geophysical Research*, 105, 2969–2980, 2000.

Appendix A
Events used in the analysis

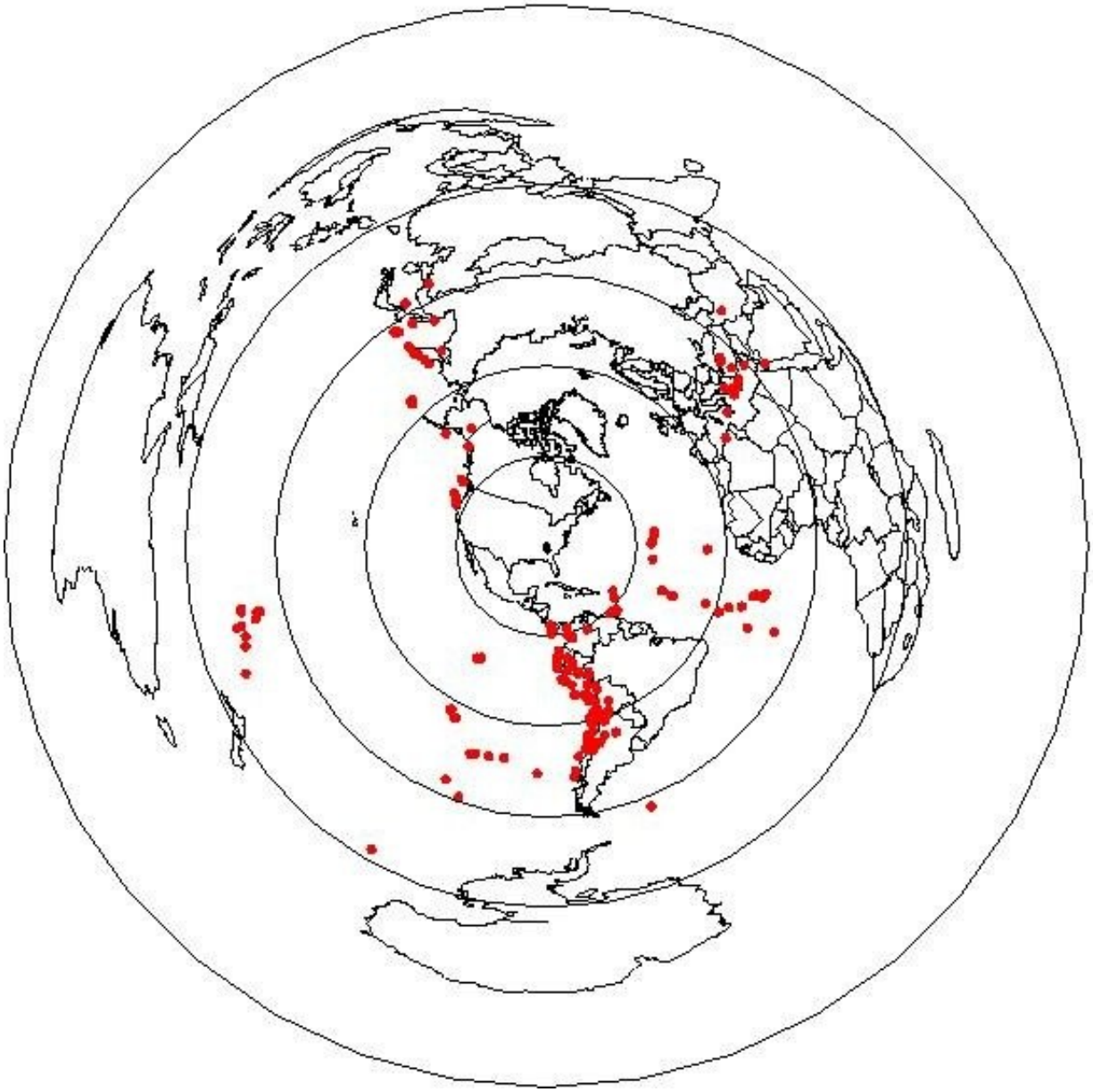

Figure A1: Azimuthal view of the world showing the location of events used in the analysis. The circles show distance away from the station in degrees (30, 60, 90, and 120).

Table A1: Events for station MYNC. The ray parameters were calculated using the IASP91 model. The pdif ray parameters are a consequence of diffracted rays at the core–mantle interface.

Date (Julian)	Time (UTC h:m:s)	Latitude (deg)	Longitude (deg)	Depth (km)	Distance (deg)	Back Azimuth (deg)	Ray Parameter (sec/deg)
1993, 122	02:09:26.06	-17.3201	-14.5036	10	84.06	115.8	5.09
1993, 131	16:24:59.23	-24.9158	-70.4545	42.7	61.06	165.8	6.79

Date (Julian)	Time (UTC h:m:s)	Latitude (deg)	Longitude (deg)	Depth (km)	Distance (deg)	Back Azimuth (deg)	Ray Parameter (sec/deg)
1993, 186	00:52:41.00	-24.92	-112.42	10	65.41	208.25	6.48
1993, 187	02:53:04.00	-24.56	-111.89	10	64.88	207.93	6.52
1993, 192	13:36:22.21	-25.2319	-70.0546	0.0	61.44	165.47	6.77
1993, 193	13:17:11.00	42.89	139.23	7.6	92.89	329.65	4.60
1993, 197	21:21:26.51	-33.1833	-72.0103	31.7	68.84	169.12	6.23
1993, 198	01:35:39.23	-29.9781	-71.5564	47.3	65.78	168.05	6.44
1993, 203	04:57:05.33	6.4898	-71.1759	7.9	30.85	154.26	8.81
1993, 215	12:43:05.74	28.7800	34.5700	10	78.45	49.97	5.52
1993, 215	16:33:20.60	28.7600	34.7000	12.6	94.12	50.51	4.57
1993, 238	10:03:58.07	36.7700	28.0500	35.6	84.7	48.31	5.03
1993, 254	06:14:28.73	-4.6513	-76.3159	128.2	40.19	167.88	8.24
1993, 257	17:20:42.39	-29.41	-177.19	24.4	108.52	246.77	4.44(pdif)
1993, 263	10:17:42.16	0.7573	-29.3451	10	61.28	111.34	6.78
1993, 303	17:59:03.05	-31.6729	-68.2407	108.9	68.05	165.42	6.26
1993, 317	12:30:50.49	-16.3552	-70.7585	86.7	52.7	163.8	7.38
1993, 318	01:59:18.75	-22.6513	-68.5999	102.8	59.27	163.28	6.90
1993, 323	09:05:39.53	7.3489	-34.7220	10	52.98	109.38	7.38
1993, 329	20:24:01.01	-0.9085	-13.3120	10	74.9	102.01	5.79
1995, 033	12:53:53.41	10.7621	-42.5715	10	44.83	112.38	7.97
1995, 043	01:02:05.09	-5.7715	-76.1246	7.7	41.32	167.88	8.21
1995, 045	15:53:56.70	-23.3383	-67.6907	0.0	60.15	162.54	6.87
1995, 260	07:25:27.83	-35.5416	-74.1575	11.9	70.86	171.41	6.08
1995, 262	03:31:53.77	-21.2034	-68.6719	0.0	57.86	162.92	7.03
1995, 276	01:51:28.24	-2.7332	-77.8971	59.7	38.06	169.88	8.41
1995, 276	16:08:15.36	-30.6416	-71.8816	17.8	66.37	168.49	6.41
1995, 305	00:35:32.61	-28.8840	-71.3778	19.9	64.74	167.63	6.53
1995, 326	04:15:11.94	28.8300	34.8000	10	94.27	50.33	4.57
1995, 337	18:01:10.15	44.53	149.31	0	87.11	324.89	4.85
1995, 363	14:36:53.54	14.3481	-59.9631	57.5	29.98	127.44	8.83
1996, 019	19:02:00.70	-10.3736	-78.7390	52.5	45.48	172.56	7.91
1996, 047	09:44:58.58	-1.4733	-15.3018	10.6	73.65	103.71	5.88
1996, 050	02:28:31.85	-1.1968	-14.2161	10	74.35	102.81	5.83
1996, 050	07:10:07.00	-42.0380	-75.2682	7.6	77.17	173.24	5.62
1996, 052	12:51:01.73	-9.6915	-79.7670	10.0	44.71	173.89	7.98
1996, 053	13:40:56.52	-33.5313	-71.4372	66.4	69.27	168.69	6.18
1996, 189	10:49:59.59	58.59	157.7	10	73.47	331.21	5.89
1996, 198	03:48:28.85	56.05	165	0	71.97	326.54	6.01
1996, 202	00:00:41.57	36.1300	27.0500	26.8	84.5	49.32	5.05
1996, 206	20:21:34.16	41.82	-125.88	10	33.13	294.41	8.71
1996, 218	02:08:57.83	-15.36	-173.08	0	97.82	256.81	4.46
1996, 218	21:39:15.08	-1.9698	-81.0284	23.4	36.96	174.84	8.49

Date (Julian)	Time (UTC h:m:s)	Latitude (deg)	Longitude (deg)	Depth (km)	Distance (deg)	Back Azimuth (deg)	Ray Parameter (sec/deg)
1996, 218	22:38:20.57	-20.72	-178.29	531.2	104.89	255.03	4.44(pdif)
1996, 231	07:16:10.86	0.6545	-30.0144	10	60.85	111.92	6.81
1996, 233	17:19:56.87	5.3760	-82.6121	10.0	29.58	176.94	8.86
1996, 249	08:14:19.40	-22.18	-113.41	50.7	63.36	210.48	6.62
1996, 252	08:08:12.90	-15.5712	-73.0302	93.3	51.46	166.28	7.46
1996, 253	00:20:41.00	-31.8814	-71.4423	53.8	67.66	168.35	6.31
1996, 255	06:28:46.22	4.2011	-76.5894	116.9	31.5	165.5	8.76
1996, 283	14:19:37.83	34.5200	32.1300	19	88.65	47.8	4.71
1996, 309	17:24:57.66	7.3801	-77.4045	10.0	28.25	165.79	8.92
1996, 318	00:28:20.09	-15.0694	-75.6728	33.0	50.51	169.39	7.56
1996, 318	02:47:33.17	-15.3497	-75.4844	33.0	50.81	169.21	7.53
1996, 344	11:28:53.52	29.8576	-42.8256	46.6	35.05	86.71	8.60
1996, 353	10:12:27.74	-25.1604	-70.6996	0.0	61.24	166.11	6.79
1997, 082	20:48:48.82	30.9354	-41.5201	10	35.77	84.33	8.57
1997, 084	16:44:34.02	-9.0511	-71.2480	619.2	45.54	162.04	7.57
1997, 091	18:42:07.66	-18.2172	-69.2485	55.6	54.85	162.63	7.23
1997, 092	06:14:33.63	11.4664	-61.1936	73.4	31.41	132.85	8.78
1997, 112	09:31:28.85	11.1620	-61.0914	47.1	31.71	133.06	8.77
1997, 129	18:40:59.63	35.3700	27.3300	11.7	85.16	49.76	5.00
1997, 131	22:16:15.53	-36.12	-97.68	10	71.95	191.51	6.00
1997, 145	18:57:30.83	-22.9834	-70.5901	44.6	59.15	165.45	6.93
1997, 149	17:02:38.90	-35.94	-102.5	10	72.7	195.54	5.95
1997, 176	19:38:44.29	33.9400	59.4500	35	103.34	30.48	4.44(pdif)
1997, 177	19:21:08.54	-49.76	-114.65	10	88.69	199.24	4.70
1997, 181	18:56:28.28	-4.1332	-80.9210	37.8	39.11	174.92	8.35
1997, 187	09:54:00.18	-30.0470	-71.8104	14.0	65.81	168.3	6.45
1997, 187	23:15:18.43	-30.1253	-71.8875	16.9	65.87	168.39	6.45
1997, 190	19:24:10.25	10.5045	-63.5453	3.0	30.82	137.56	8.82
1997, 190	19:28:35.78	10.6	-63.49	19.9	30.77	137.37	8.81
1997, 191	14:55:50.00	-23.0492	-71.0914	0.0	59.11	165.99	6.94
1997, 197	10:53:10.38	28.4751	-43.6906	10	34.82	89.42	8.62
1997, 200	12:22:54.14	-29.2001	-71.5917	4.2	65.02	167.91	6.51
1997, 203	19:10:35.42	4.6461	-32.6936	10	56.24	110.37	7.15
1997, 208	10:07:52.55	35.5800	21.0600	33	81.01	52.79	5.32
1997, 227	07:37:49.15	-4.4	-105.73	10	44.21	211.77	8.01
1997, 227	22:53:31.48	-5.8549	-81.0203	31.5	40.81	175.27	8.24
1997, 230	12:24:26.55	-29.8984	-71.9639	33.0	65.64	168.41	6.46
1997, 238	08:43:27.46	-6.9879	-21.9489	10	71.89	112.53	6.01
1997, 307	19:17:34.96	-30.7624	-71.1646	54.6	66.61	167.85	6.38
1997, 307	20:12:53.87	-30.8257	-71.2421	63.1	66.67	167.94	6.37
1997, 314	12:47:34.21	0.0790	-16.8716	10	71.47	103.42	6.04

Date (Julian)	Time (UTC h:m:s)	Latitude (deg)	Longitude (deg)	Depth (km)	Distance (deg)	Back Azimuth (deg)	Ray Parameter (sec/deg)
1997, 322	13:07:38.33	37.4800	20.6900	10	79.65	51.43	5.43
1997, 322	13:13:48.68	37.4800	20.9100	46.2	79.79	51.32	5.41
1997, 332	22:53:42.61	-13.7720	-68.7982	599.8	50.71	160.62	7.24
1997, 339	11:26:53.81	54.8	162.01	25.2	74.08	326.59	5.84
1997, 345	07:56:29.66	3.9729	-75.7653	182.4	31.9	164.07	8.71
1997, 347	19:22:58.96	-41.3880	-87.3941	10.0	76.15	182.53	5.69
1998, 010	04:54:25.55	-12.0264	-72.0638	33.0	48.22	164.08	7.72
1998, 012	04:12:02.61	-24.9123	-70.0210	22.9	61.14	165.36	6.79
1998, 012	10:14:09.65	-31.0218	-71.3387	53.1	66.84	168.07	6.37
1998, 030	12:16:09.30	-23.8380	-70.1614	0.0	60.07	165.23	6.87
1998, 084	21:02:52.42	-24.2160	-66.8876	164.7	61.19	162.01	6.73
1998, 088	07:15:00.20	-0.0504	-17.9662	10	70.67	104.23	6.10
1998, 088	20:38:37.98	-17.65	-178.96	493	103.78	258.04	4.44(pdif)
1998, 091	22:42:59.08	-40.2828	-74.9150	19.0	75.46	172.73	5.74
1998, 093	22:01:51.92	-8.0835	-74.9182	170.1	43.79	166.76	7.97
1998, 100	16:40:39.57	-1.2150	-15.6506	10	73.22	103.73	5.91
1998, 102	23:49:34.82	-15.6617	-71.8814	33.0	51.78	164.92	7.46
1998, 142	04:48:50.46	-17.8595	-65.5390	24.0	55.52	158.39	7.20
1998, 148	18:33:28.41	31.4500	27.6400	10	87.88	52.58	4.75
1998, 152	05:34:04.18	52.88	160.02	48.6	76.22	325.83	5.68
1998, 158	16:10:45.33	-31.4700	-67.7863	103.0	67.95	164.97	6.27
1998, 169	04:17:55.60	-11.4768	-14.0731	10	80.73	110.99	5.35
1998, 174	10:58:42.09	23.7975	-45.0773	10	35.61	97.68	8.58
1998, 176	21:03:44.83	17.7433	-61.5691	42.1	26.47	124.9	9.02 / 10.0
1998, 178	13:55:53.47	36.8500	35.3200	46.6	88.96	44.32	4.69
1998, 190	14:19:18.40	38.7200	48.5100	26	94.5	35.29	4.56
1998, 210	07:14:24.99	-32.2719	-71.2180	56.0	68.08	168.23	6.27
1998, 216	17:35:06.58	-0.4797	-80.3443	41.3	35.55	173.48	8.57
1998, 216	18:59:22.34	-0.5539	-80.3153	46.6	35.62	173.45	8.57
1998, 246	17:37:56.29	-29.3682	-71.6196	12.0	65.17	167.98	6.50
1998, 274	03:41:13.34	13.7502	-45.5600	10	40.69	111.68	8.25
1998, 281	04:51:40.41	-16.0485	-71.3472	111.6	52.27	164.4	7.40
1998, 332	09:58:12.38	-7.5993	-74.4317	171.7	43.42	165.94	8.00
1998, 344	08:21:12.77	-7.9219	-71.3250	624.4	44.44	161.72	7.64
1998, 345	08:37:49.20	-31.1302	-68.8681	102.8	67.4	165.85	6.31
1998, 347	17:31:59.12	13.3491	-44.8295	10	41.49	111.49	8.20
1999, 025	18:19:18.18	4.4690	-75.6820	24.3	31.44	163.69	8.79
1999, 048	21:58:54.34	-21.1950	-70.0520	33.0	57.54	164.39	7.05
1999, 061	17:45:54.89	-22.8020	-68.4910	110.2	59.44	163.21	6.88
1999, 064	00:33:41.94	-20.3370	-68.8370	62.7	56.99	162.84	7.08
1999, 090	05:54:45.02	6.1090	-82.7050	10.0	28.85	177.06	8.89

Date (Julian)	Time (UTC h:m:s)	Latitude (deg)	Longitude (deg)	Depth (km)	Distance (deg)	Back Azimuth (deg)	Ray Parameter (sec/deg)
1999, 127	14:19:52.62	56.5	-152.86	40.8	50.13	317.68	7.58
1999, 183	11:49:52.49	49.33	-129.15	10	35.71	307.56	8.57
1999, 188	19:02:29.01	49.2	155.55	41.3	80.78	325	5.33
1999, 189	15:38:02.47	-18.08	-178.62	628.8	103.74	257.49	4.44(pdif)
1999, 213	12:55:19.74	51.56	-176.27	45.1	64.67	316.36	6.53
1999, 218	00:42:06.21	49.93	156.23	54.9	79.96	325.22	5.39
1999, 351	04:09:25.00	8.08	-38.03	10	49.98	111.31	7.60
1999, 67	12:25:46.77	52.07	159.44	36.6	77.02	325.44	5.62
1999, 79	10:47:45.09	51.56	-177.72	25.8	65.49	316.79	6.47
2002, 091	19:59:32.69	-29.6339	-71.2699	72.7	65.49	167.71	6.46
2002, 108	16:08:36.00	-27.3400	-69.9900	60.9	63.5	165.95	6.61
2002, 111	22:24:05.99	-5.7859	-81.0399	22.9	40.75	175.29	8.25
2002, 114	10:51:50.93	42.4400	21.4700	10	84.55	49.83	45.05
2002, 131	10:43:09.14	-10.4289	-78.5369	56.1	45.56	172.29	7.90
2002, 143	15:52:16.63	-30.7219	-71.1929	62.8	66.57	167.87	6.38
2002, 148	04:04:22.00	-28.8900	-66.5700	21.3	65.74	163.13	6.46
2002, 168	13:25:57.51	-4.5	-105.29	10	44.11	211.14	8.02
2002, 169	13:56:22.00	-30.7800	-70.9300	52.2	66.67	167.64	6.38
2002, 173	02:58:21.00	35.6700	48.9300	10	97.12	36.84	4.48
2002, 174	11:10:43.70	-30.8609	-71.1519	79.8	66.71	167.86	6.37
2002, 179	17:19:30.61	43.76	130.67	568	95.38	335.47	4.47
2002, 215	02:39:04.67	8.2410	-82.9159	26.8	26.73	177.34	9.01/9.99
2002, 215	14:18:13.96	-1.4619	-14.4629	10	74.41	103.16	5.82
2002, 220	13:39:55.86	5.0620	-77.7739	19.9	30.44	167.42	8.83
2002, 231	11:01:02.33	-21.7	-179.46	587.7	106.33	254.77	4.44(pdif)
2002, 249	01:21:27.00	38.37	13.72	10	74.6	53.87	5.81
2002, 267	03:57:22.00	-31.4100	-68.9400	117.3	43.72	165.97	8.00
2002, 285	20:09:11.00	-8.2600	-71.5300	535.9	43.79	165.93	7.75
2002, 292	12:19:24.81	44.16	149.87	33	87.13	324.34	4.84
2002, 307	22:18:21.42	63.44	-145.63	10.8	46.61	327.07	7.84
2002, 321	04:53:55.04	47.7708	145.9942	483.9	86.13	328.67	4.74
2003, 007	00:54:52.00	-33.5900	-69.7600	110.7	69.62	167.23	6.14
2003, 16	00:57.52.73	44.31	-129.09	10	35.43	298.93	8.59
2004, 320	09:06:56.00	4.6300	-77.5400	15.0	30.9	167.13	8.81

Table A2: Events for station GOGA. The ray parameters were calculated using the IASP91 model. The pdif ray parameters are a consequence of diffracted rays at the core–mantle interface.

Date (Julian)	Time (UTC h:m:s)	Latitude (deg)	Longitude (deg)	Depth (km)	Distance (deg)	Back Azimuth (deg)	Ray Parameter (sec/deg)
1993, 108	09:16:22.08	-11.66	-76.52	95.3	45.31	170.41	7.90
1993, 126	13:03:20.27	-8.5	-71.46	600.6	43.22	162.54	7.74
1993, 136	21:44:48.85	-15.2876	-173.2934	21.3	98.11	257.11	4.45
1993, 145	23:51:26.43	-23.32	-66.59	221	58.66	161.79	6.89
1993, 149	06:50:13.69	19.0996	-26.4806	12	52.47	90.75	7.42
1993, 186	00:52:41.00	-24.92	-112.42	10	64.22	209.22	6.57
1993, 187	02:53:04.00	-24.56	-111.89	10	63.69	208.92	6.61
1993, 192	13:36:22.21	-25.23	-70.05	0	59.7	165.91	6.90
1993, 198	01:35:39.23	-29.98	-71.56	47.3	64.05	168.52	6.57
1995, 122	06:06:07.96	-3.78	-76.93	116.9	37.5	169.25	8.42
1995, 133	08:47:13.06	40.17	21.69	13.9	79.36	48.81	5.68
1995, 147	13:03:52.26	52.6	142.85	7.7	85.3	333.73	4.99
1995, 166	00:15:48.73	38.4	22.28	14.2	80.75	50.01	5.34
1995, 266	22:31:53.87	-10.71	-78.58	39.1	44.12	173.09	8.01
1995, 274	15:57:16.20	38.06	30.13	33	85.86	46.49	4.95
1995, 276	12:45:01.01	-2.78	-77.86	37.8	36.38	170.53	8.49
1995, 280	21:28:08.89	-2.79	-77.85	57	36.39	170.52	8.51
1995, 285	23:41:45.60	-35.37	-106.25	8.4	71.67	199.47	6.03
1995, 305	00:35:32.61	-28.88	-71.38	19.9	63.01	168.09	6.65
1995, 326	04:15:11.94	28.83	34.8	10	94.9	50.83	4.55
1995, 336	17:13:22.99	44.29	149.21	58	89.02	325.17	4.69
1995, 337	18:01:10.15	44.53	149.31	0	88.79	325.27	4.70
1996, 038	21:36:45.60	45.26	149.89	0	87.97	325.46	4.74
1996, 047	09:44:58.58	-1.4733	-15.3018	10.6	72.72	103.63	5.95
1996, 050	02:28:31.85	-1.1968	-14.2161	10	73.41	102.83	5.90
1996, 052	12:51:01.73	-9.69	-79.77	10	43.01	174.65	8.10
1996, 053	13:40:56.52	-33.53	-71.44	66.4	67.54	169.14	6.31
1996, 070	08:56:22.22	-13.05	-69.44	0	48.1	161.5	7.74
1996, 107	00:44:43.63	-24.25	-177	0	105.72	251.16	4.44 (Pdif)
1996, 110	00:19:31.20	-23.96	-70.02	0	58.47	165.55	6.99
1996, 154	02:52:09.62	10.7942	-42.2725	10	43.92	111.09	8.03
1996, 160	23:19:13.77	51.42	-178.12	23.4	67.37	317.45	6.34
1996, 162	04:03:35.71	51.55	-177.61	34.1	67.02	317.43	6.36
1996, 162	15:24:57.18	51.4	-176.85	33	66.65	317.07	6.39
1996, 164	02:16:48.30	51.38	-178.21	31.4	67.43	317.44	6.33
1996, 173	13:57:11.99	51.55	159.08	33	79.2	325.66	5.46
1996, 202	00:00:41.57	36.13	27.05	26.8	85.16	49.55	5.00
1996, 218	02:19:55.26	-15.36	-173.08	0	97.98	256.94	4.45

Date (Julian)	Time (UTC h:m:s)	Latitude (deg)	Longitude (deg)	Depth (km)	Distance (deg)	Back Azimuth (deg)	Ray Parameter (sec/deg)
1996, 218	22:38:20.57	-20.7195	-178.2906	531.2	104.99	254.94	4.44 (Pdif)
1996, 232	04:19:15.83	51.44	-178.35	29.2	67.49	317.54	6.33
1996, 233	17:19:56.87	5.38	-82.61	10	27.9	178.18	8.94/9.79
1996, 249	09:46:59.59	-22.02	-113.11	10	62.22	211.53	6.71
1996, 253	00:20:41.00	-31.88	-71.44	53.8	65.93	168.8	6.43
1996, 268	11:42:19.14	15.2026	-61.4507	148.1	26.94	126.99	8.93
1996, 280	20:13:09.57	49.01	-127.89	10	36.31	308.89	8.54
1996, 296	22:15:02.95	63.46	-145.47	11.4	48.24	327.87	7.73
1996, 309	17:24:57.66	7.38	-77.4	10	26.51	166.42	9.03/10.0
1996, 344	11:28:53.52	29.8576	-42.8256	46.6	34.62	84.64	8.62
1997, 092	06:14:33.63	11.4664	-61.1936	73.4	29.88	131.77	8.83
1997, 112	09:31:28.85	11.1620	-61.0914	47.1	30.18	132.01	8.83
1997, 139	02:25:51.35	6.69	-82.4	10	26.61	177.63	9.03/10.0
1997, 145	18:57:30.83	-22.98	-70.59	44.6	57.4	165.89	7.05
1997, 149	17:02:38.90	-35.94	-102.5	10	71.25	196.23	6.06
1997, 161	21:53:55.56	-35.75	-108.1	10	72.62	200.96	5.96
1997, 177	19:21:08.54	-49.76	-114.65	10	87.31	199.64	4.82
1997, 181	18:56:28.28	-4.13	-80.92	37.8	37.41	175.82	8.46
1997, 187	09:54:00.18	-30.05	-71.81	14	64.07	168.77	6.58
1997, 190	19:29:32.98	10.6	-63.49	19.9	29.19	136.47	8.87
1997, 201	10:14:19.67	-22.85	-66.22	221.7	58.3	161.25	6.92
1997, 227	07:37:49.15	-4.4	-105.73	10	43.11	213.56	8.09
1997, 245	12:13:23.08	3.88	-75.7	196.4	30.26	164.48	8.78
1997, 287	09:53:11.07	-22.1447	-176.7203	105.4	104.44	252.91	4.44 (Pdif)
1997, 288	01:03:33.03	-30.89	-71.14	54.1	65.01	168.32	6.50
1997, 301	06:15:19.22	-4.35	-76.68	127.5	38.1	168.99	8.38
1997, 307	19:17:34.96	-30.76	-71.16	54.6	64.88	168.31	6.51
1997, 322	13:07:38.33	37.48	20.69	10	89.36	48.14	4.68
1997, 332	22:53:42.61	-13.77	-68.8	599.8	48.96	160.96	7.36
1997, 345	07:56:29.66	3.97	-75.77	182.4	30.16	164.58	8.79
1997, 347	19:22:58.96	-41.39	-87.39	10	74.52	183.06	5.81
1998, 088	20:38:37.98	-17.6499	-178.9630	493	103.98	257.98	4.44 (Pdif)
1998, 091	22:42:59.08	-40.28	-74.92	19	73.75	173.2	5.87
1998, 093	22:01:51.92	-8.08	-74.92	170.1	42.05	167.31	8.09
1998, 158	16:10:45.33	-31.47	-67.79	103	66.21	165.38	6.39
1998, 210	07:14:24.99	-32.27	-71.22	56	66.34	168.68	6.40
1998, 216	18:59:22.34	-0.55	-80.32	46.6	33.91	174.35	8.66
1998, 281	04:51:40.41	-16.05	-71.35	111.6	50.53	164.84	7.52
1999, 025	18:19:18.18	4.47	-75.68	24.3	29.7	164.18	8.85
1999, 079	10:47:45.09	51.56	-177.72	25.8	67.08	317.48	6.36
1999, 090	05:54:45.02	6.11	-82.71	10	27.17	178.33	8.99/9.93

Date (Julian)	Time (UTC h:m:s)	Latitude (deg)	Longitude (deg)	Depth (km)	Distance (deg)	Back Azimuth (deg)	Ray Parameter (sec/deg)
1999, 147	08:08:58.70	58.65	-137.18	10	43.49	322.16	8.06
1999, 183	11:45:32.01	49.33	-129.15	10	37.17	309.23	8.48
1999, 316	16:57:19.82	40.81	31.19	10.4	84.72	43.85	5.03
1999, 325	06:50:50.53	-63.19	-164.51	10	115.43	209.73	4.44 (Pdif)
2000, 058	16:10:42.44	7.94	-82.86	36.5	25.35	178.6	9.08/10.2
2000, 075	06:35:05.79	-44.31	-117.36	10	83.29	203.77	5.15
2000, 114	09:27:23.03	-28.29	-62.94	603.6	64.38	159.94	6.30
2000, 143	13:15:10.66	-4.05	-81.03	44.5	37.33	175.99	8.46
2000, 158	02:41:53.00	40.65	32.92	33	85.87	43.11	4.94
2000, 168	07:55:35.08	-33.81	-70.06	113.7	68.04	167.99	6.26
2000, 216	19:25:55.80	-17.62	-71.72	30.6	51.97	165.73	7.45
2000, 234	09:16:28.00	-53.08	-46.33	33	92	158.63	4.61
2000, 255	17:28:01.30	-15.77	-173.74	116.3	98.74	256.94	4.44 (Pdif)
2000, 270	06:17:53.48	-17.26	-173.88	0	99.64	255.74	4.44 (Pdif)
2000, 278	14:37:45.04	11.15	-62.48	0	29.34	134.17	8.87
2000, 278	14:40:13.16	11.12	-62.56	110.3	29.32	134.34	8.84
2000, 279	13:39:12.59	31.8910	-40.9239	10	35.68	80.78	8.57
2000, 313	07:00:00.00	6.97	-77.81	33	26.83	167.48	9.00/9.96
2000, 315	20:10:56.90	36.61	4.84	33	69.8	58.98	6.16
2002, 108	16:08:36.00	-27.34	-69.99	60.9	61.76	166.39	6.73
2002, 114	20:53:29.70	36.63	24.27	97.7	85.2	50.05	4.98
2002, 148	04:04:22.00	-28.89	-66.57	21.3	64	163.53	6.58
2002, 169	13:56:22.82	-30.79	-71.04	52.2	64.94	168.1	6.50
2002, 173	02:58:21.47	35.59	49.02	10	98.11	37.4	4.45
2002, 179	17:19:30.61	43.76	130.67	568	97.12	335.82	4.44 (Pdif)
2002, 190	18:40:35.63	43.52	-127.17	10	35.33	299.6	8.59
2002, 212	00:16:48.00	8.12	-82.57	33	25.18	177.91	9.08/10.2
2002, 215	02:42:11.15	8.24	-82.92	26.8	25.05	178.72	9.09/10.2
2002, 231	11:01:02.33	-21.6999	-179.4639	587.7	106.42	254.63	4.44 (Pdif)
2002, 249	01:21:28.60	38.38	13.7	10	75.13	53.79	5.77
2003, 309	00:58:51.11	4.97	-77.77	33	28.79	168.05	8.89
2004, 077	03:21:07.91	-21.12	-65.59	288.3	56.86	159.96	6.99
2005, 101	14:54:07.00	-7.28	-77.83	132.9	40.82	171.43	8.19

Appendix B
Gathers of receiver functions

The following are gathers of receiver functions. The gathers are shown for the Gaussian setting of 2.0 with variable trace spacing without moveout correction followed by gathers with moveout corrections for all four Gaussian settings except for the WEST azimuth. The WEST azimuth lacked events with a range of ray parameters and the majority of traces for this azimuth were greater than 100º away and had the same ray parameter. The parameters used for the moveout correction for station MYNC were V_P=6.5 with a reference ray parameter of 0.06 s/km. The values for V_P/V_S and H were taken from the $H - \kappa$ stacking results (Table 2) for each azimuth to get the optimal moveout correction.. The parameters used for the moveout correction for station GOGA were V_P=6.5 with a reference ray parameter of 0.06 s/km. The values for V_P/V_S and H were taken from the $H - \kappa$ stacking results (Table 1) for each azimuth to get the optimal moveout correction.

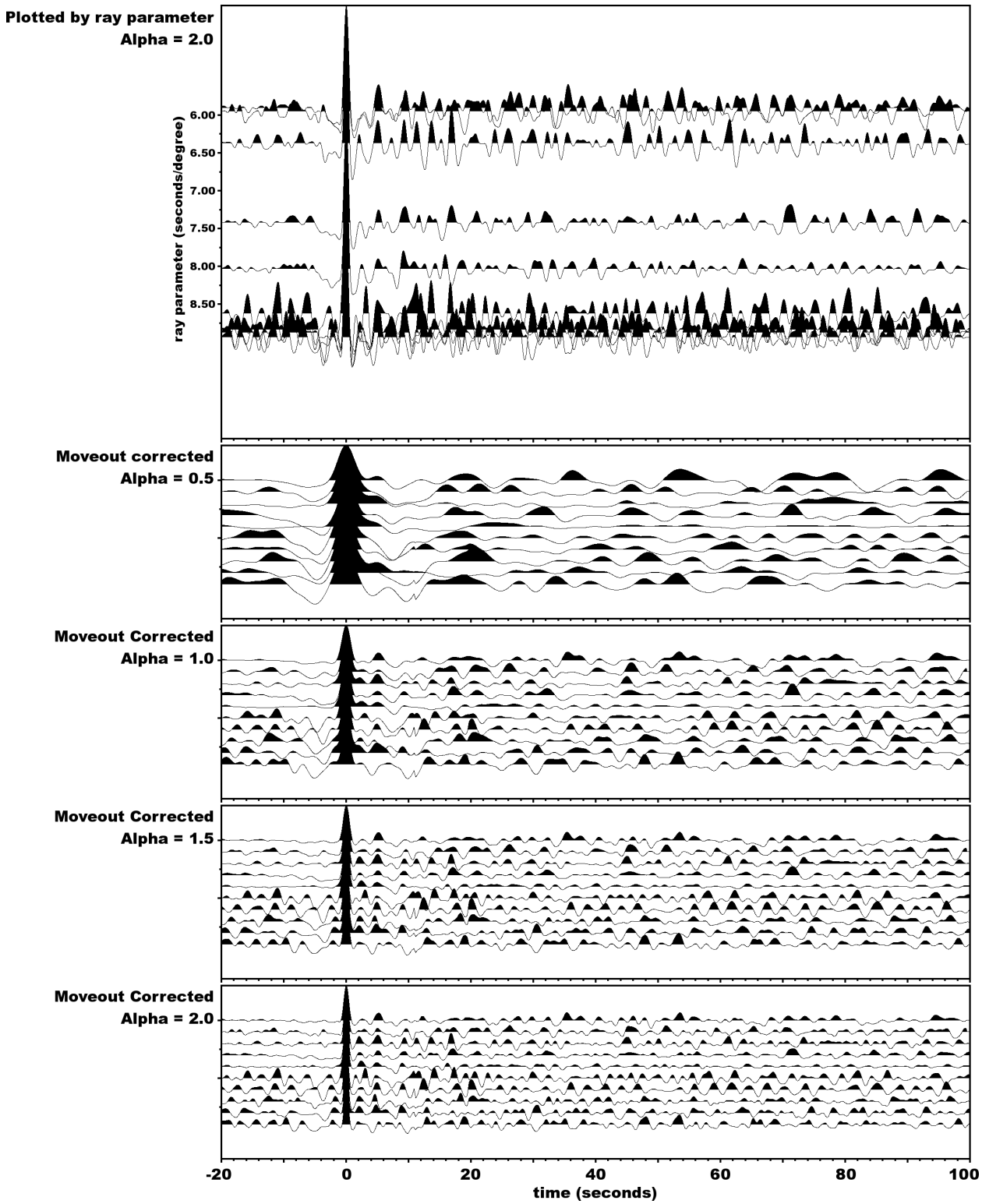

Figure B1: Gathers of receiver functions from the EAST azimuth for station GOGA

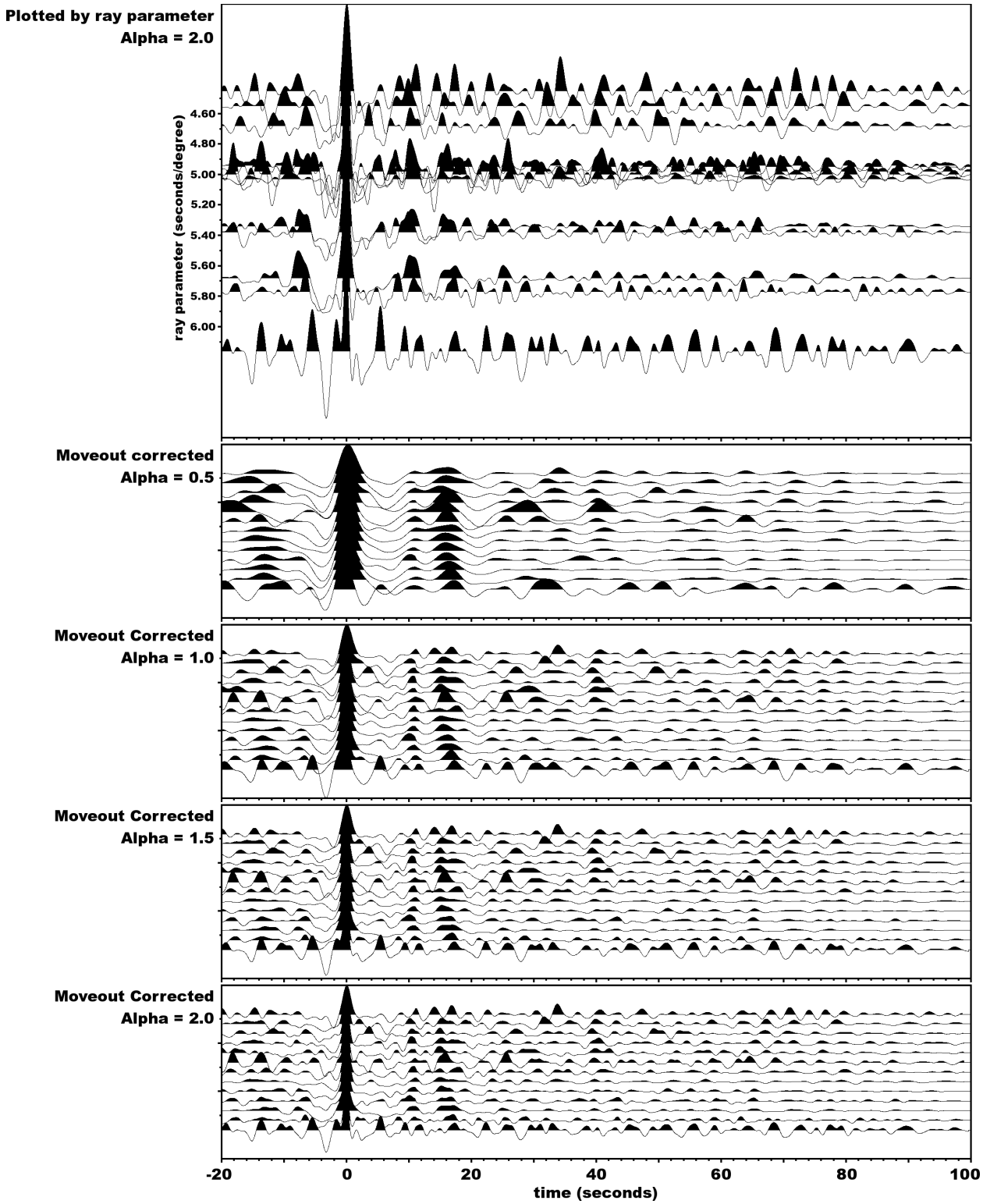

Figure B2: Gathers of receiver functions from the NE azimuth for station GOGA

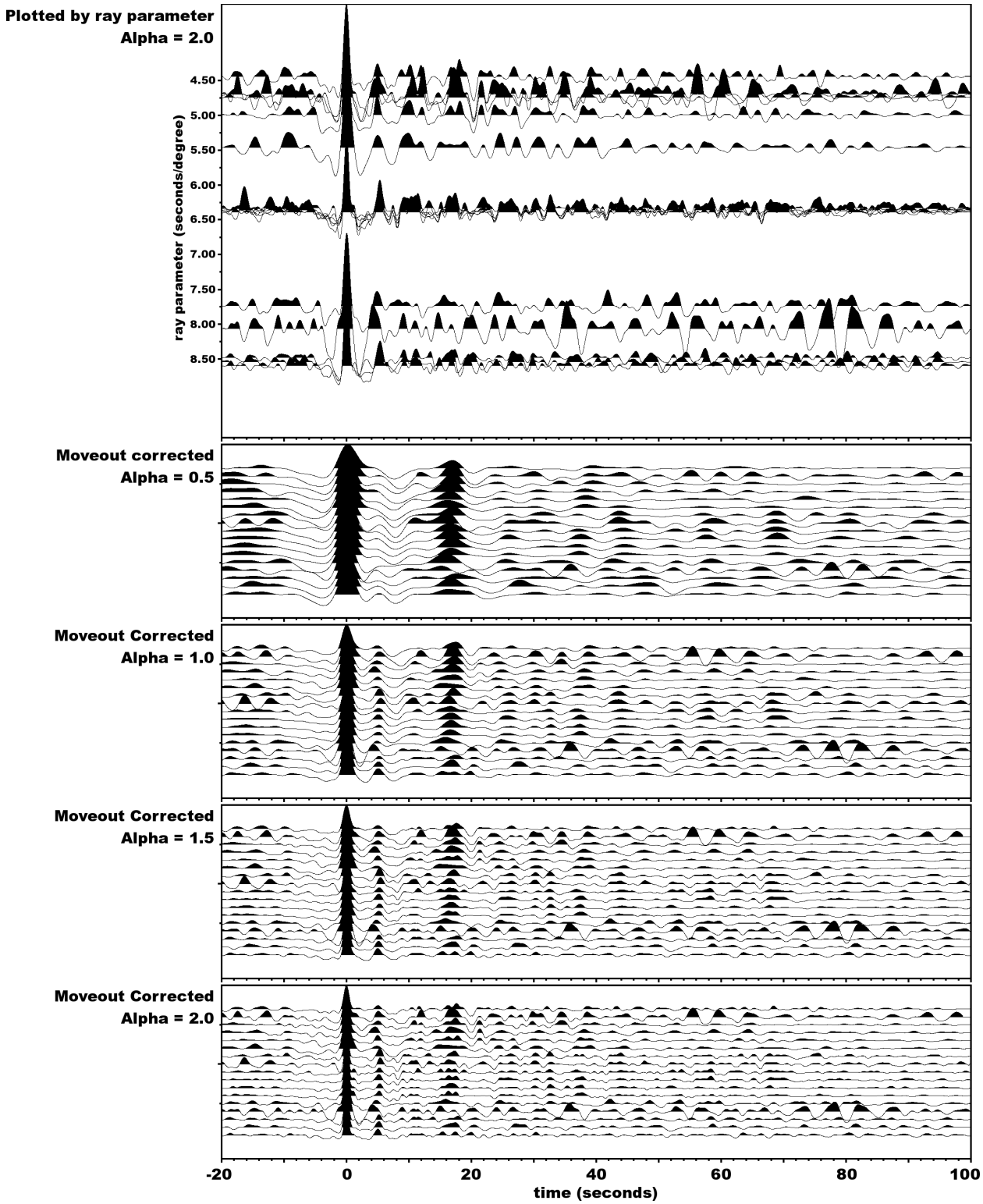

Figure B3: Gathers of receiver functions from the NW azimuth for station GOGA

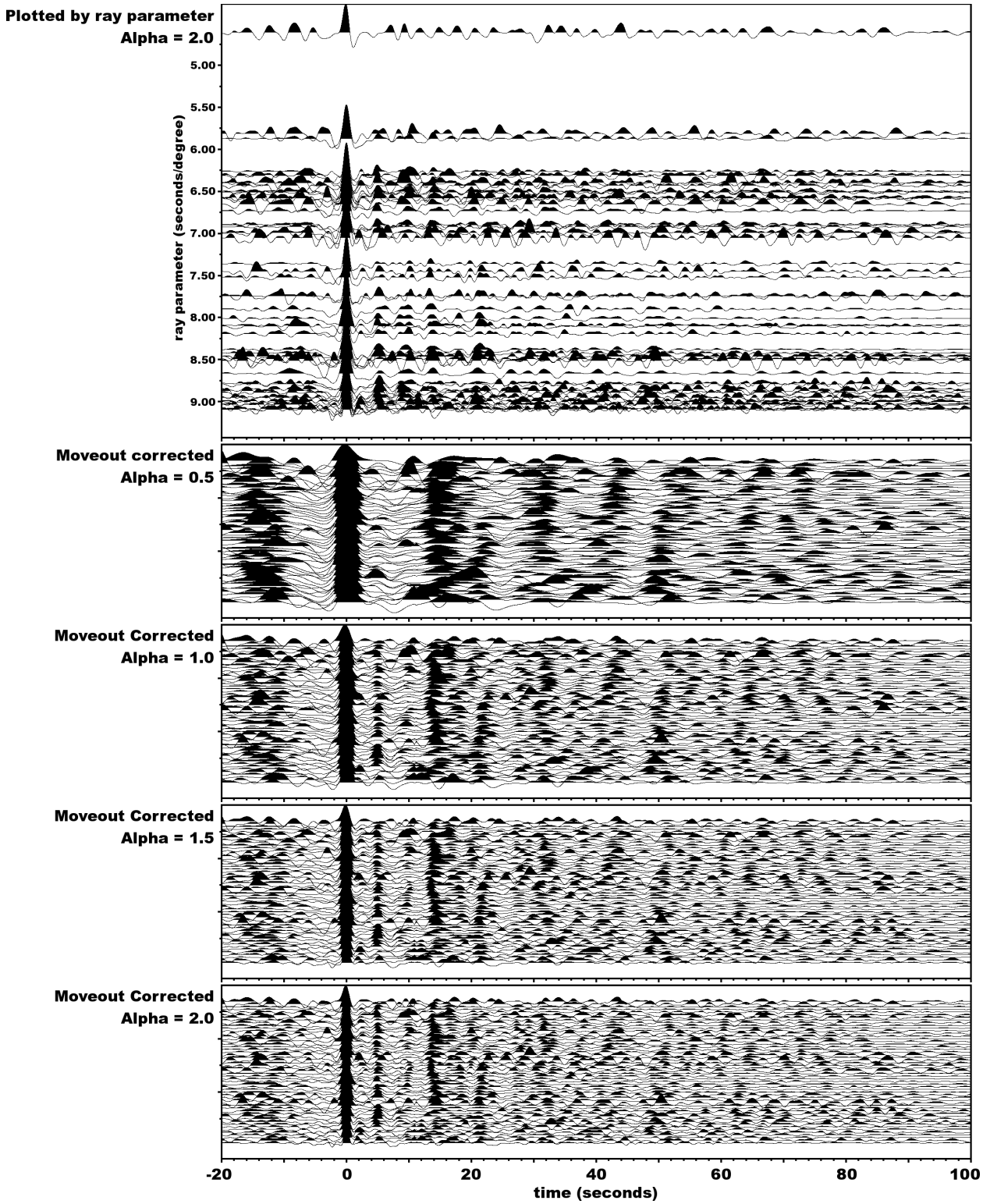

Figure B4: Gathers of receiver functions from the SA azimuth for station GOGA

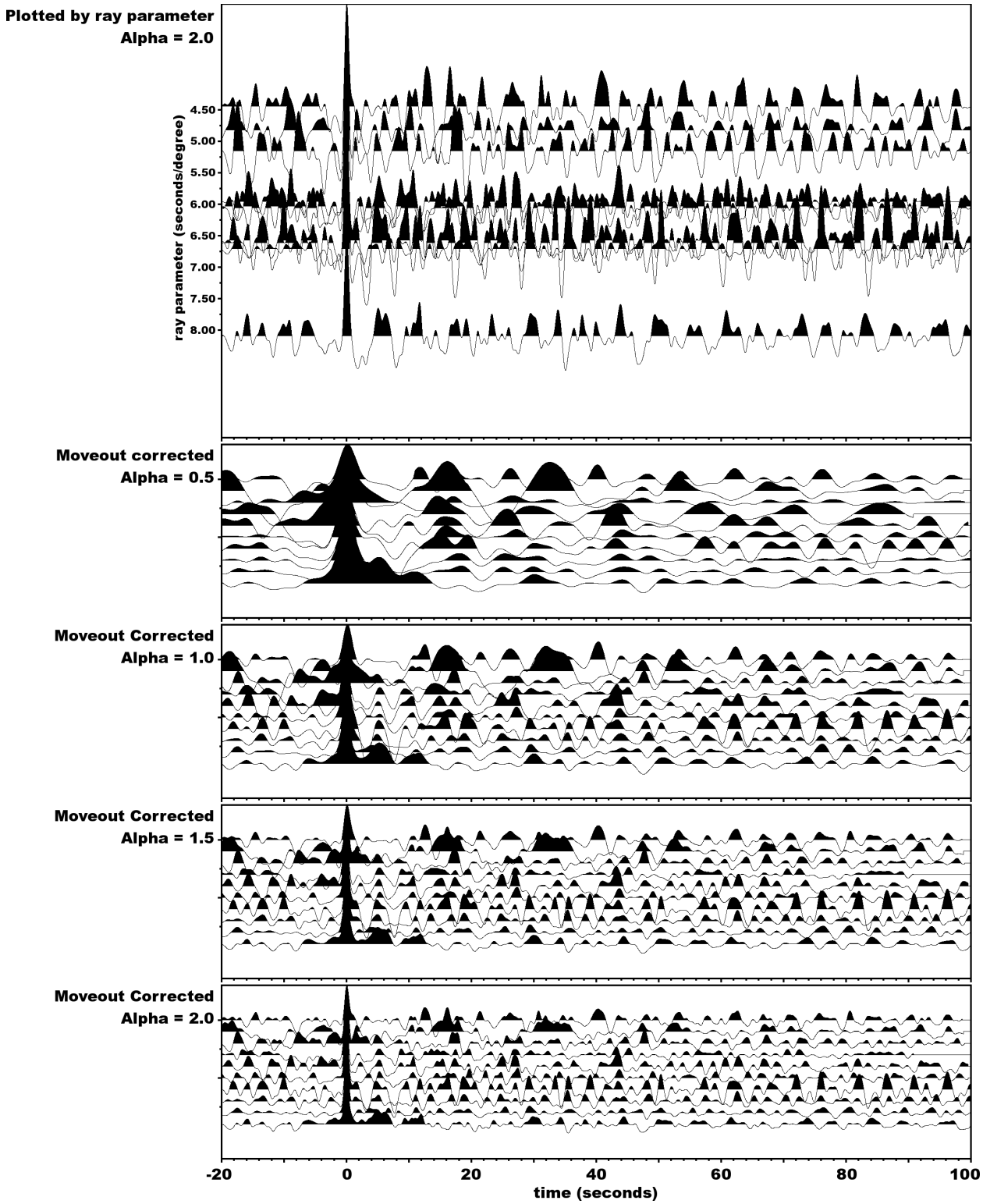

Figure B5: Gathers of receiver functions from the SSW azimuth for station GOGA

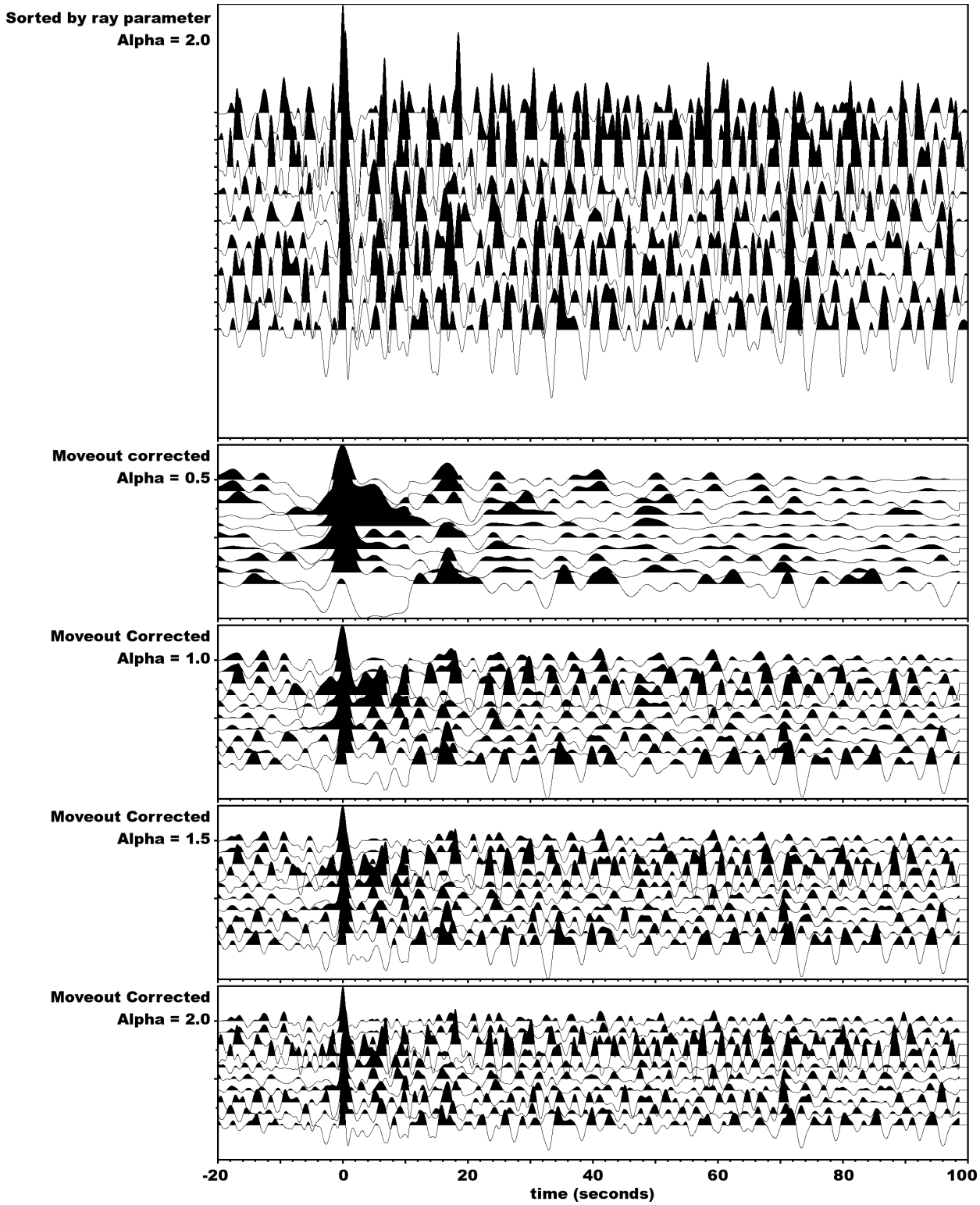

Figure B6: Gathers of receiver functions from the WEST azimuth for station GOGA

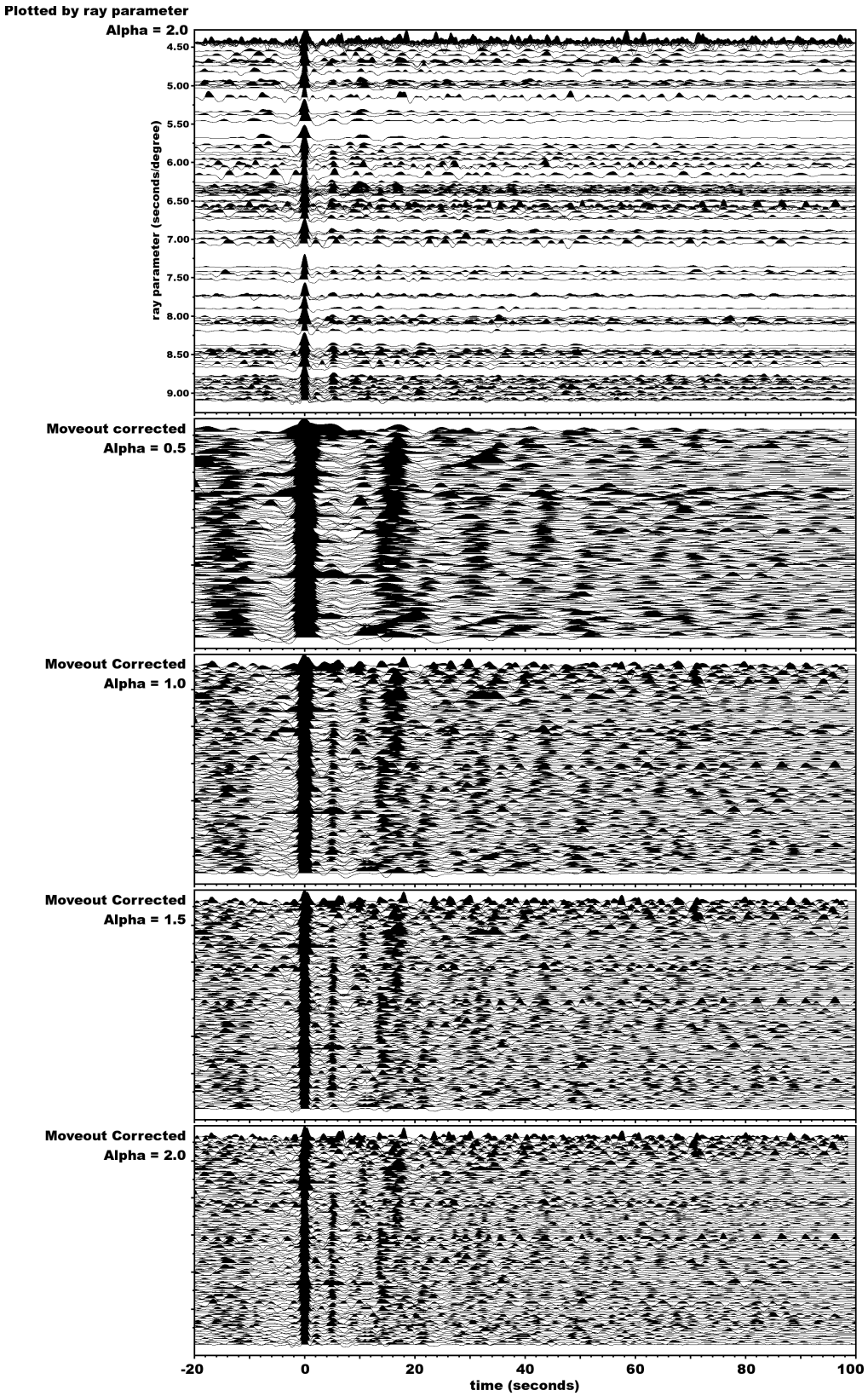

Figure B7: Gathers of receiver functions for all events for station GOGA

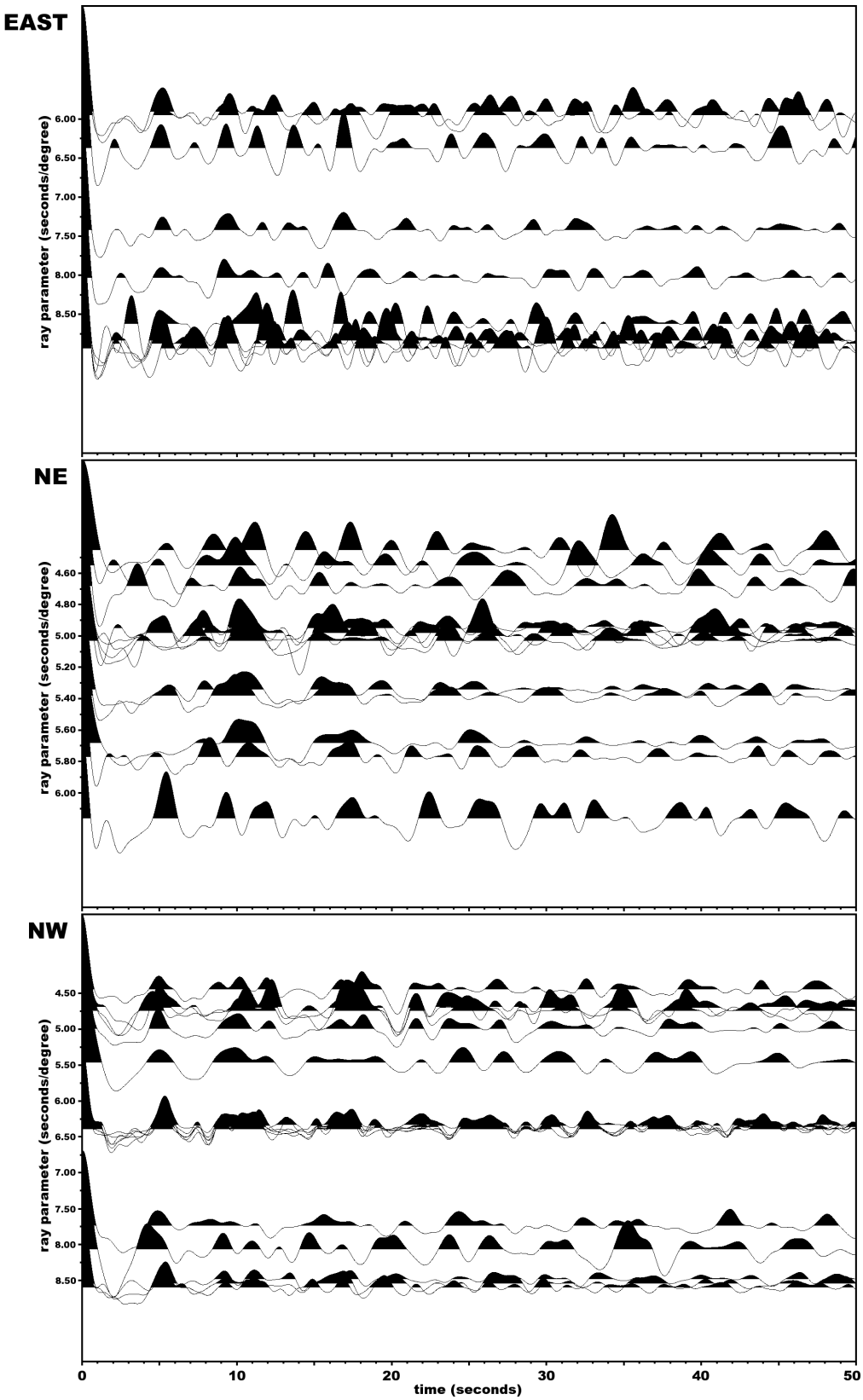

Figure B8: Partial gathers of receiver functions for station GOGA

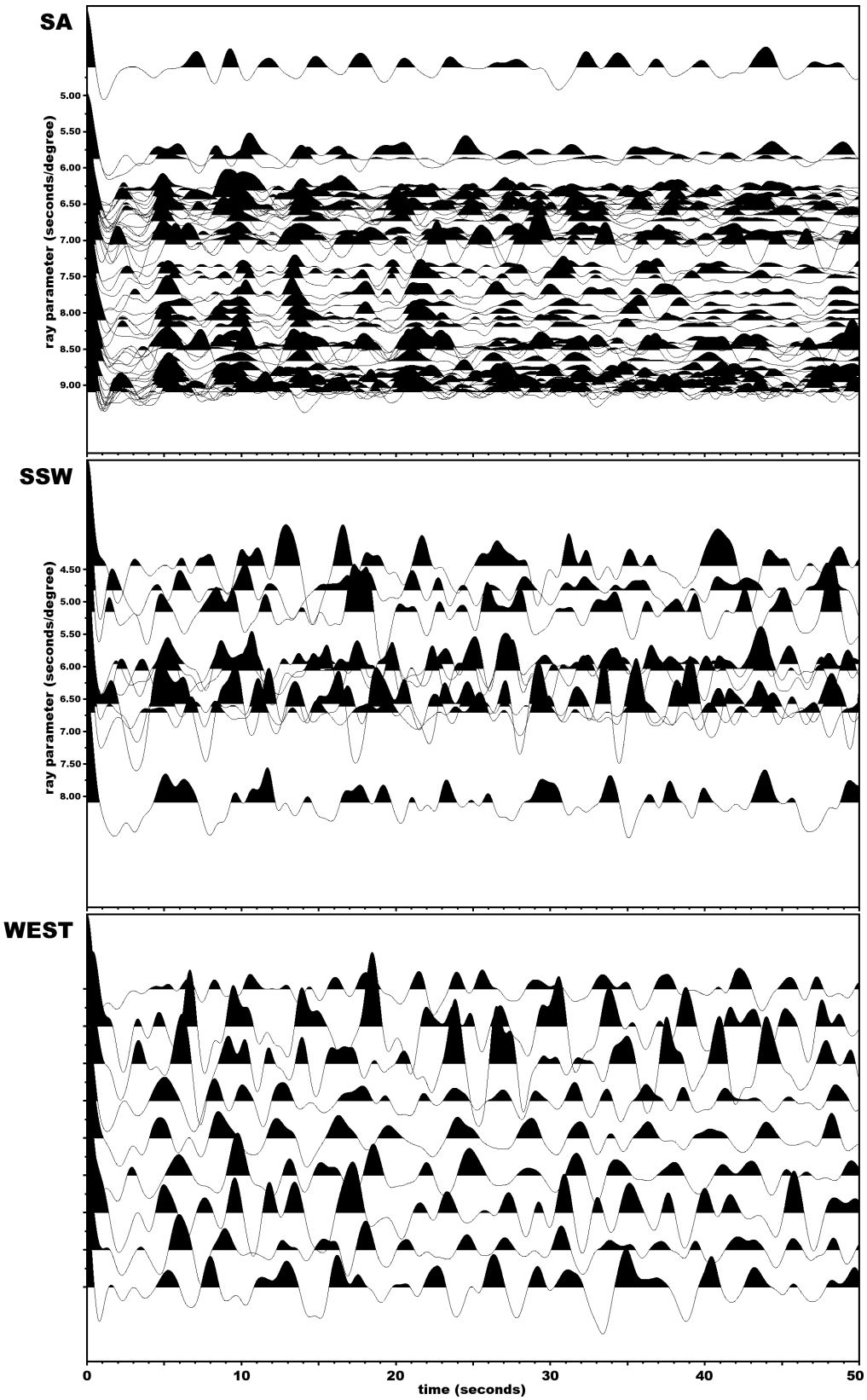

Figure B9: Partial gathers of receiver functions for station GOGA

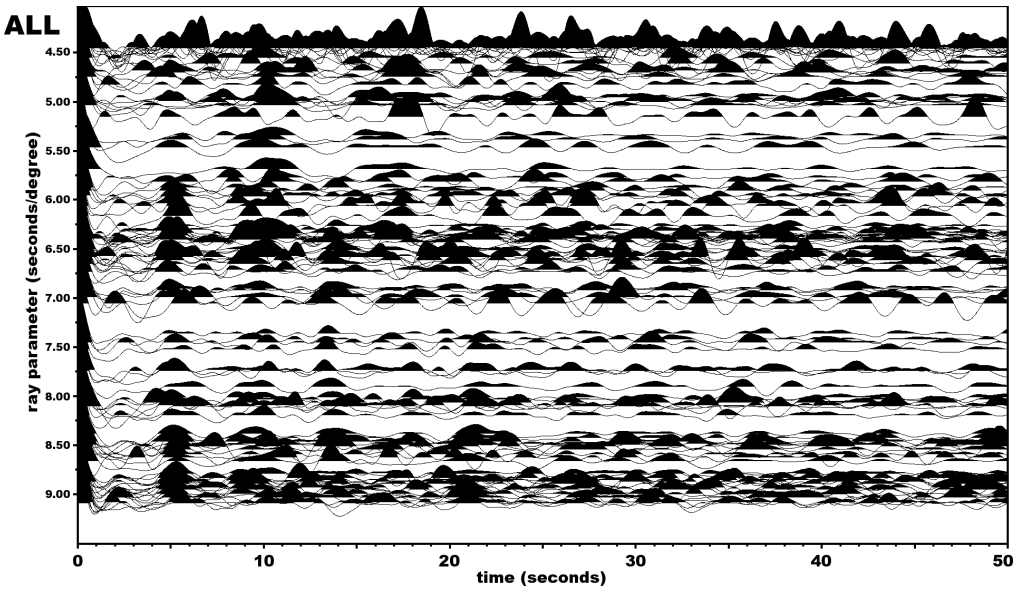

Figure B10: Partial gathers of receiver functions for station GOGA

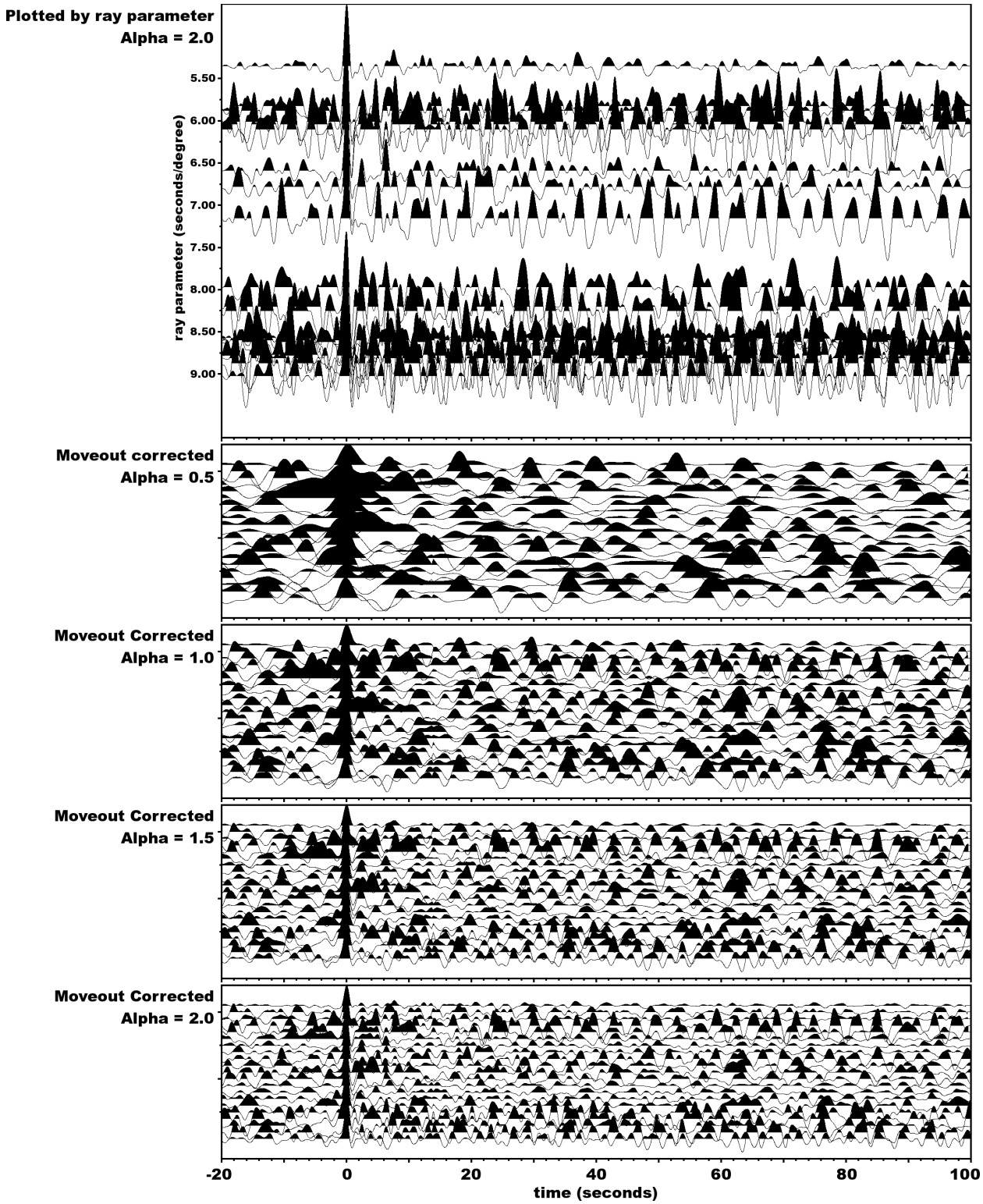

Figure B11: Gathers of receiver functions from the EAST azimuth for station MYNC

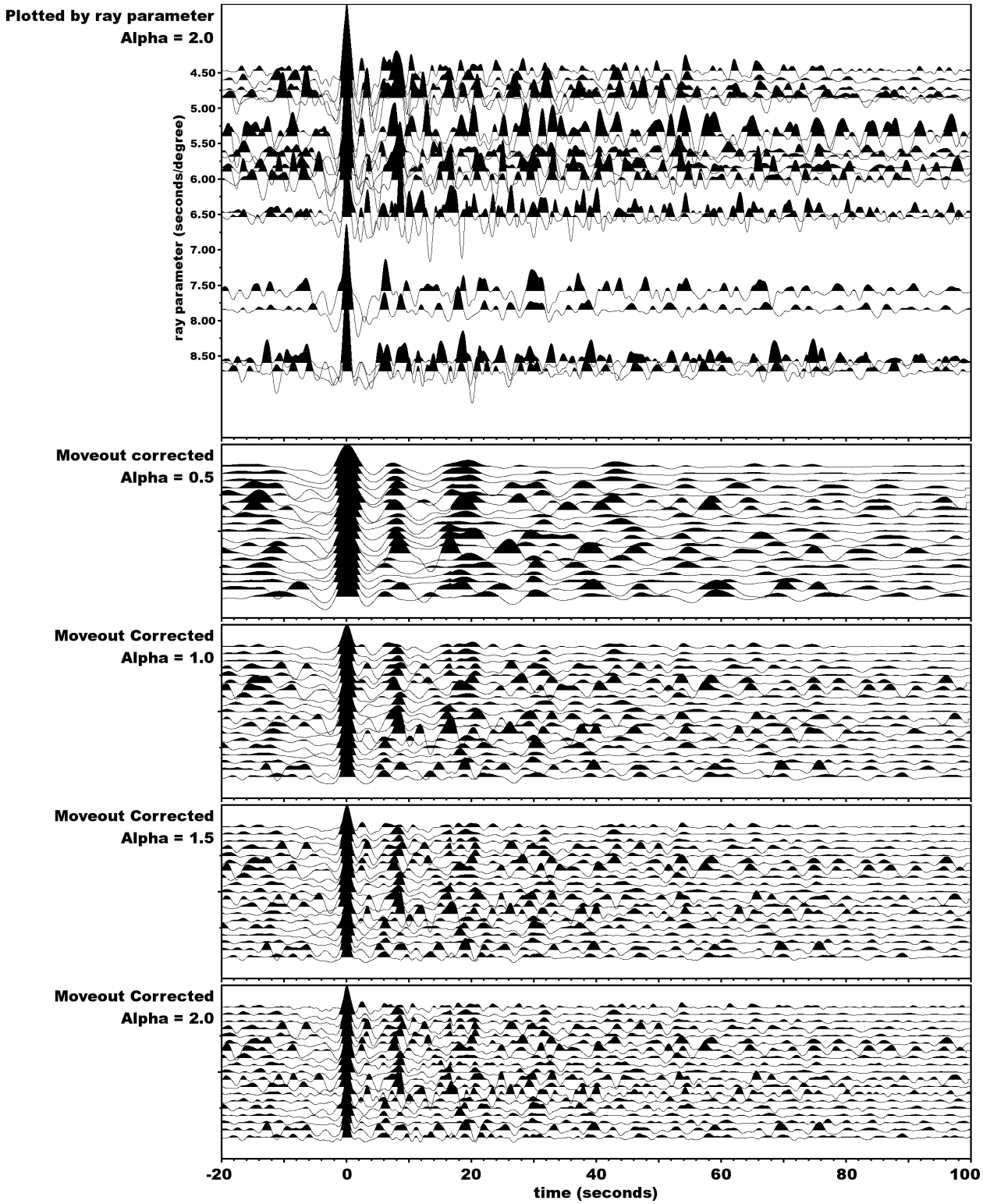

Figure B12: Gathers of receiver functions from the NW azimuth for station MYNC

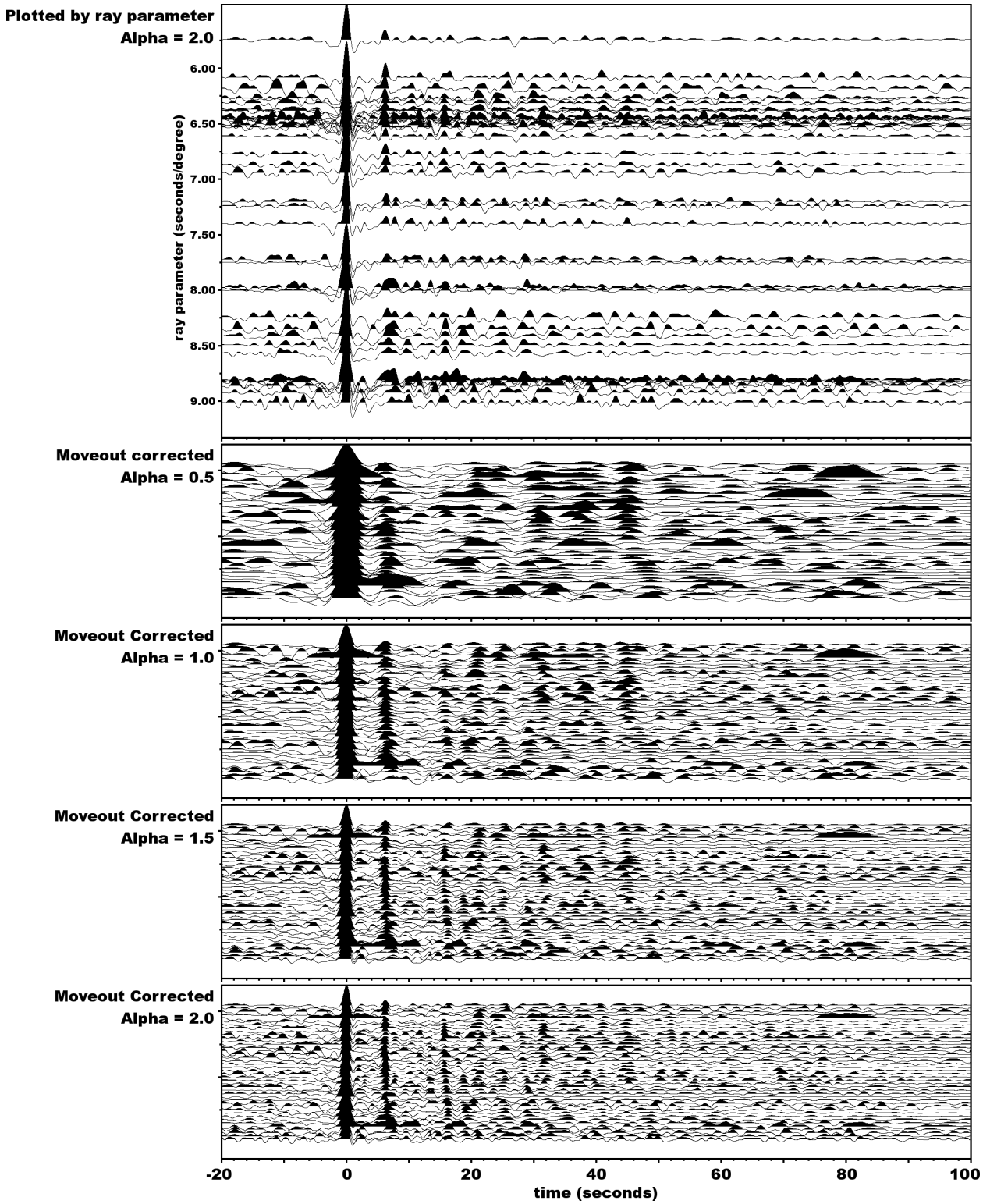

Figure B13: Gathers of receiver functions from the SA azimuth for station MYNC

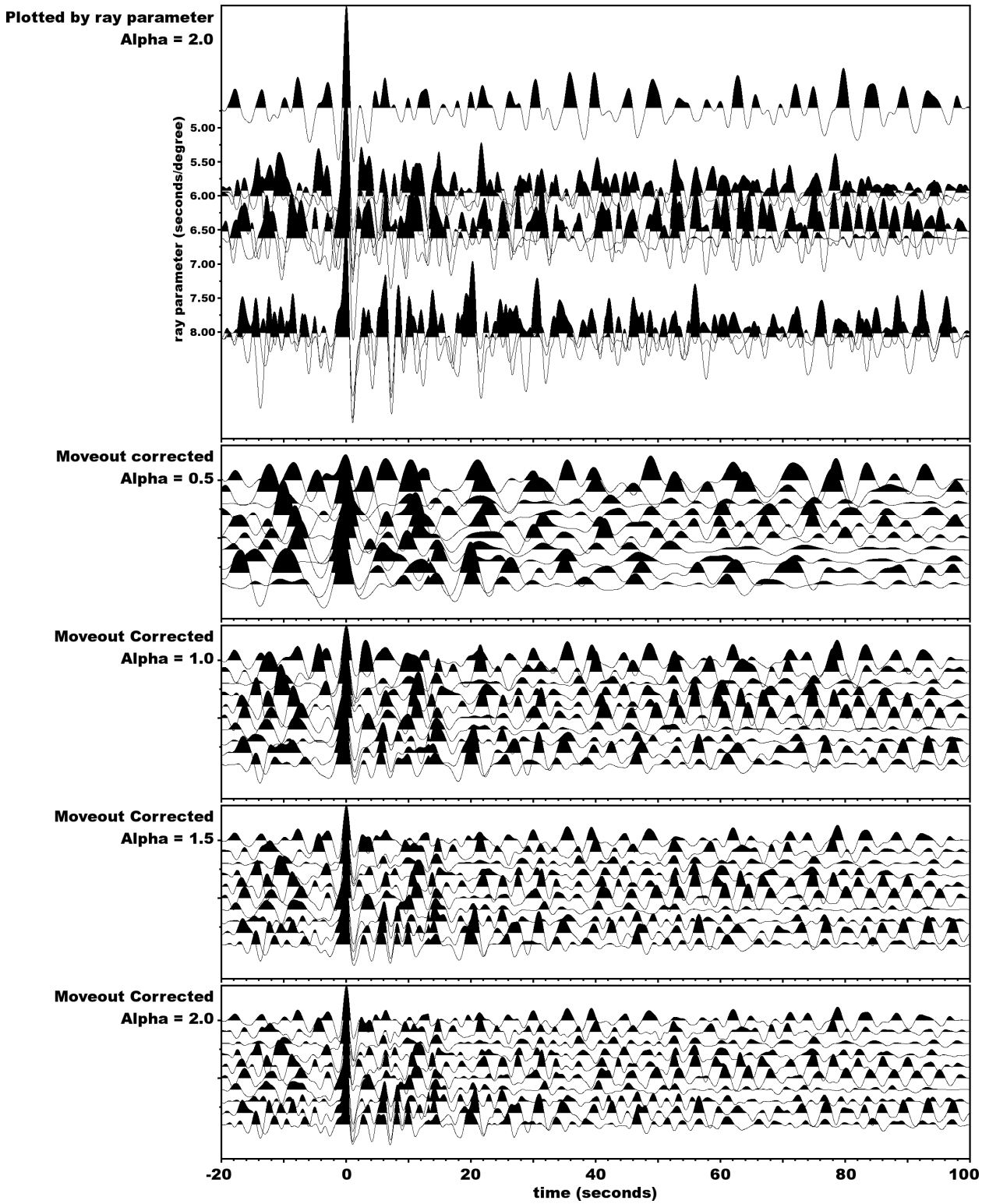

Figure B14: Gathers of receiver functions from the SSW azimuth for station MYNC

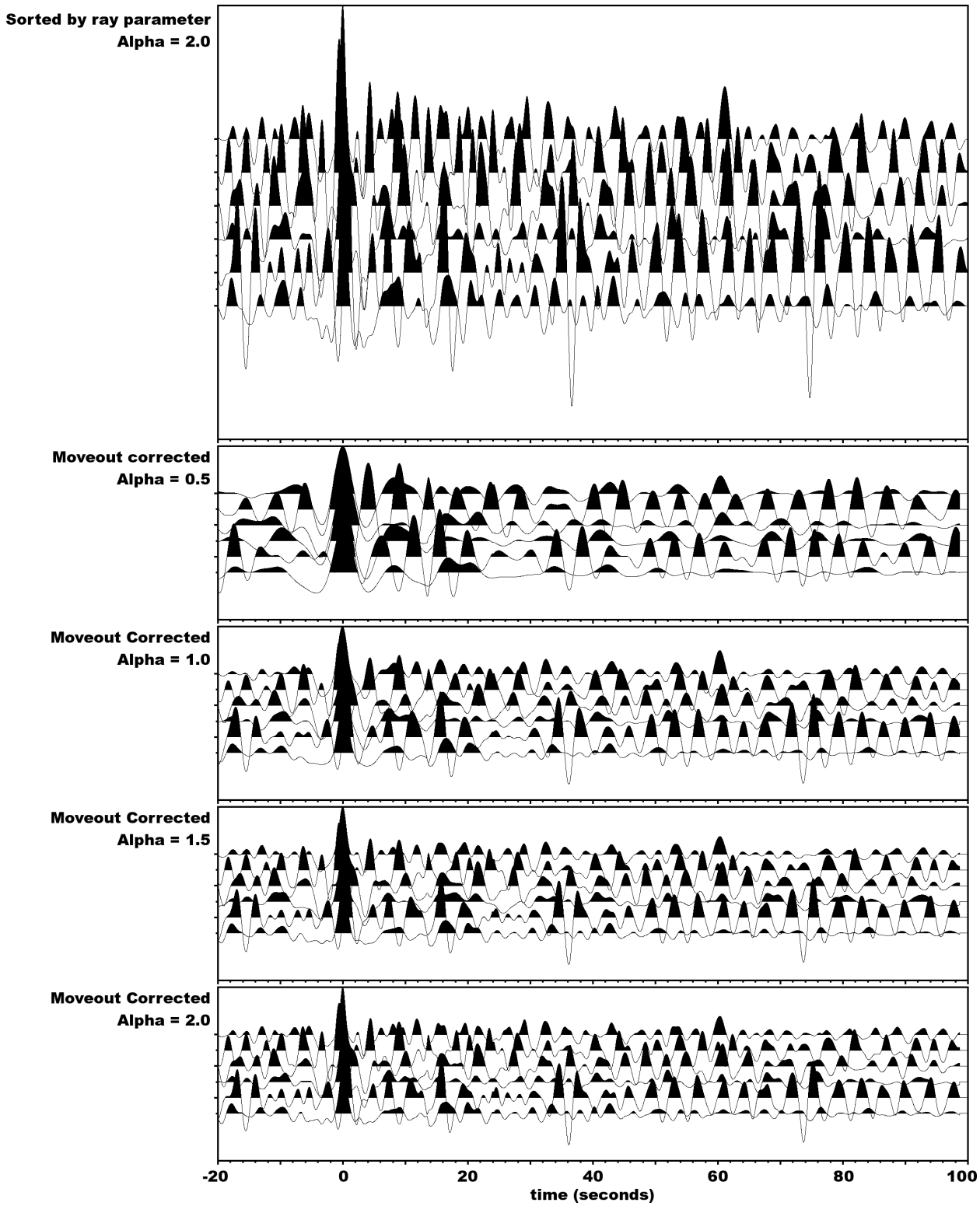

Figure B15: Gathers of receiver functions from the WEST azimuth for station MYNC

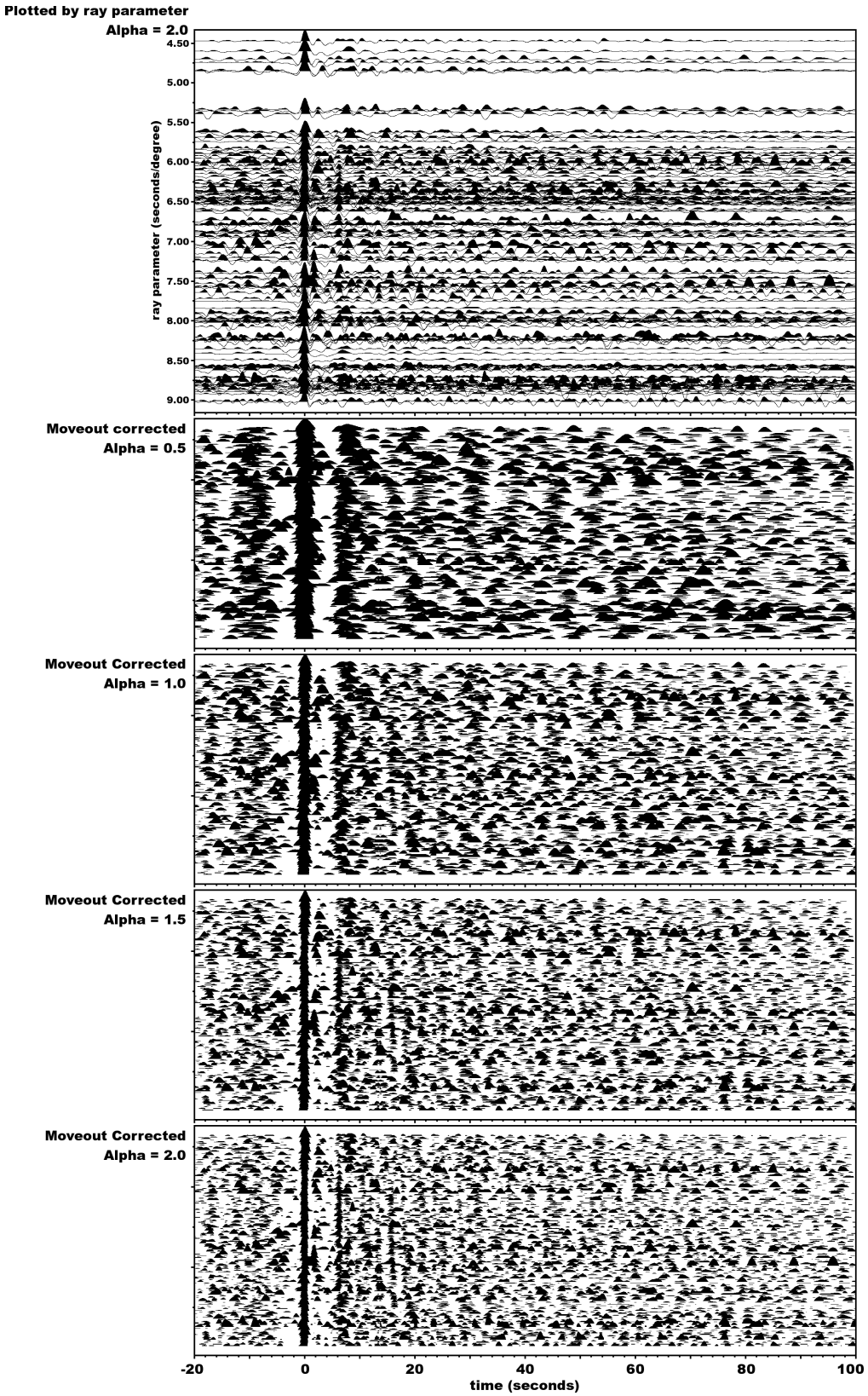

Figure B16: Gathers of receiver functions for all events for station MYNC

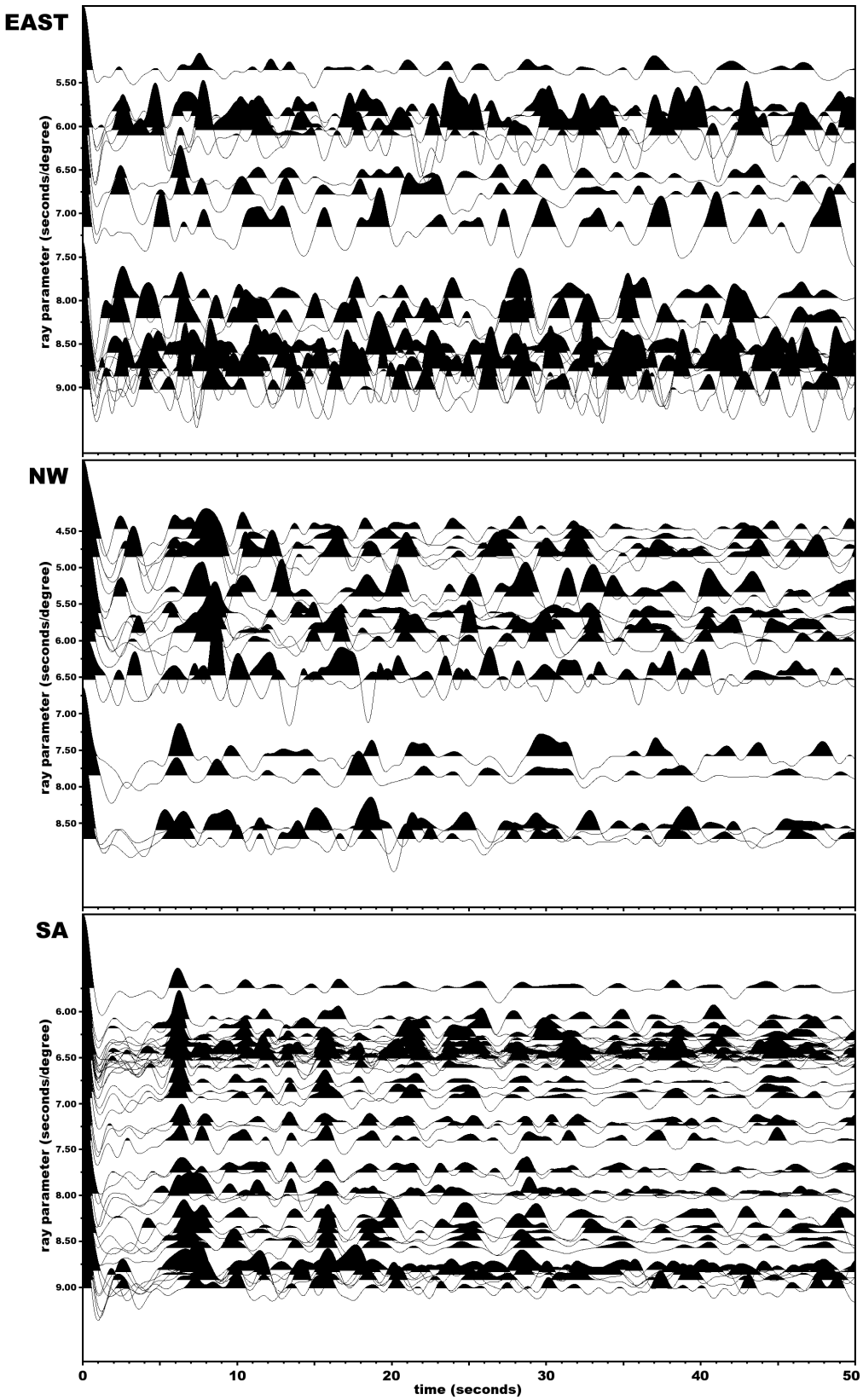

Figure B17: Partial gathers of receiver functions for station MYNC

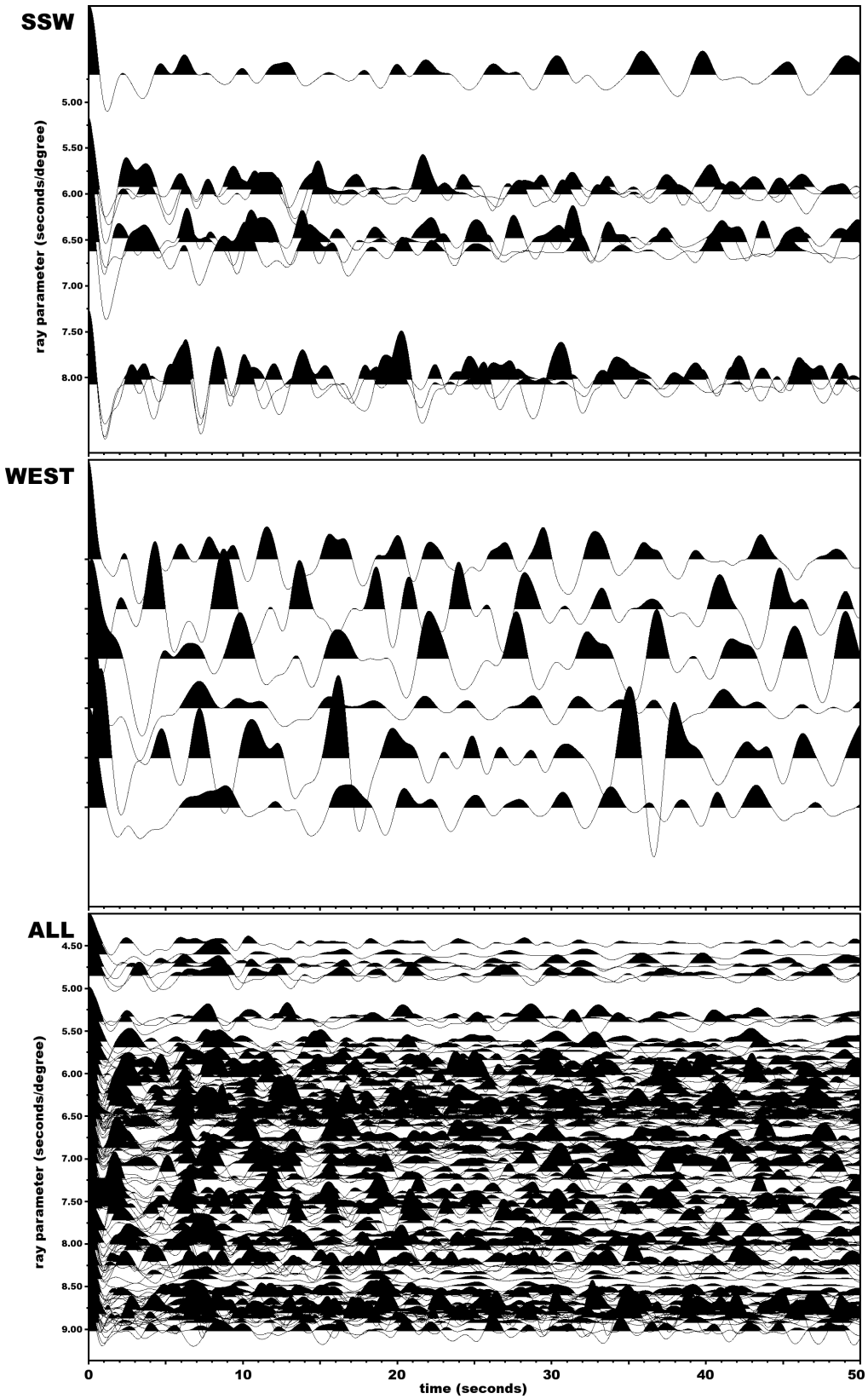

Figure B18: Partial gathers of receiver functions for station MYNC

Appendix C
H – κ stacks of receiver functions

The following figures are the results from the Zhu and Kanamori (2000) method for stacking receiver functions. The stacking was done on the gathers of receiver functions with alpha = 2.0. The range of V_P is from 6.1 km/s to 6.9 km/s and shows the variation in the thickness and V_P/V_S ratio within this range of V_P values. The arrows show the location of the peaks that represent the Moho.

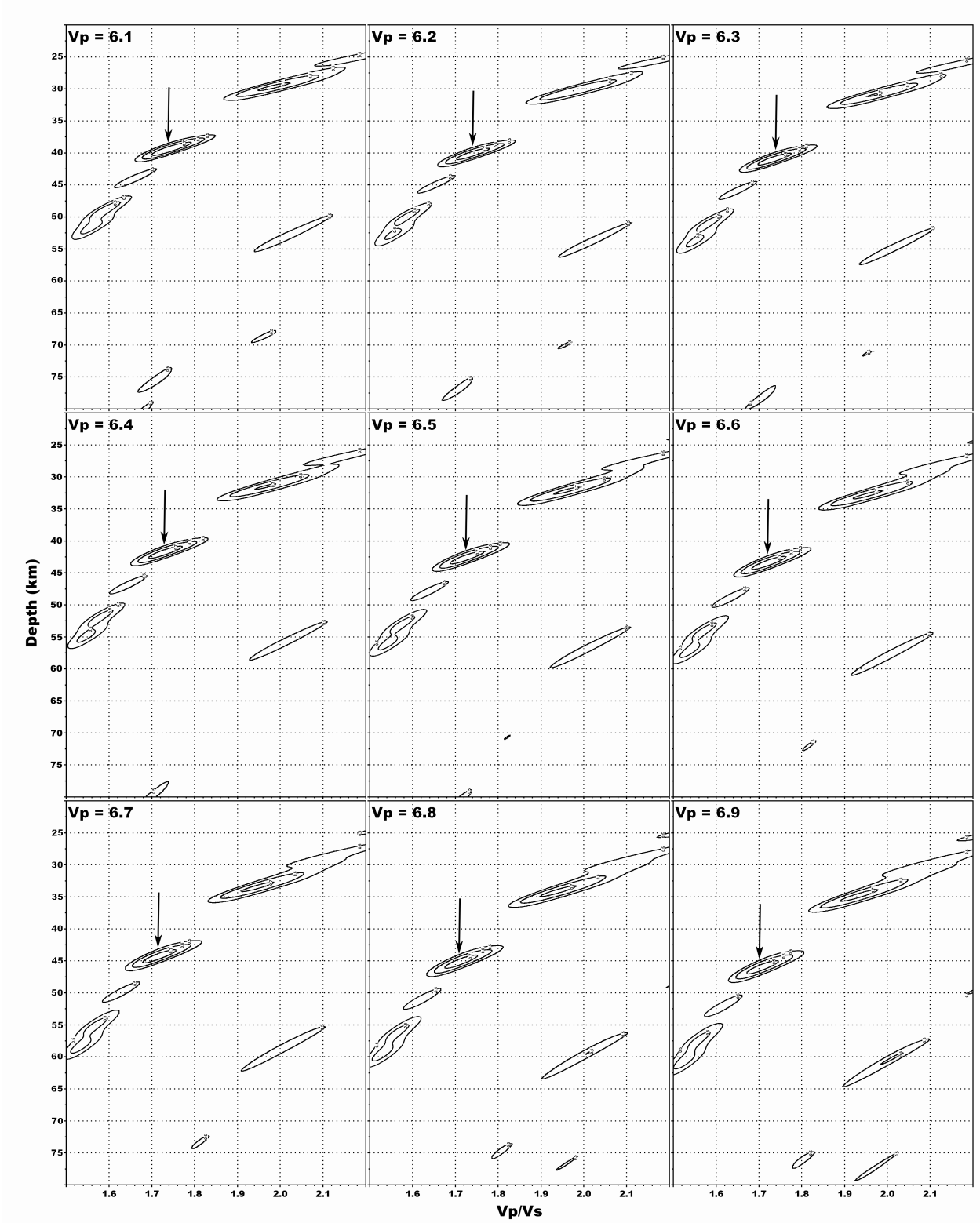

Figure C1: $H - \kappa$ stacks of receiver functions from the EAST azimuth for station GOGA

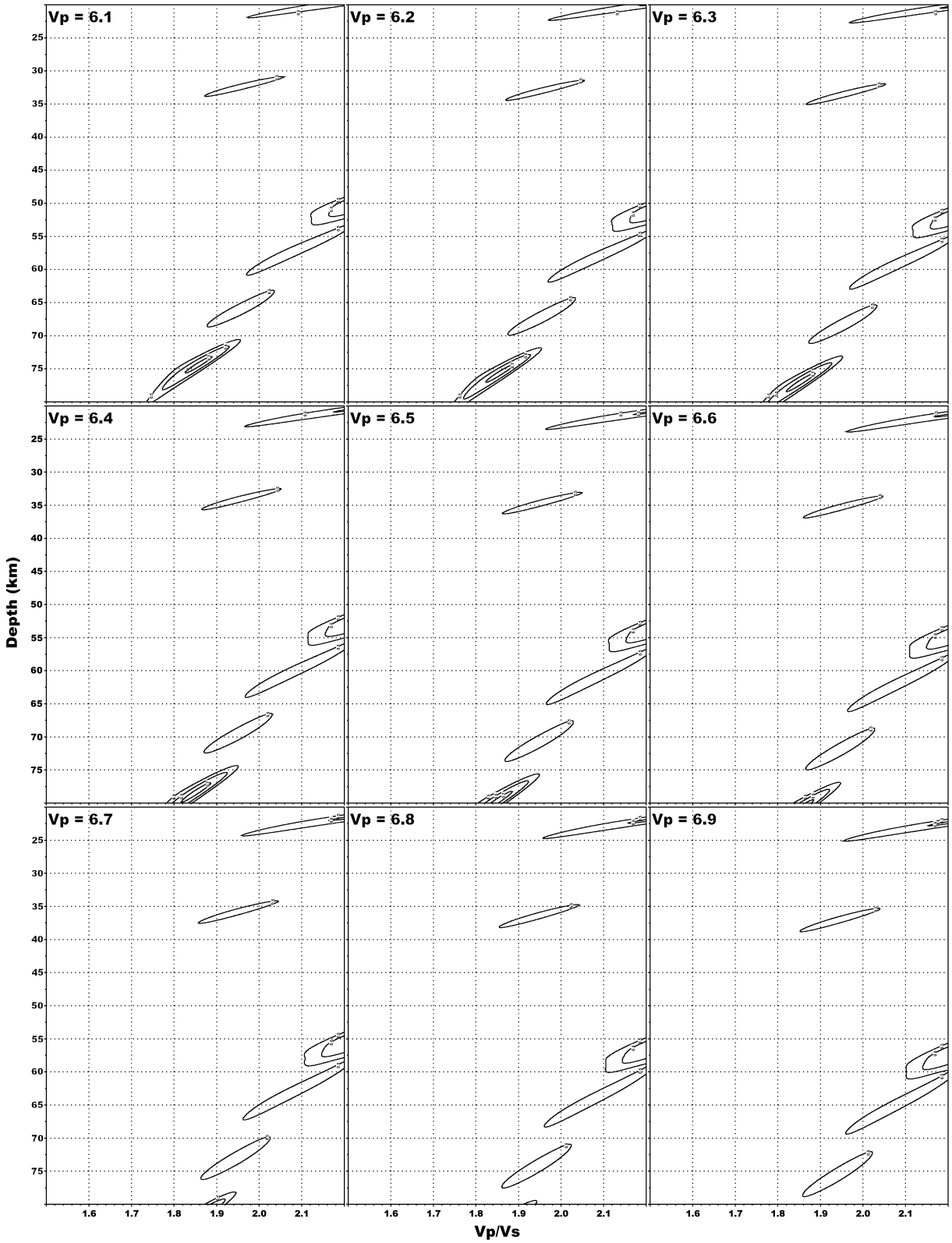

Figure C2: H – κ stacks of receiver functions from the NE azimuth for station GOGA

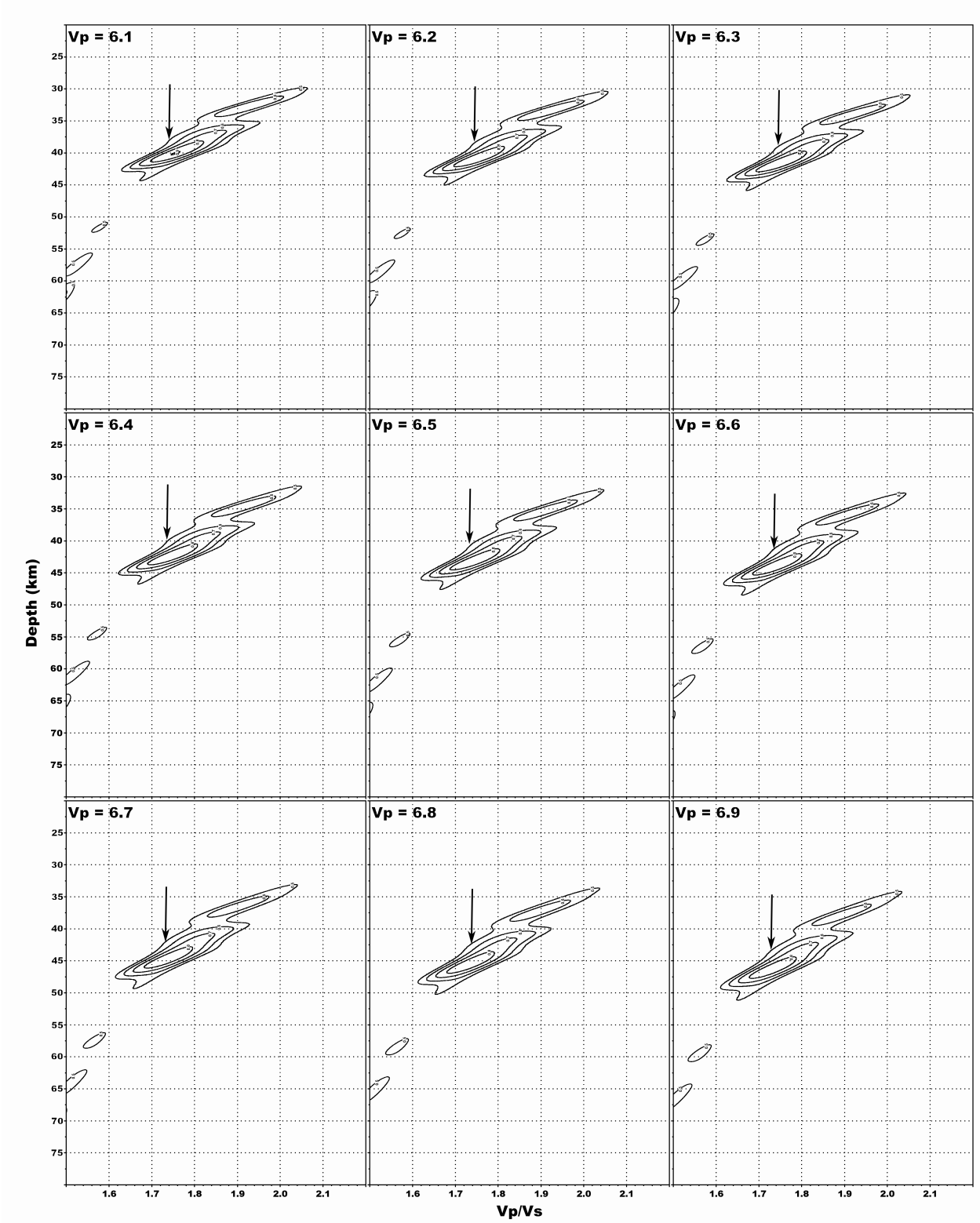

Figure C3: H – κ stacks of receiver functions from the NW azimuth for station GOGA

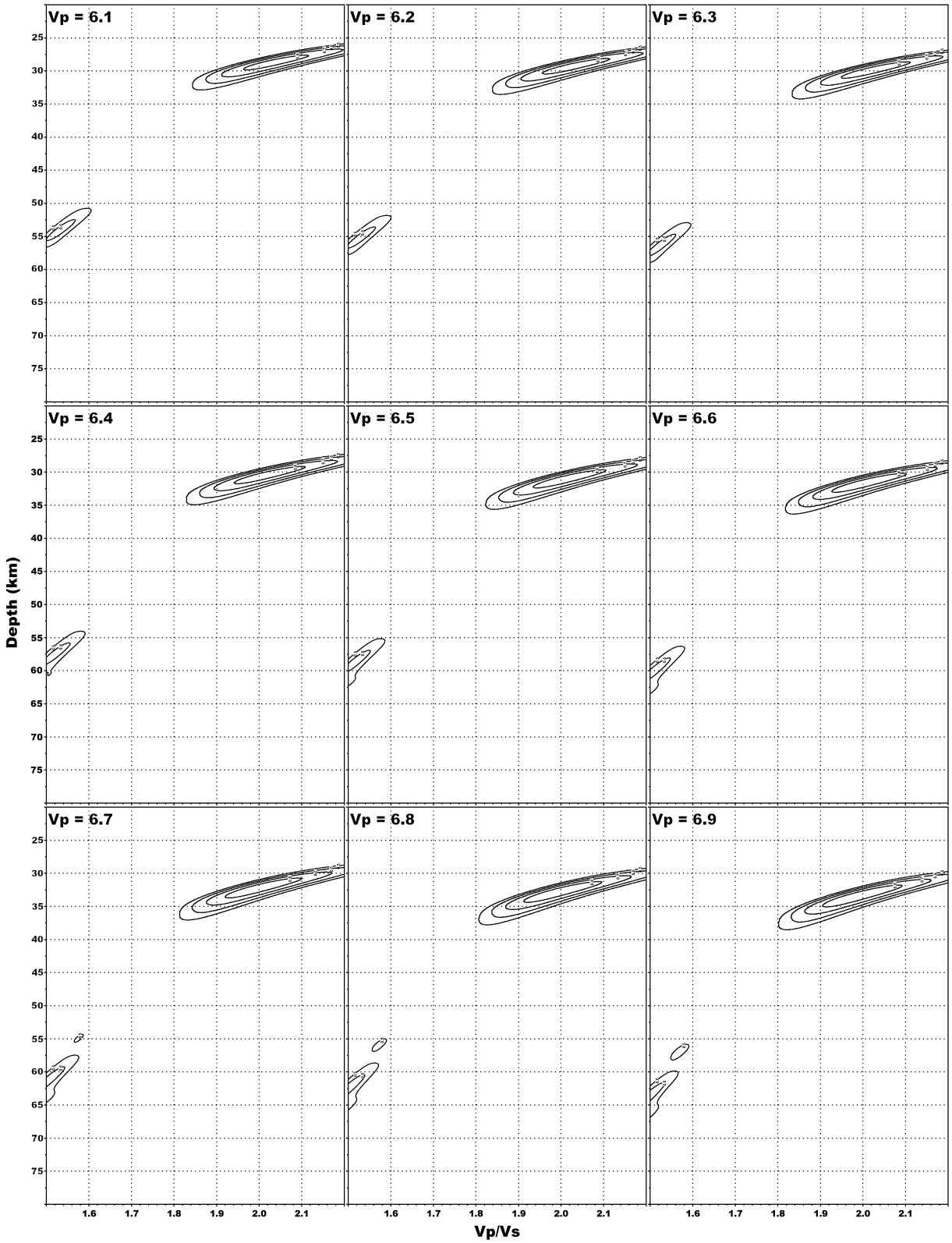

Figure C4: H – κ stacks of receiver functions from the SA azimuth for station GOGA

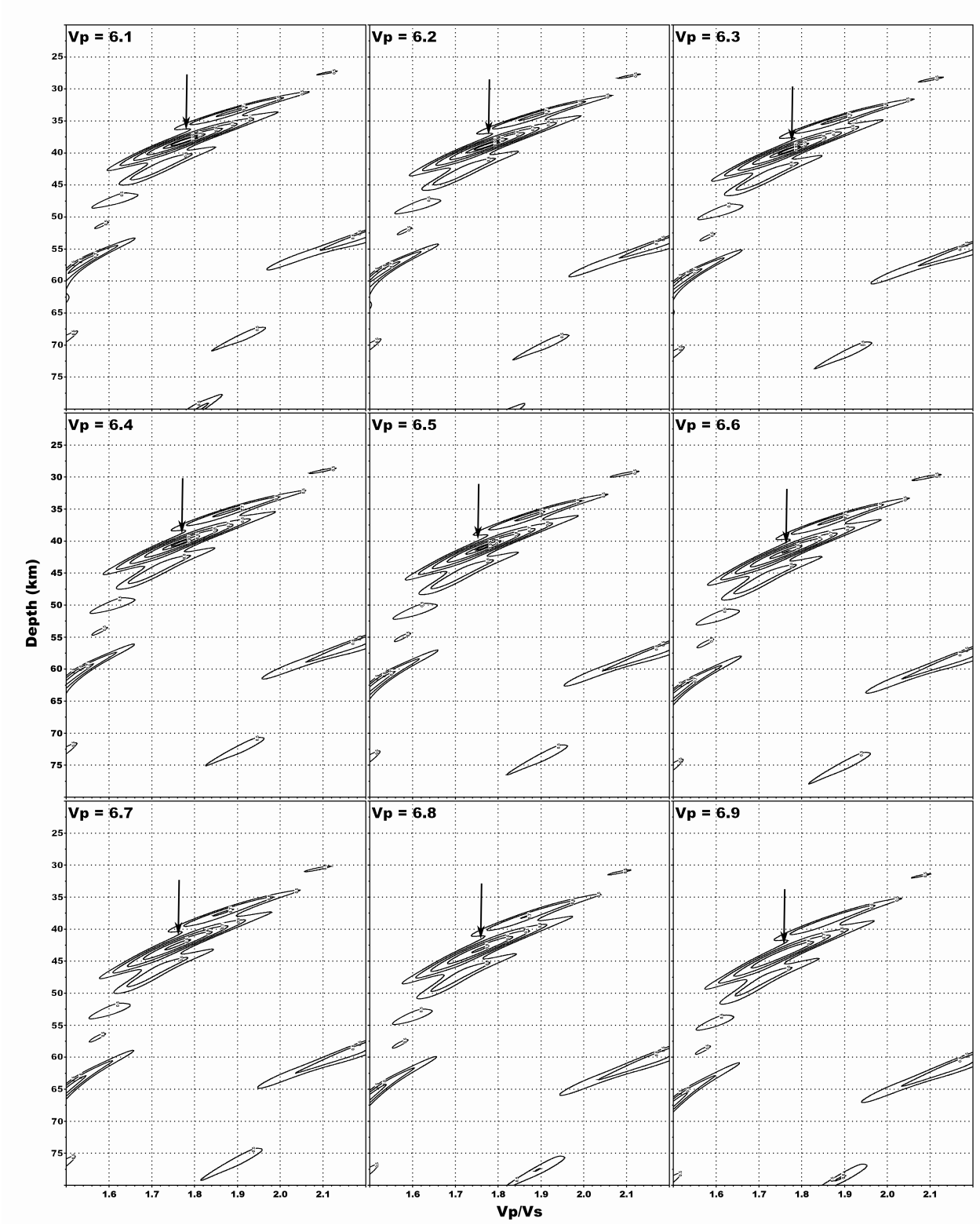

Figure C5: H – κ stacks of receiver functions from the SSW azimuth for station GOGA

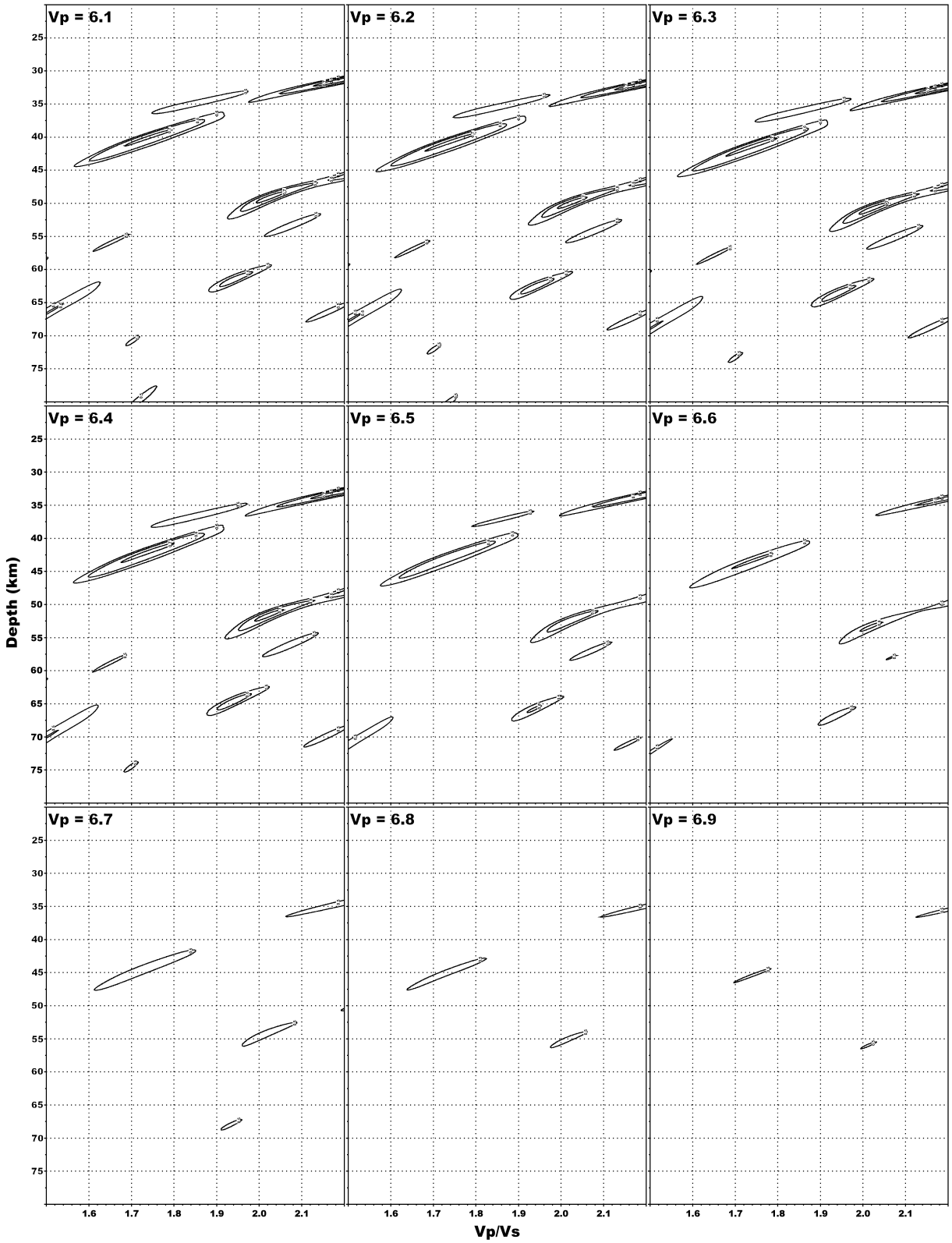

Figure C6: H – κ stacks of receiver functions from the WEST azimuth for station GOGA

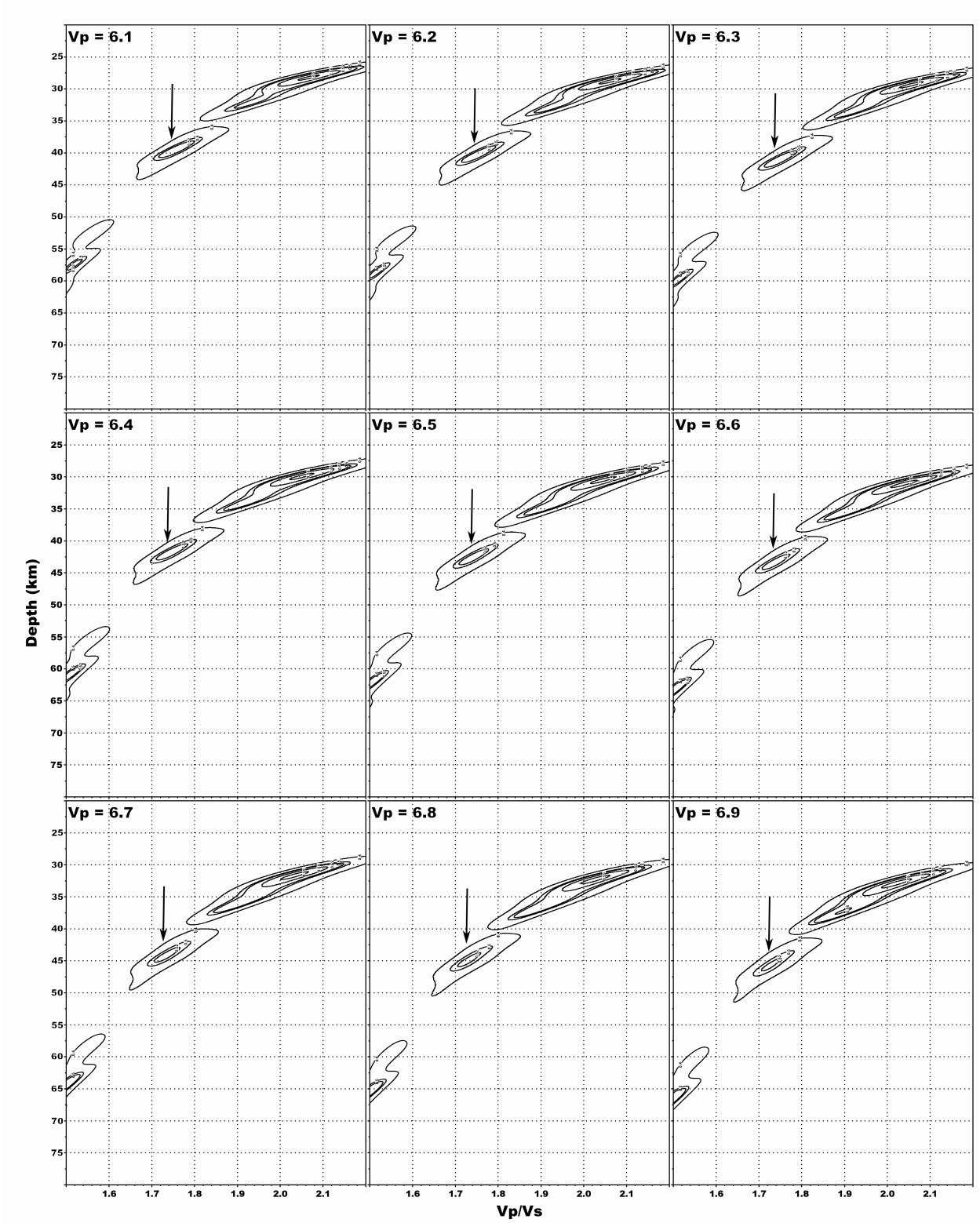

Figure C7: H – κ stacks of receiver functions for all events from station GOGA

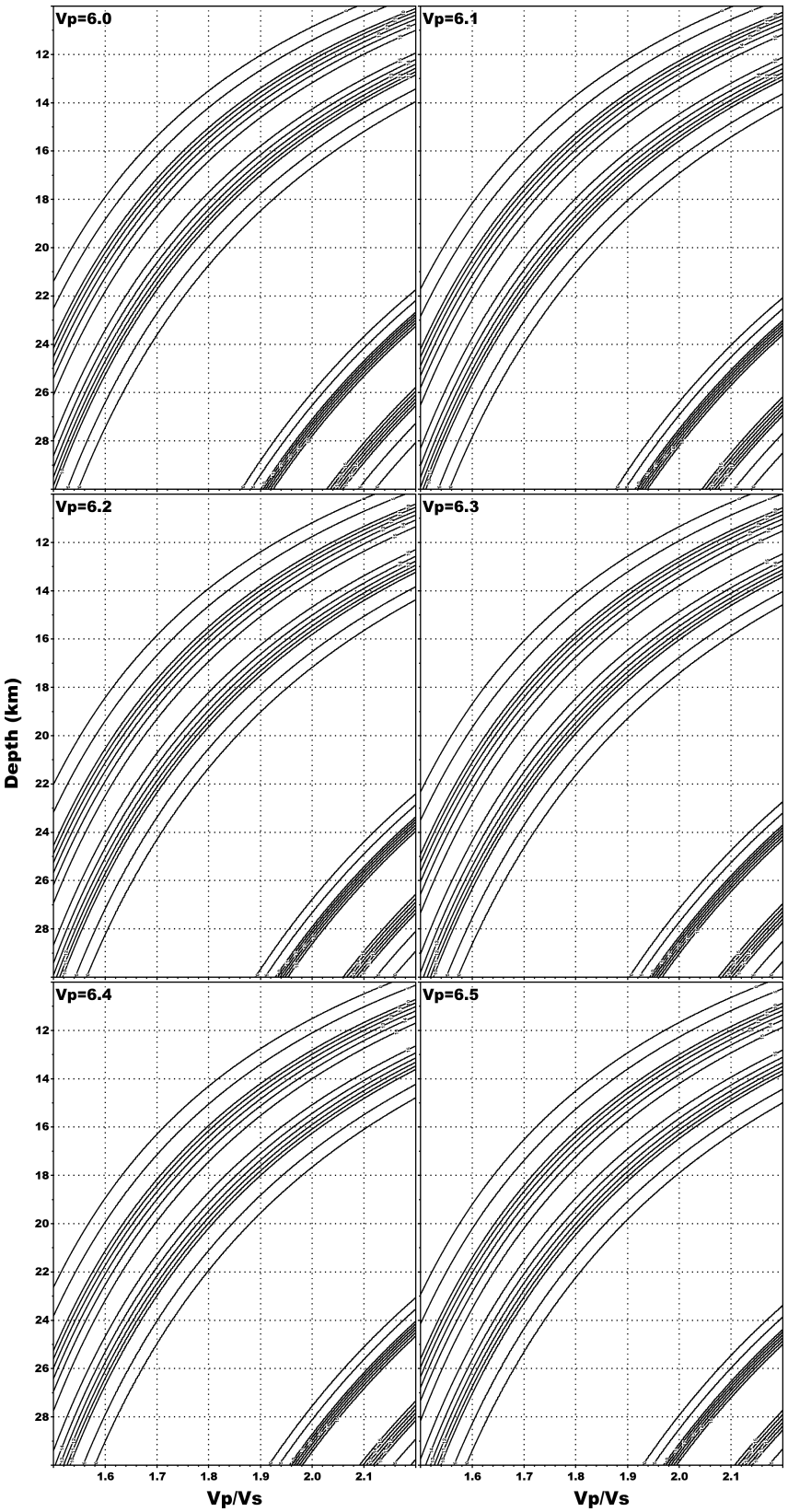

Figure C8: $H - \kappa$ stacks of receiver functions locating midcrustal arrival for GOGA

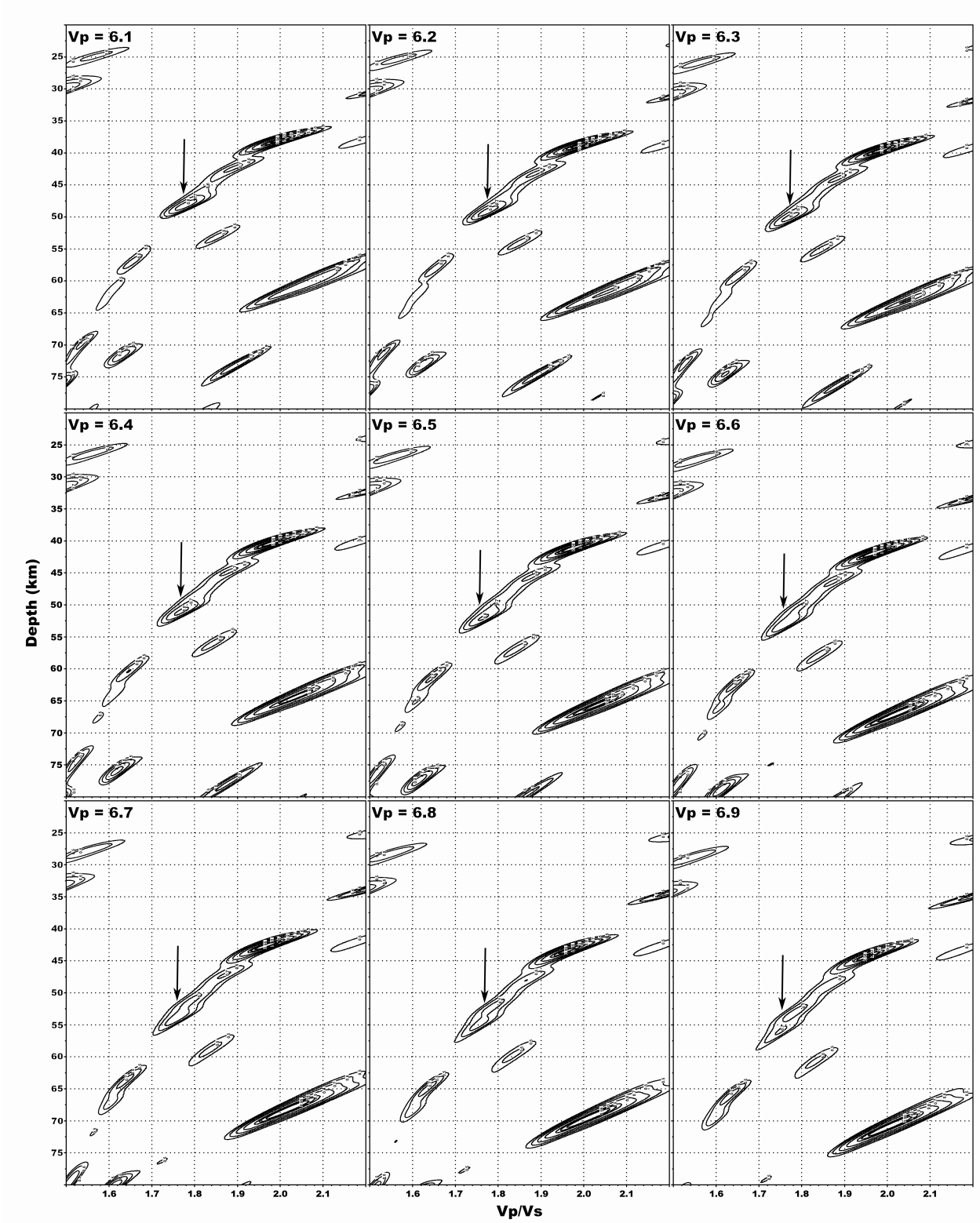

Figure C9: H – κ stacks of receiver functions from the EAST azimuth for station MYNC

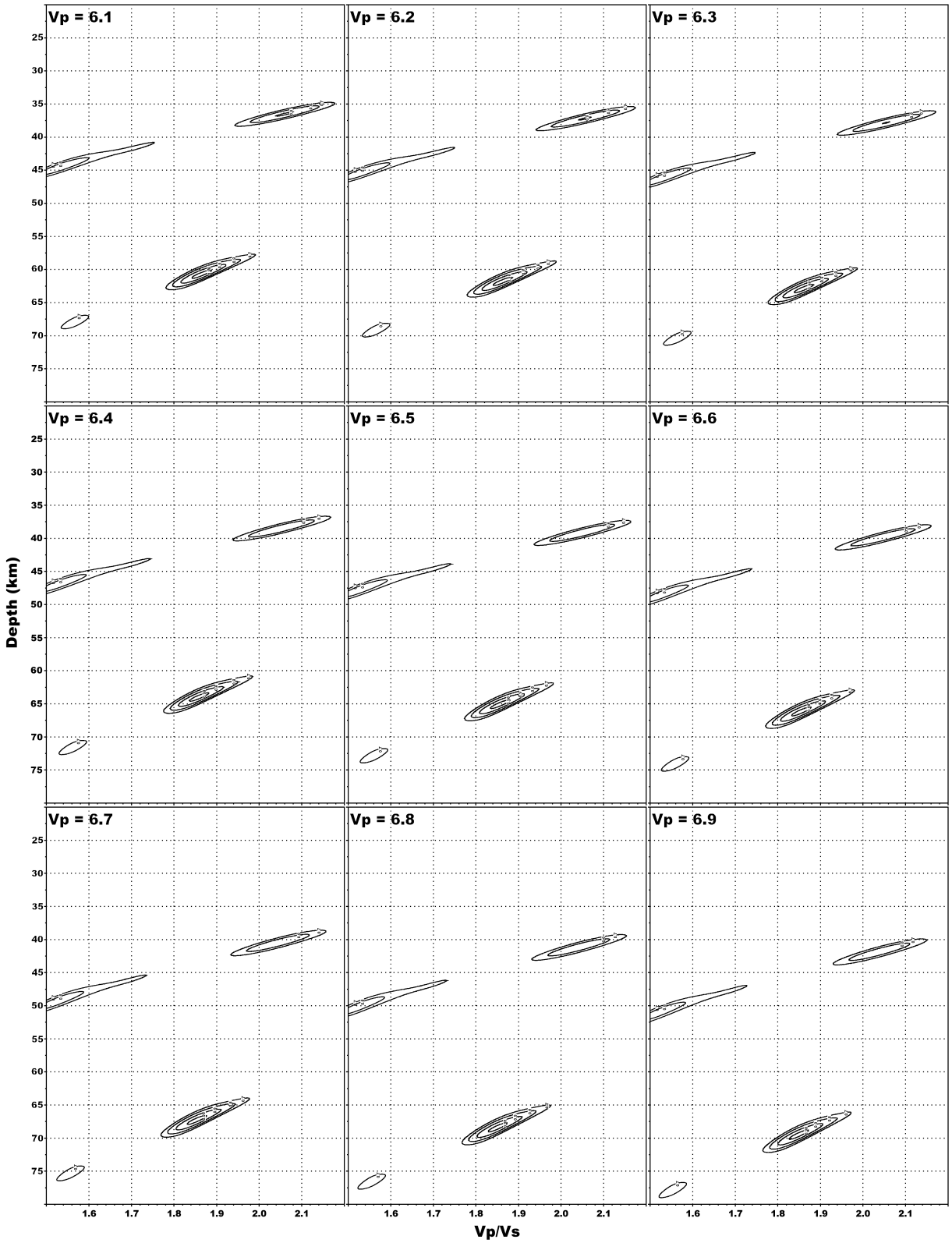

Figure C10: H – κ stacks of receiver functions from the NE azimuth for station MYNC

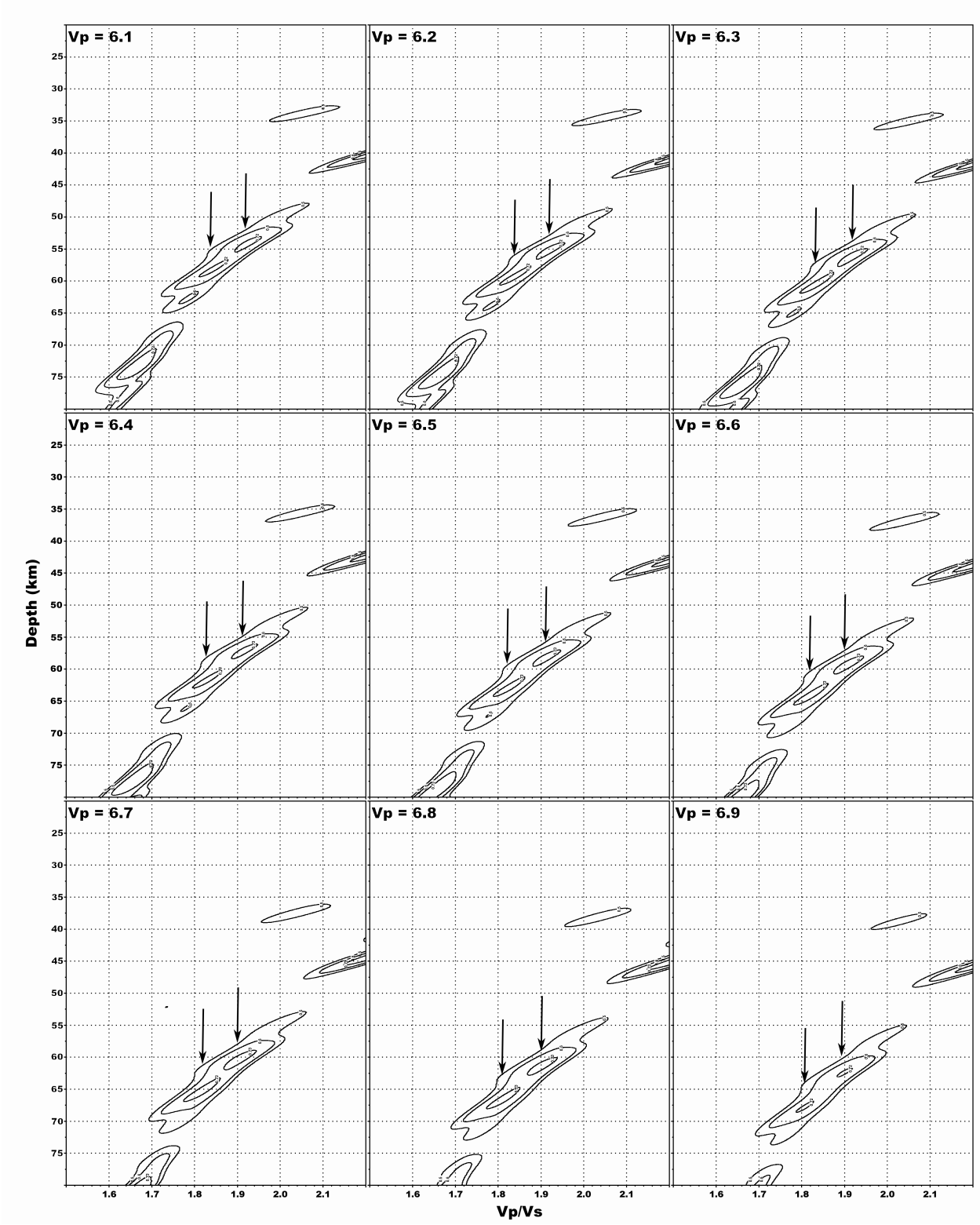

Figure C11: H – κ stacks of receiver functions from the NW azimuth for station MYNC

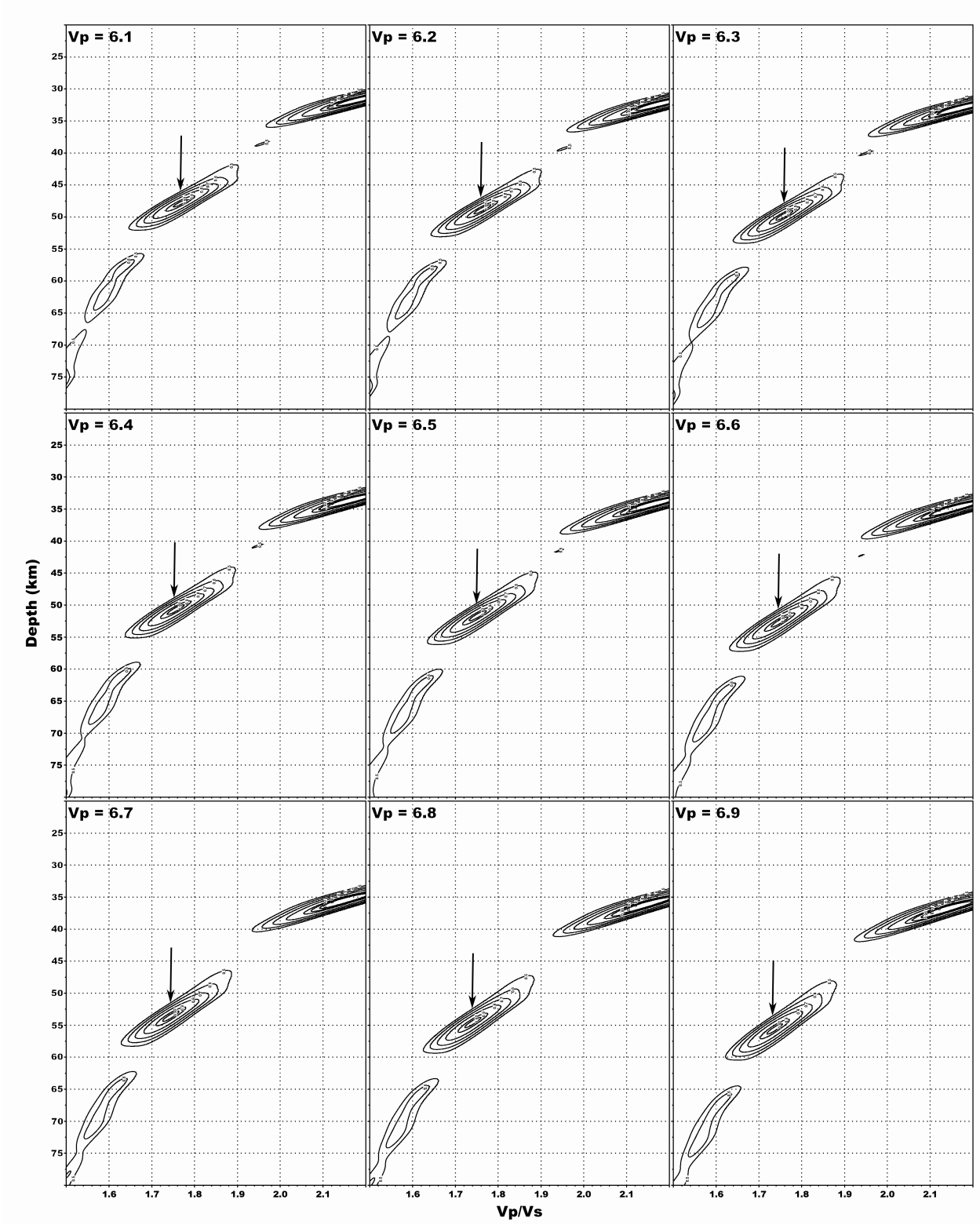

Figure C12: H – κ stacks of receiver functions from the SA azimuth for station MYNC

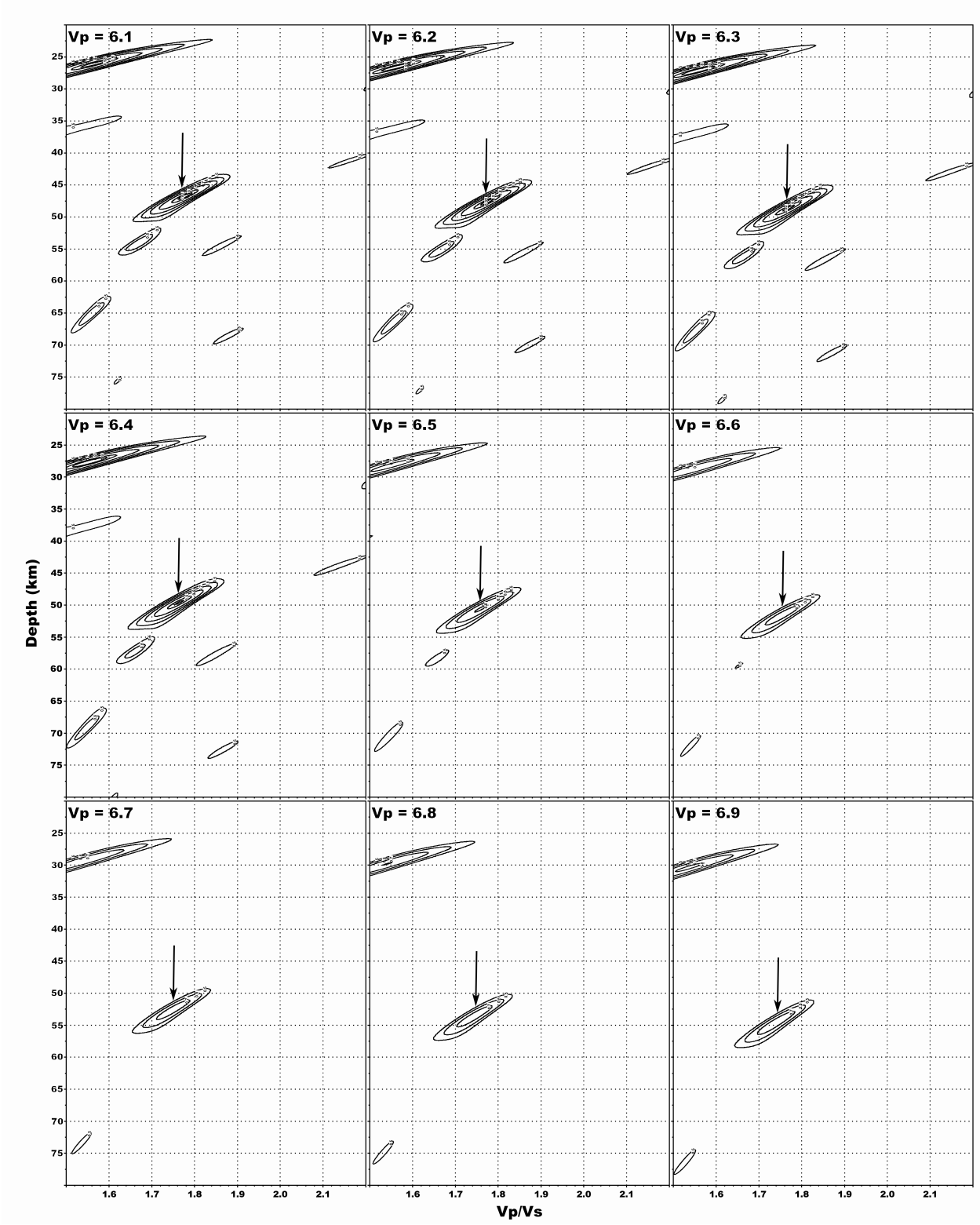

Figure C13: H – κ stacks of receiver functions from the SSW azimuth for station MYNC

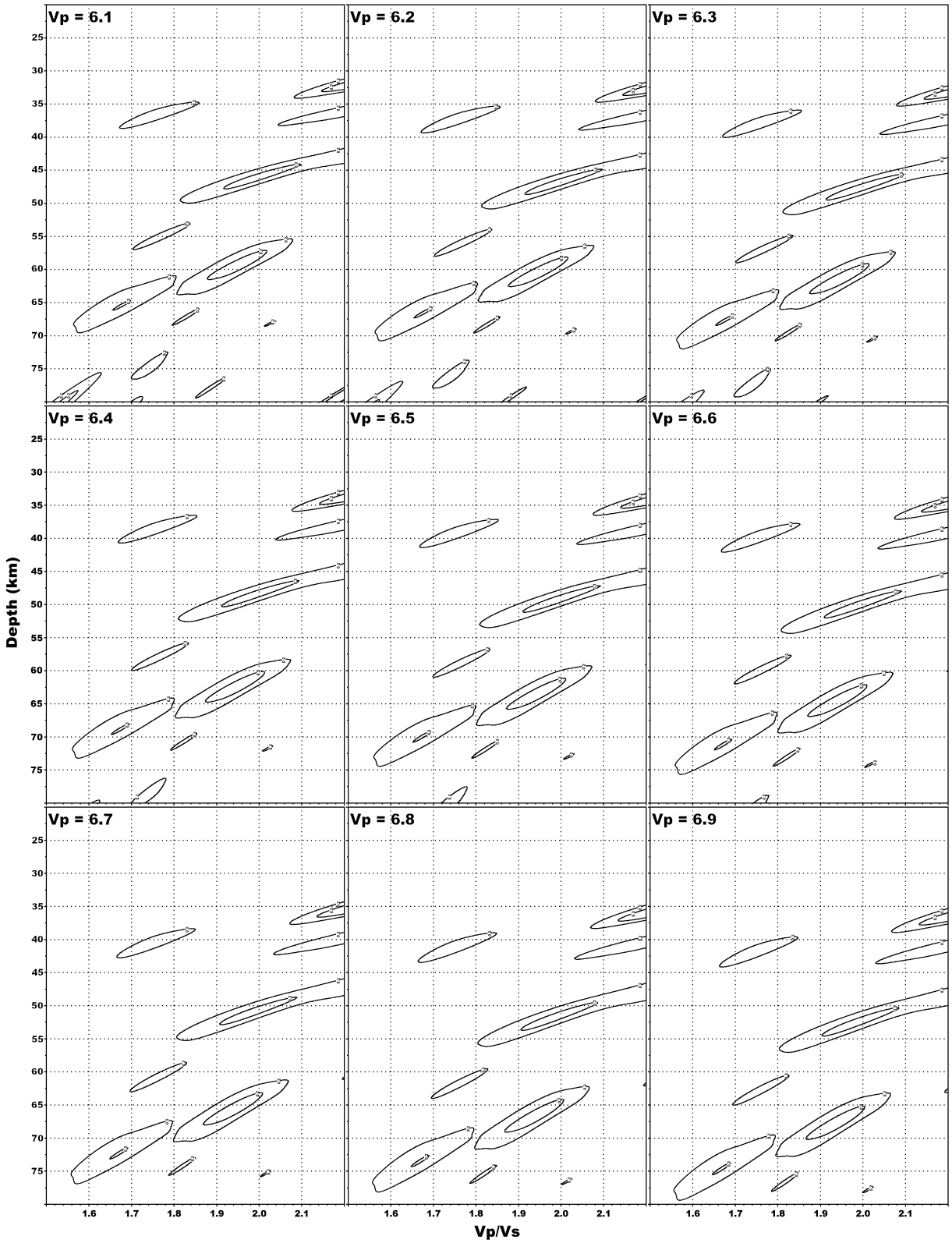

Figure C14: H – κ stacks of receiver functions from the WEST azimuth for station MYNC

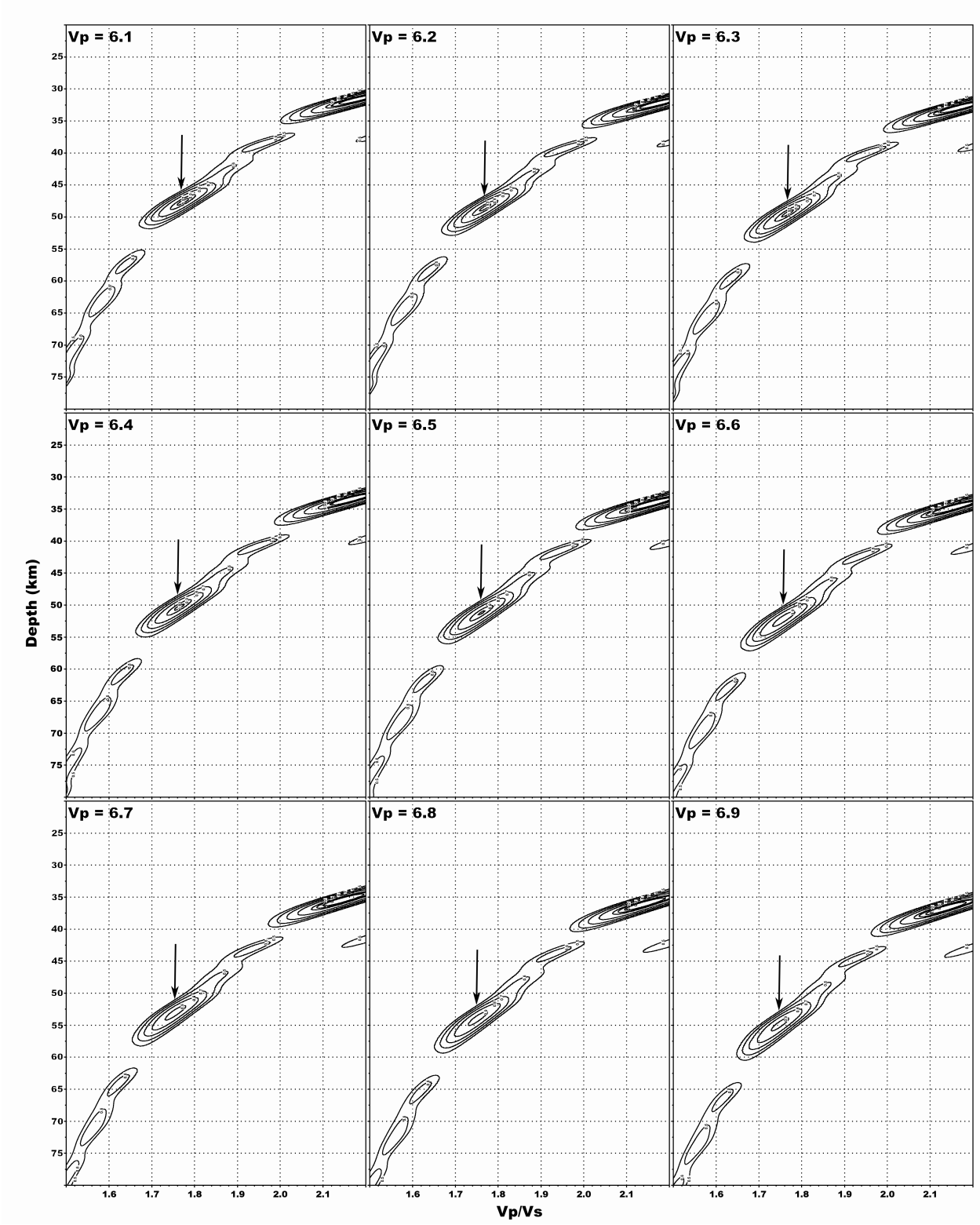

Figure C15: H – κ stacks of receiver functions for all events for station MYNC

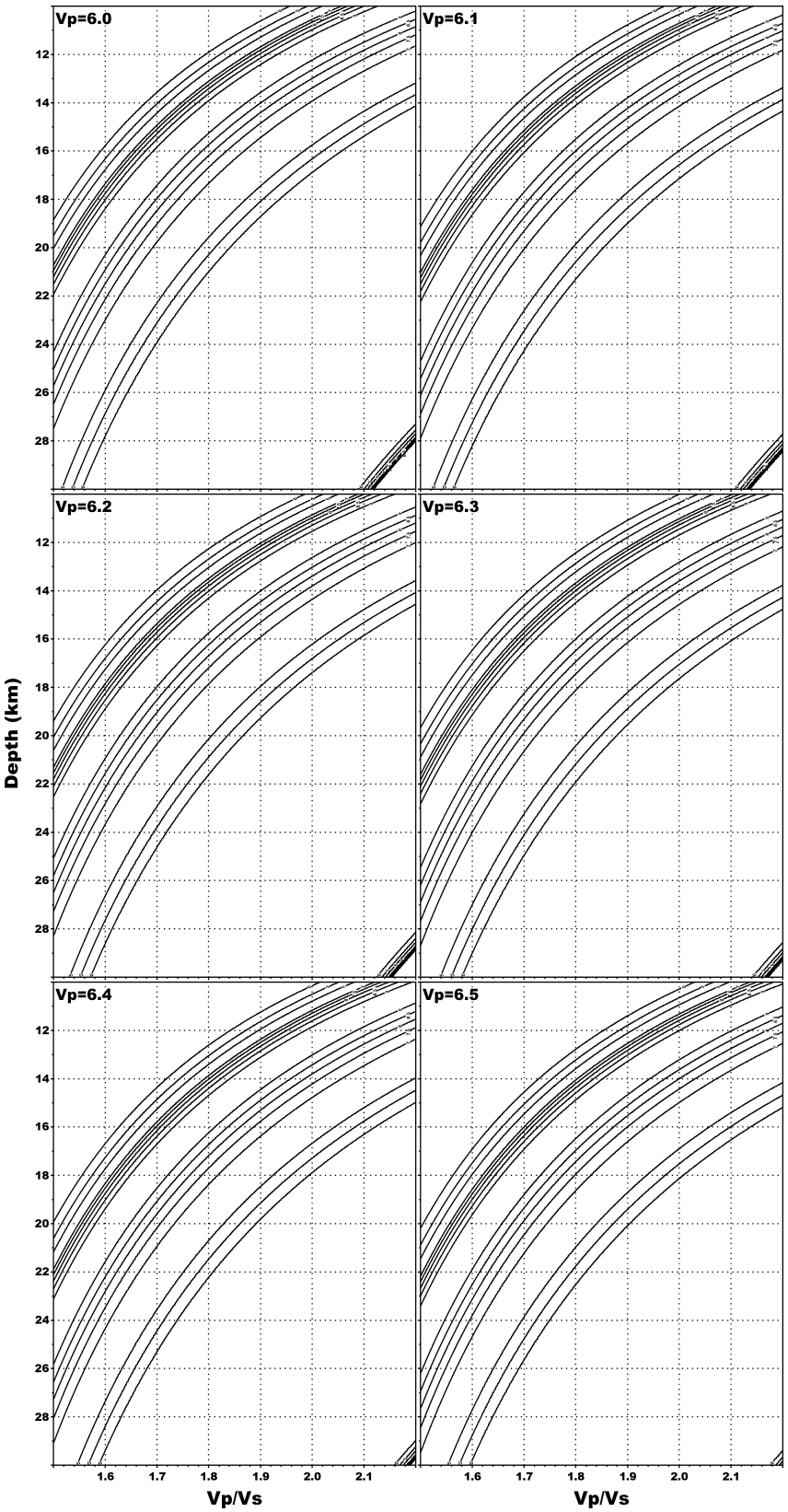

Figure C16: $H - \kappa$ stacks of receiver functions locating midcrustal arrival for MYNC